



Technische Universität München

Fakultät für Medizin



APPROACHING PRECLINICAL *IN VIVO*
EXPERIMENTS INVOLVING NANOPARTICLES AS
RADIOSENSITIZERS THROUGH MATHEMATICAL
MODELING AND MONTE CARLO SIMULATIONS

Alexander Patrick Klapproth

Vollständiger Abdruck der von der Fakultät für Medizin der Technischen Universität München zur Erlangung des akademischen Grades eines

Doktors der Naturwissenschaften (Dr. rer. nat.)

genehmigten Dissertation.

Vorsitz: Prof. Dimitrios Karampinos, Ph.D.

Prüfer*innen der Dissertation: 1. Prof. Dr. Vasilis Ntziachristos
2. Prof. Dr. Gabriele Multhoff

Die Dissertation wurde am 23.06.2022 bei der Technischen Universität München eingereicht und durch die Fakultät für Medizin am 11.10.2022 angenommen.

List of contributed articles

- A.P. Klapproth, M. Shevtsov, S. Stangl, W.B. Li, G. Multhoff, **A New Pharmacokinetic Model Describing the Biodistribution of Intravenously and Intratumorally Administered Superparamagnetic Iron Oxide Nanoparticles (SPIONs) in a GL261 Xenograft Glioblastoma Model**, *International Journal of Nanomedicine*, Volume 15, 2020, Pages 4677-4689, <https://doi.org/10.2147/IJN.S254745>. [1]
- A.P. Klapproth, M. Shevtsov, S. Stangl, W.B. Li, G. Multhoff, **A New Pharmacokinetic Model Describing the Biodistribution of Intravenously and Intratumorally Administered Superparamagnetic Iron Oxide Nanoparticles (SPIONs) in a GL261 Xenograft Glioblastoma Model [Corrigendum]**, *International Journal of Nanomedicine*, Volume 15, 2020, Pages 6067-6068, <https://doi.org/10.2147/IJN.S274126>. [2]
- A.P. Klapproth, J. Schuemann, S. Stangl, T. Xie, W.B. Li, G. Multhoff, **Multi-scale Monte Carlo simulations of gold nanoparticle-induced DNA damages for kilovoltage X-ray irradiation in a xenograft mouse model using TOPAS-nBio**, *Cancer Nanotechnology*, Volume 12, 2021, Page 27, <https://doi.org/10.1186/s12645-021-00099-3>. [3]

I am the first author and author in charge of all articles listed above. On top of these, I contributed to the following articles:

- W.B. Li, A. Belchior, M. Beuve, Y.Z. Chen, S. Di Maria, W. Friedland, B. Gervais, B. Heide, N. Hocine, A. Ipatov, A.P. Klapproth, C.Y. Li, J.L. Li, G. Multhoff, F. Poignant, R. Qiu, H. Rabus, B. Rudek, J. Schuemann, S. Stangl, E. Testa, C. Villagrasa, W.Z. Xie, Y.B. Zhang, **Intercomparison of dose enhancement ratio and secondary electron spectra for gold nanoparticles irradiated by X-rays calculated using multiple Monte Carlo simulation codes**, *Physica Medica*, Volume 69, 2020, Pages 147-163, ISSN 1120-1797, <https://doi.org/10.1016/j.ejmp.2019.12.011>. [4]
- W.B. Li, M. Beuve, S. Di Maria, W. Friedland, B. Heide, A.P. Klapproth, C.Y. Li, F. Poignant, H. Rabus, B. Rudek, J. Schuemann, C. Villagrasa, **Corrigendum to “Intercomparison of dose enhancement ratio and secondary electron spectra for gold nanoparticles irradiated by X-rays calculated using multiple Monte Carlo simulation codes”** [*Phys. Med.* **69** (2020) 147–163], *Physica Medica*, Volume 80, 2020, Pages 383-388, ISSN 1120-1797, <https://doi.org/10.1016/j.ejmp.2020.10.008>. [5]
- H. Rabus, W.B. Li, C. Villagrasa, J. Schuemann, P.A. Hepperle, L. de la Fuente Rosales, M. Beuve, S. Di Maria, A.P. Klapproth, C.Y. Li, F. Poignant, B. Rudek, H. Nettelbeck, **Intercomparison of Monte Carlo calculated dose enhancement ratios for gold nanoparticles irradiated by X-rays: Assessing the uncertainty and correct methodology for extended beams**, *Physica Medica*, Volume 84, 2021, Pages 241-253, ISSN 1120-1797, <https://doi.org/10.1016/j.ejmp.2021.03.005>. [6]

- N. Yudintceva, N. Mikhailova, D. Bobkov, L. Yakovleva, B. Nikolaev, D. Krasavina, A. Muraviov, T. Vinogradova, P. Yablonskiy, I. Samusenko, V. Ryzhov, V. Deriglazov, Y. Marchenko, G. Multhoff, A.P. Klapproth, W.B. Li, B. Nayak, A. Sonawane, M. Shevtsov, **Evaluation of the Biodistribution of Mesenchymal Stem Cells in a Pre-clinical Renal Tuberculosis Model by Non-linear Magnetic Response Measurements**, *Frontiers in Physics*, Volume 9, 2021, ISSN 2296-424X, <https://doi.org/10.3389/fphy.2021.625622>. [7]
- H. Rabus, W.B. Li, H. Nettelbeck, J. Schuemann, C. Villagrasa, M. Beuve, S. Di Maria, B. Heide, A.P. Klapproth, F. Poignant, R. Qiu, B. Rudek, **Consistency checks of results from a Monte Carlo code intercomparison for emitted electron spectra and energy deposition around a single gold nanoparticle irradiated by X-rays**, *Radiation Measurements*, Volume 147, 2021, Page 106637, ISSN 1350-4487, <https://doi.org/10.1016/j.radmeas.2021.106637>. [8]
- W.B. Li, S. Stangl, A.P. Klapproth, M. Shevtsov, A. Hernandez, M.A. Kimm, J. Schuemann, R. Qiu, B. Michalke, M.A. Bernal, J. Li, K. Hürkamp, Y. Zhang, G. Multhoff, **Application of High-Z Gold Nanoparticles in Targeted Cancer Radiotherapy—Pharmacokinetic Modeling, Monte Carlo Simulation and Radiobiological Effect Modeling**, *Cancers*, 2021, Volume 13, Page 5370, <https://doi.org/10.3390/cancers13215370>. [9]

Contents

List of contributed articles	I
Contents	IV
Abstract	VI
Zusammenfassung	VI
Abbreviations	VII
1. Motivation	1
2. Introduction	4
3. Background	7
3.1. Compartmental modeling in biology	7
3.2. Physiologically based pharmacokinetic models	8
3.3. Radiosensitization effects of AuNPs	9
3.4. SPIONs	10
4. Methodology	12
4.1. Publication summary: A PBPK model describing the biodistribution of SPIONs	12
4.2. PBPK model for SPIONs	13
4.2.1. Structure	15
4.2.2. Parameter values	16
4.3. MC Simulations with a single AuNP	18
4.4. Multi-scale MC simulations	19
4.4.1. Mouse model	20
4.4.2. Tumor	25
4.4.3. Cell	26
4.4.4. Randomization algorithm for AuFeNPs	28
4.4.5. Nucleus	31

4.5. Publication summary: Multi-scale Monte Carlo simulations of DNA damages with and without AuNPs	34
5. Discussion and Literature Review	37
5.1. SPIONs	37
5.2. PBPK model	38
5.3. AuFeNPs	39
5.4. MC simulations	39
5.4.1. Limitations	40
6. Outlook	43
A. Included publications	46
A.1. A new pharmacokinetic model describing the biodistribution of i.v. and intratumorally administered superparamagnetic iron oxide nanoparticles (SPIONs) in a GL261 xenograft glioblastoma model	46
A.1.1. Article	46
A.1.2. Supplementary information	60
A.2. Erratum: A new pharmacokinetic model describing the biodistribution of i.v. and intratumorally administered superparamagnetic iron oxide nanoparticles (SPIONs) in a GL261 xenograft glioblastoma model [corrigendum]	63
A.3. Multi-scale Monte Carlo simulations of gold nanoparticle-induced DNA damages for kilovoltage X-ray irradiation in a xenograft mouse model using TOPAS-nBio	65
A.3.1. Article	65
A.3.2. Supplementary information	84
List of Figures	91
List of Tables	92
Bibliography	93

Abstract

In this work, we investigated the biodistribution and radiosensitization effects of different types of nanoparticles in preclinical mouse models. First, we developed a mathematical model in order to simulate the route of the nanoparticles inside the murine body after injection, as well as their concentrations in the bloodstream, organs and the tumor over time. We then proceeded to quantify how gold coated nanoparticles inside a tumor can affect the efficacy of radiotherapy. The radiosensitizing effect was quantified by Monte Carlo simulations including a detailed DNA model.

Zusammenfassung

In dieser Arbeit wurde sowohl die Biodistribution als auch der radiosensitivierende Effekt unterschiedlicher Nanopartikel in präklinischen Modellen bzw. Mausexperimenten mit Hilfe mathematischer Modelle analysiert. Zunächst wurde ein mathematisches Modell entwickelt, durch das die Verteilung von Nanopartikeln und ihre Konzentrationen in Blutkreislauf, unterschiedlichen Organen und einem Tumor nach dem Injizieren in Mäuse simuliert werden kann. Danach wurde der Effekt von Nanopartikeln mit einer Gold-Oberfläche auf die Effizienz einer Strahlentherapie durch Monte Carlo Simulationen quantifiziert.

Abbreviations

Gold-Fe₂O₃-hybrid-nanoparticle (AuFeNP)
Gold nanoparticle (AuNP)
Blood-brain barrier (BBB)
Cell region (CR)
Dose enhancement ratio (DER)
Double strand break (DSB)
Enhanced permeability and retention (EPR)
Heat shock protein 70 (Hsp70)
Intravenous (i.v.)
Local effect model (LEM)
Least squares objective function (LSOF)
Monte Carlo (MC)
Magnetic Resonance Imaging (MRI)
Nanoparticle (NP)
Ordinary differential equation (ODE)
Physiologically based pharmacokinetic (PBPK)
Polyethylene glycol (PEG)
Positron emission tomography (PET)
Relative biological effectiveness (RBE)
Reactive oxygen species (ROS)
Small animal radiation research platform (SARRP)
Strand break (SB)
Single photon emission computer tomography (SPECT)
Superparamagnetic iron oxide nanoparticle (SPION)
Single strand break (SSB)
Tool for Particle Simulation (TOPAS)

1. Motivation

Cancer research has been one of the most dominating fields in biology and preclinical studies for many decades. Many scientific groups are working with the aim to create more efficient and reliable treatment methods, so eventually more patients can be cured and live better lives. Before such novel and promising methods can be tested on humans, they have to pass through several phases of rigorous preclinical and clinical studies. One of the big topics in preclinical research with clinical potential is the employment of nanoparticles (NPs). Their applications in both cancer diagnostics and therapy are ample, including among others as contrast agents, vehicles for drugs or radiosensitizers [10, 11, 12]. Even without active targeting their potential to accumulate inside tumors passively due to the enhanced permeability and retention (EPR) effect has already been shown [13, 14].

Since the groundbreaking study published by Hainfeld et al. in 2004, which showed the potential of gold NPs (AuNPs) to locally increase radiation dose and, therefore, more effectively kill tumor cells, AuNPs have become one of the leading NPs in cancer research [15, 16]. Their widespread utilization is supported by the fact that radiotherapy cannot be applied without harming healthy tissue in the process. Radiotherapy can lead to severe side effects: the most frequent are normal tissue toxicity, oral pain, loss of appetite, and general fatigue [17]. The presence of gold nanoparticles inside tumor cells can, however, locally enhance the effectiveness of irradiation on the tumor and therefore reduce the required dose for effective radiotherapy [18]. While this effect has the potential to significantly improve radiotherapy, it is still constrained by its low energy range and the potential accumulation of AuNPs in healthy cells. In order to tackle both problems at once AuNPs can be

functionalized with tumor specific reagents such as antibodies to specifically target tumor cells [19]. Reliable targeting methods are presently rare but are essential for a successful application of AuNPs in clinical practice [20].

Studies investigating the reliability of NP targeting towards tumor cells are often supported by mathematical models, which help to understand biological interactions and can be used to predict experimental outcome. A common tool for the biodistribution of pharmaceutical agents is physiologically based pharmacokinetic (PBPK) models [21, 22]. These are especially valuable for research involving tissues that are difficult or impossible to measure in reality [23]. The popularity of PBPK models is documented by multiple published reviews over the last decade reporting about the large number of recent models and their contributions [21, 22, 24, 25, 26]. Modeling the biodistribution of NPs particularly has become a fast-moving field [22, 24, 26]. These models have the potential to predict the effects of the large diversity of presently investigated NPs in terms of size, shape, material and coating composition. Changing any of these parameters can cause significant differences in the pharmacokinetic behavior of the NP in living cells and organisms [26]. Therefore, it is key to choose the most suitable model carefully and even to develop a new model if necessary.

For optimizing NP supported radiotherapy it is crucial to estimate the dose enhancing effect caused by the NPs as accurately as possible. In that regard Monte Carlo (MC) simulations provide a frequently used tool for calculating the expected dose with and without NPs [27, 28]. Since such simulations can be performed computationally, they allow for testing different scenarios and optimizing the use of NPs without having to conduct numerous expensive wet-laboratory experiments. Among others AuNPs have been studied extensively in these studies. Calculating the dose enhancement caused by a single AuNP is already very complicated and several studies have concentrated on exactly this question [4, 8, 29, 30, 31, 32]. There is also still some controversy about the best way to physically describe the interactions around a single irradiated AuNP [5, 6]. As it is crucial to design the optimal strategy when developing a viable therapeutic method for the clinic, MC simulations play an im-

portant role in preclinical studies investigating the radiosensitizing effects of AuNPs [20].

The aim of this study is to develop new techniques to model and simulate pre-clinical *in vivo* experiments with nanoparticles, so that the parameters of those experiments can be calibrated beforehand and the necessary amount of resources and laboratory animals is minimized.

2. Introduction

One of the biggest challenges for AuNP-based strategies for radiosensitization of tumor cells is the identification of biomarkers for precise tumor targeting. Since novel treatments must be efficient as well as executable on a daily basis, the easiest mode of delivery is an intravenous (i.v.) injection. In contrast, intratumoral injections deliver higher amounts of AuNPs to close proximity of the tumor, but may include complex medical procedures, which are associated with unfavorable side effects for the patient. Consequently, i.v. injections are much more efficient in terms of time and cost, while sparing patients unnecessary discomfort. Although the EPR effect allows some passive, non-specific uptake of AuNPs into the tumor cells, the EPR effect on its own does not guarantee a sufficient amount of gold inside tumor cells without harming the patients' organs due to the toxicity of high doses of AuNPs after i.v. injection [33]. Therefore, active targeting of AuNPs towards tumor cells through functionalization would be advantageous. This requires a tumor-specific biomarker that can be targeted via the bloodstream. Heat shock protein 70 (Hsp70) has been proven to be present on the surface of many different tumor types, however, not on the surface of corresponding normal tissues [34, 35]. This makes membrane-bound Hsp70 a very promising target for tumor therapy and initiated the development of the cmHsp70.1 antibody, which identifies the membrane form of Hsp70 on tumor cells [36, 35]. Since membrane Hsp70 has a short turn-over time, reagents – such as antibodies or AuNPs – functionalized with a Hsp70 antibody, which binds to membrane-bound Hsp70 on tumor cells, are rapidly internalized.

The effects of such targeting techniques can also be the focus of MC studies investigating AuNPs. One issue for such investigations has been a discrepancy between

simulation and experimental results [37]. Simulations in most cases suggest a necessary AuNP concentration of approximately 1% of weight within or around a cell to yield significant dose enhancement. Yet experiments in living cells have shown that much lower concentrations of AuNPs can already impair cell survival [37].

For a long time the best solution was the employment of the Local Effect Model (LEM), which was introduced by Kraft et al. in 1999 [38]. It typically includes basic MC simulations calculating the dose enhancement caused by a single AuNP under the investigated circumstances. The dose enhancement is stored as a function of distance from the AuNP. Then the results are mathematically extrapolated to calculate the relative biological effectiveness (RBE) of multiple AuNPs inside one or more cells. The model uses the probability for lethal events at each location inside the cell. This information can then be used to predict cell survival based on factors like radiation source, AuNP characteristics, AuNP concentrations or AuNP distribution [37, 39, 40, 41, 42]. There are several approaches to improve the LEM model to meet the conditions of AuNP enhanced irradiation more precisely [43, 44]. Though helpful in many cases, even most specialized models add further assumptions and uncertainties to the existing problems of MC simulations, which already show uncertainties in low-energy regions and still do not include all the relevant processes. This is because they mostly just simulate the impact of physical interactions caused by photons, protons, electrons, etc., while neglecting potentially significant effects of chemical species or triggered biological mechanisms [20]. Many groups have, therefore, shifted their focus back to directly assessing cell damage during their MC simulations. This requires not only computers with high processing power, but also accurate cell geometries that are implemented into the MC code.

Cell geometries, in particular DNA models, have been included in some form in every widely used MC code. Especially worth mentioning is the PARTRAC code, through which important pioneer work has been done for many years [45]. In recent years, the Geant4 toolkit [46] has become more and more popular due to its open source distribution, regularly updated physics models and multithreading capabilities [47, 48]. Especially interesting for this work is the side-project Geant4-DNA,

which designs and implements models describing radiation caused damage down to a sub-cellular scale [49]. On top of that there are several projects developing more user-friendly, specialized software that employs Geant4 physics processes. The GATE toolkit, for example, was specifically built for positron emission tomography (PET) and single photon emission computer tomography (SPECT) [50]. The Tool for Particle Simulation (TOPAS) is more versatile, although it was initially exclusively developed for proton applications [51]. Since its release it has been constantly extended and represents an easy-to-use tool for a multitude of applications that can make use of Geant4 physics models, such as dose calculation in voxel phantoms, implementing modeling organ effects, or microdosimetry [52, 53, 54]. An extension to TOPAS called TOPAS-nBio was released recently, which includes not only detailed cell and DNA geometries, but also physics and chemistry models based on Geant4-DNA [55, 56, 57]. It, therefore, counteracts several mentioned limitations of MC simulations and is thus a good choice for radiobiological simulations on cellular and sub-cellular scale.

3. Background

3.1. Compartmental modeling in biology

Most biological processes have one central problem in common – they include so many different interactions, micro and/or macro molecules, that not all of them can be taken into account, when one tries to make predictions about their outcome. Hence, it can be very challenging to develop a mathematical model that describes a complex process and produces useful quantitative results. Since none of the models can include all involved interactions, it is crucial to identify the most important ones and only include as many as necessary and, in turn, as little as possible. Compartmental models are one of the most common types of mathematical models that deal with this problem. In these models each object is assigned one of a finite number of states at each point in time. Objects can change their state over time through transitions that are described by mathematical equations. The different states are represented by compartments. If one tries to depict a biological interaction that is relevant in a scientific study, the number of compartments and possible transitions can quickly become unmanageable. The same applies to the complexity of the individual transitions, i.e. mathematical equations. This brings us back to the importance of keeping the model as simple as possible, without missing any important interactions. Otherwise the number of parameters involved in the model can get too large to extract any useful information from it [58].

3.2. Physiologically based pharmacokinetic models

The transportation of drugs of any kind in, around and out of the body of an organism is called pharmacokinetics. It is followed or accompanied by the pharmacodynamics - the biological response at the site of action. The goal for therapies involving a drug is usually to achieve an ideal concentration of the drug at the site of action without reaching a toxic concentration at any other location within the body. A different way to describe pharmacokinetics is “the study of drug concentrations in different body compartments over time”. Existing knowledge about the pharmacokinetics of drugs and their respective target can be used to develop a compartmental model called physiologically based pharmacokinetic (PBPK) model. In this model the central transportation route and compartment is almost in all cases the blood circulation. More accurately it is usually either the whole blood, including red and white blood cells, plasma or serum. Apart from that different PBPK models can differ heavily from one another, since their form depends on many factors, including (amongst others) investigated drug, injection mode, organs of interest, and available experimental data set.

PBPK models can be used to answer many questions. Firstly, they can help to fill knowledge gaps about the drug concentrations in certain compartments at certain time points where no physical measurements were performed. They can also support the analysis of mechanisms responsible for the speed of distribution and the final endpoint of drug transport inside the body. After the model is validated, it can also be used to test different scenarios to make predictions about the outcome in different patients, the sensitivity of certain parameters, or the influence of actors / procedures that might affect one or more pathways [59]. A good example for the latter is the already mentioned tumor targeting, by which the rate of tumor uptake is increased.

3.3. Radiosensitization effects of AuNPs

Before simulating cell damages through radiation some physical fundamentals need to be understood. An x-ray beam, as was used in the simulations in this work, can be divided into a large number of single photons traveling through space. Along their path they deposit energy to their surrounding molecules (i.e. absorbers), mostly through many transfer events, in which they lose small amounts of energy. The mean value of deposited energy is around 58 eV per event [60]. The probability of a photon to interact with other particles depends on its energy and the density and atomic number of the absorber [61]. In MC simulations these probabilities are combined in so-called cross sections. In Geant4 these cross sections are part of the physics lists the user can choose according to their applications. During an interaction a photon can either be fully absorbed and thereafter disappear or be scattered. In case the photon is absorbed, the atom it interacted with releases positrons or electrons, and their combined energy is close to the energy of the absorbed photon. If the photon is scattered there is the possibility that it does not lose any energy and continues traveling with the same energy. It can also lose some of its energy to an electron, which is released in the process. Electrons picking up energy in this way start to travel on their own and are called secondary electrons [61]. They are the most important source of physical DNA damages in our upcoming simulations. There are several types of possible interactions between photons and matter, but we are focusing on the three most important ones in terms of our study: the Compton effect, the photoelectric effect, and pair production [62] - and how their impact on the results is affected by AuNPs.

The Compton effect is the dominant source of physical DNA damage in the absence of radiosensitizers. The Compton effect occurs when a photon collides with an electron and transfers some of its energy to it, while getting scattered. This means the photon moves on and is able to keep interacting with the matter. In addition, the electron becomes a secondary electron, and is released from its atom in case it was bound to one before the interaction. It starts traveling as a free particle and is

thereby able to damage the tissue. The probability of the Compton effect to occur is mostly unaffected by the addition of AuNPs [63, 64].

In the photoelectric effect a photon is fully absorbed by an electron, which is bound to one of the inner shells of an atom. This causes the electron to be released from the atom, leaving a vacancy in one of its shells. This vacancy is immediately filled by another electron from an outer shell, causing an energy imbalance inside the atom. The atom evens this out by releasing an additional electron, and its kinetic energy is exactly the difference between the two atomic orbits. These secondary electrons are called Auger-electrons and their production the Auger-effect. Since the atomic bond of the electron before the interaction is a requirement for the photoelectric effect, its probability increases significantly for atoms with a large atomic number Z , also called high- Z materials. Since high- Z atoms also have more atomic shells, the Auger-effect can occur in them more than once at the same time, resulting in a so-called Auger-cascade. Since gold is a high- Z material, the addition of AuNPs has a big impact on the occurrence rate of the photoelectric and Auger-effect making it the dominant effect in scenarios where AuNPs are present as radiosensitizers. The probability of the photoelectric effect is also in inverse proportion to the photon energy so the radiosensitizing effect of AuNPs is much stronger in keV range than in MeV range [28, 63, 64].

Pair production occurs when a photon is absorbed by the nucleus of an atom causing it to release an electron-positron-pair. Shortly after, the positron combines with an electron, which causes both of their existences to cease, while two photons are created with opposite momenta. This effect is only relevant for high energy photon beams [62, 64].

3.4. SPIONs

Another type of NP, which is also the focus of many studies, is superparamagnetic iron oxide nanoparticle (SPION). Superparamagnetism is a phenomenon only observed in magnetic particles below a certain size, which depends on the material. As

long as thermal energy stays within a certain range and there is no external magnetic field applied, the orientation of the NP's magnetic moments is flipped repeatedly in very short time intervals in the order of 10^{-9} s or less. This means that in any given period longer than 10^{-9} s, superparamagnetic particles appear to have zero net magnetization. This has the effect of SPIONs not attracting each other through their magnetic properties. Yet external magnetic fields disturb this interaction and still attract superparamagnetic particles [65]. SPIONs can, therefore, be directed towards their desired destination by an external magnet or used as contrast agents for Magnetic Resonance Imaging (MRI). These and various other possible applications in both diagnostics and theranostics make SPIONs a popular agent for tumor research [66].

Our goal is to combine the advantageous properties of AuNPs and SPIONs by using hybrid NPs with a Fe_2O_3 core and a gold surface.

4. Methodology

4.1. Publication summary: A PBPK model describing the biodistribution of SPIONs

The first step towards projecting a realistic NP distribution inside tumor cells is approximating the number of NPs reaching the tumor in the first place. For that purpose a PBPK model was set up to describe the biodistribution of SPIONs after either i.v. or intratumoral injection. The findings of this work were published in the *International Journal of Nanomedicine* under the title *A new pharmacokinetic model describing the biodistribution of i.v. and intratumorally administered superparamagnetic iron oxide nanoparticles (SPIONs) in a GL261 xenograft glioblastoma model* [1]. There has been a corrigendum, which only regards the list of co-authors and the phrasing of one sentence [2].

Two types of SPIONs, ^{89}Zr -Perimag®-COOH and ^{99m}Tc -ferucarbotran, were injected either intratumorally or intravenously into C57BL/6 mice. There were three different sets of laboratory experiments, which were conducted by my colleagues: (i) intratumorally injected ^{89}Zr -Perimag®-COOH SPIONs, (ii) i.v. injected ^{99m}Tc -ferucarbotran SPIONs and (iii) i.v. injected ^{89}Zr -Perimag®-COOH SPIONs. The mice in (i) and (ii) bore subcutaneous GL261 glioblastomas and the ones in (iii) were tumor-free. The SPION content within the most important organs was measured by obtaining and weighing tissue samples and then determining the percent of injected dose per gram using a gamma counter.

Based on the data of biologists in our laboratory, I developed a PBPK model

describing the biodistribution of SPIONs inside mice after intratumoral and i.v. injection. The model contains the tumor, blood and important organs as compartments. Their SPION content over time is described by ordinary differential equations (ODEs) that include 30 constants. I estimated the parameters for each set of experiments by fitting the model to the respective experimental data of (i). Then, I used the resulting parameters as starting points for fitting the ones of (ii) and (iii). Since not all organs were included in (ii) and (iii), I adopted the constants for the missing organs from the set calculated for (i).

Through a long process of optimizing my parameter fitting techniques, I was able to compute sets of constants for each experiment that describe the measurement data accurately. The model shows that after intratumoral injection a big fraction of SPIONs is quickly released from the tumor into the blood stream and then into all other organs. Yet the SPION concentrations in most organs and the tumor decrease over time and a large share of SPIONs eventually end up in liver and spleen. After i.v. injection most SPIONs are immediately released into the tumor and organs before they are again mostly transported to liver and spleen. The most important conclusion of this study is that the i.v. injection of NPs without tumor targeting is not viable for clinical applications, which underlines the importance of finding and improving targeting techniques.

Although there were some limitations regarding the study, I was able to set up a working PBPK model that could describe several sets of experimental data. The model can henceforth be used as a base line for future preclinical experiments including SPIONs in mice.

4.2. PBPK model for SPIONs

I developed a PBPK model to describe the biodistribution of SPIONs after injection. Data from either intratumoral or i.v. injection was used to fit the parameters to compare the differences between these modes.

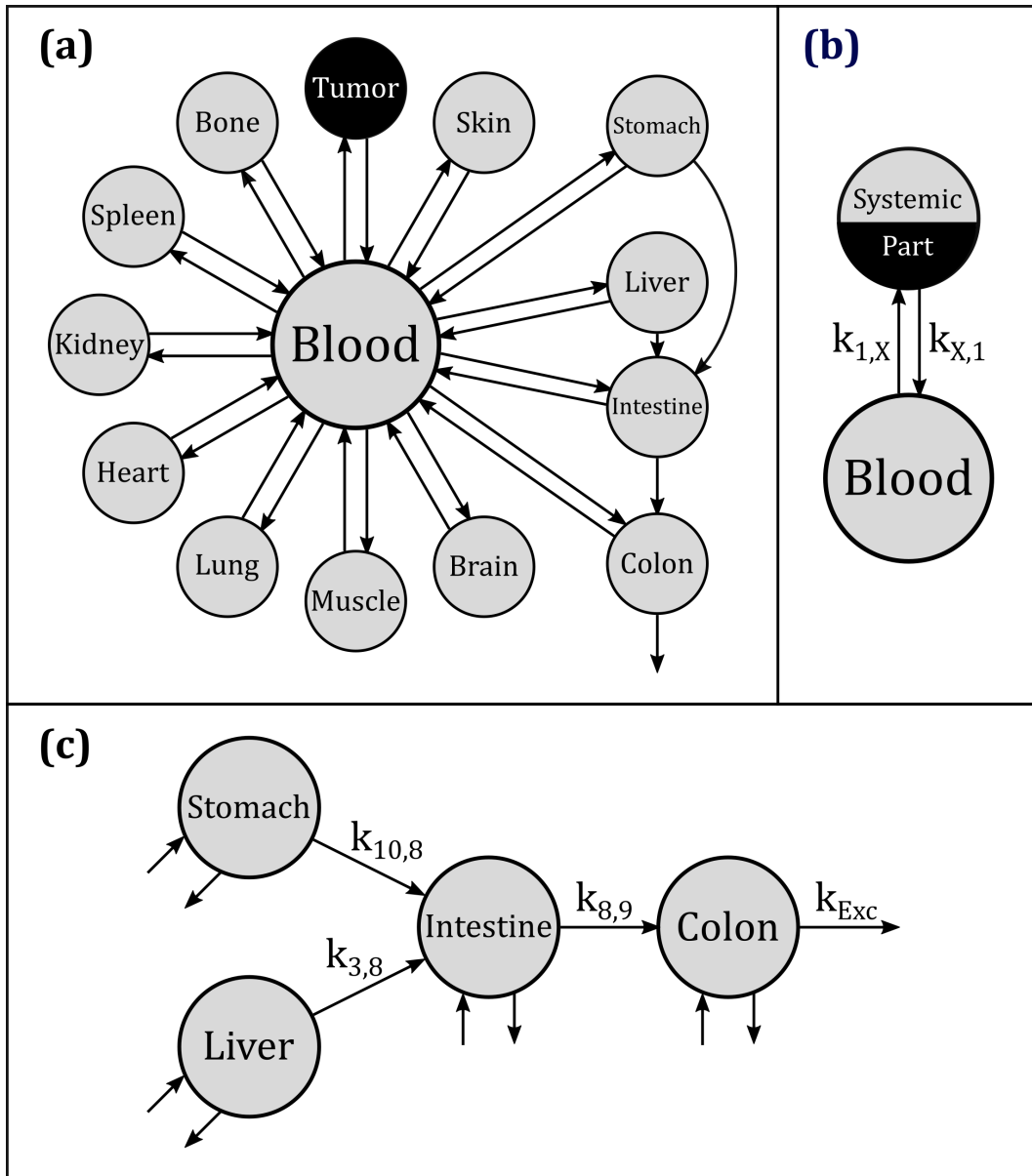


Figure 1.: **PBPK model structure:** (a) shows the overall structure of the model, where each circle describes a compartment and each arrow one possible pathway for SPIONs to be transferred. “Intestine” is short for small intestine. (b) displays systemic circulation through blood, which is the dominating transportation route in our model. (c) illustrates the alimentary tract in more detail. Source: Klapproth et al. (2020): A New Pharmacokinetic Model Describing the Biodistribution of Intravenously and Intratumorally Administered Superparamagnetic Iron Oxide Nanoparticles (SPIONs) in a GL261 Xenograft Glioblastoma Model [1].

4.2.1. Structure

The overall model structure is shown in Figure 1a. The murine body is divided into 13 separate compartments, which are blood, tumor and important organs. Tumor and organs are grouped under the more generic term “systemic part”. I have taken the assumption that there are only two possible pathways for SPIONs to travel between body parts - the bloodstream (Figure 1b) and the alimentary tract (Figure 1c). For each compartment there is an ODE describing the amount of SPIONs it contains over time:

$$\dot{S}_{blood}(t) = \sum_{i=2}^{14} (k_{i,1} \cdot S_i(t) - k_{1,i} \cdot S_{blood}(t)) \quad (1)$$

$$\dot{S}_{tumor}(t) = -k_{2,1} \cdot S_{tumor}(t) + k_{1,2} \cdot S_{blood}(t) \quad (2)$$

$$\dot{S}_{liver}(t) = -k_{3,1} \cdot S_{liver}(t) + k_{1,3} \cdot S_{blood}(t) - k_{3,8} \cdot S_{liver}(t) \quad (3)$$

$$\dot{S}_{spleen}(t) = -k_{4,1} \cdot S_{spleen}(t) + k_{1,4} \cdot S_{blood}(t) \quad (4)$$

$$\dot{S}_{kidney}(t) = -k_{5,1} \cdot S_{kidney}(t) + k_{1,5} \cdot S_{blood}(t) \quad (5)$$

$$\dot{S}_{heart}(t) = -k_{6,1} \cdot S_{heart}(t) + k_{1,6} \cdot S_{blood}(t) \quad (6)$$

$$\dot{S}_{lung}(t) = -k_{7,1} \cdot S_{lung}(t) + k_{1,7} \cdot S_{blood}(t) \quad (7)$$

$$\begin{aligned} \dot{S}_{intestine}(t) &= -k_{8,1} \cdot S_{intestine}(t) + k_{1,8} \cdot S_{blood}(t) \\ &\quad + k_{3,8} \cdot S_{liver}(t) - k_{8,9} \cdot S_{intestine}(t) + k_{10,8} \cdot S_{stomach}(t) \end{aligned} \quad (8)$$

$$\begin{aligned} \dot{S}_{colon}(t) &= -k_{9,1} \cdot S_{colon}(t) + k_{1,9} \cdot S_{blood}(t) \\ &\quad + k_{8,9} \cdot S_{intestine}(t) - k_{Exc} \cdot S_{colon}(t) \end{aligned} \quad (9)$$

$$\dot{S}_{stomach}(t) = -k_{10,1} \cdot S_{stomach}(t) + k_{1,10} \cdot S_{blood}(t) - k_{10,8} \cdot S_{stomach}(t) \quad (10)$$

$$\dot{S}_{brain}(t) = -k_{11,1} \cdot S_{brain}(t) + k_{1,11} \cdot S_{blood}(t) \quad (11)$$

$$\dot{S}_{muscle}(t) = -k_{12,1} \cdot S_{muscle}(t) + k_{1,12} \cdot S_{blood}(t) \quad (12)$$

$$\dot{S}_{bone}(t) = -k_{13,1} \cdot S_{bone}(t) + k_{1,13} \cdot S_{blood}(t) \quad (13)$$

$$\dot{S}_{skin}(t) = -k_{14,1} \cdot S_{skin}(t) + k_{1,14} \cdot S_{blood}(t) \quad (14)$$

S_C denotes the SPION content of a particular compartment C and its change at a certain time point t is described by the respective equation for $\dot{S}_C(t)$. Each single pathway of the model, which is illustrated by an arrow in Figure 1a, is embodied by one summand in Equations (1-14). Both uptake and emission are assumed to be linear for each systemic part, so every pathway is described by two multipliers: $k_{x,y} \cdot S_c(t)$. The expression $k_{x,y}$ denotes a transition rate from systemic part x to systemic part y , where each compartment is assigned an integer between 1 and 14. In this case, x would be the integer assigned to compartment c , which is the source for this pathway. Each transition rate is assumed to be a constant parameter with unit $1/t$.

4.2.2. Parameter values

Values of the constant transition rates $k_{i,j}$ were estimated by fitting simulation results produced by the PBPK model to experimental data. I used MATLAB for all the following calculations. Measurements were in the form of “ $x\%$ of the initial dose per gram”. This means I could manually add an additional data point at $t_0 = 0$, in which depending on the injection mode either $S_{tumor}(t_0) = 100\%$ or $S_{blood}(t_0) = 100\%$. The initial values at t_0 were respectively set to 0 for all other compartments. However, to be able to compare SPION concentrations directly, I had to multiply each data point by the respective weight of the systemic part, in which it was measured. Weights of blood and organs were derived from literature [67, 68, 69, 70, 71, 72, 73].

For parameter estimation I developed a procedure based on iterating global multistart fits with a least squares objective function (LSOF). In its simplest form a LSOF has the following structure:

$$LSOF(D_{exp}, D_{sim}) = \sum_{t \in T_{exp}, c \in C} (D_{exp}(t, c) - D_{sim}(t, c))^2 \quad (15)$$

D_{exp} denotes a set of data derived from experimental measurements and includes one (mean) data point for each compartment in the set of compartments C for every

time point in the set of experimental time points T_{exp} . In other words, $D_{exp}(t, c)$ is the experimental measurement in compartment c at time t . $D_{sim}(t, c)$ is the equivalent time point computed in a model simulation, whereas D_{sim} denotes the set of all data points derived from one simulation. The LSOF, therefore, summates squared differences between each experimental data point and its corresponding simulation point. For an optimal fit this function has to be minimized. For the parameter estimation method in this work, I also introduced weights for each compartment, which were inversely proportional to its data points. Otherwise, the organs containing very low concentrations of SPIONs over the whole course of the experiments would be almost completely ignored during parameter fitting. Furthermore, I added a penalty term that increases the LSOF even more, in case $D_{sim}(t, c)$ is outside the confidence interval of the respective $D_{exp}(t, c)$.

Even after defining a reasonable objective function minimizing it can still be challenging, since the initial values for the algorithm can have a big impact on the results. For such a complex model as ours, it is thus not possible to ever be sure that the actual minimum of the LSOF has been found. For this work I developed a minimization procedure in two steps. First, all transition rates included in the ODE for a single systemic part were approximated individually. This was achieved by consecutively minimizing LSOFs with a greatly increased weight for the respective compartment. This step was repeated 1000 times for each compartment; each time with different initial values chosen randomly around the best values found up to this point by previous iterations (i.e. multi-start approach). The best values found in step 1 were then used in the second step, in which another multi-start approach with 1000 attempts tried to minimize the actual global LSOF. This whole two-step process had to be repeated several times until the model with the resulting parameters could describe the experimental data.

4.3. MC Simulations with a single AuNP

To investigate the radiosensitization effects of NPs with a gold surface in living mice, I developed a set of Monte Carlo simulation tools. Setting up their geometry was a complex process. The first set of simulations I performed was part of a large project, in which several working groups performed simulations with different Monte Carlo codes, following the same instructions regarding geometry setup and photon sources. The results were published in 2020 [4]. The envelope for the geometry is a cubical water phantom. In its center one single spherical AuNP is placed. The particle is irradiated by a circular photon beam with the same center and radius as the AuNP. The area around the AuNP is divided into concentric shells. Within a 1 μm distance from the AuNP, the range between shells is 1 nm and for distances between 1 μm and 50 μm the shell width is 1 μm . In each shell the average amount of deposited energy per photon is then calculated during the simulations. In addition, the energy spectrum of electrons released from the AuNP was stored. All simulations were performed for both a 50 nm and a 100 nm AuNP, each with two different x-ray sources: 50 kVp and 100 kVp. On the basis of the deposited energy E_{dep} with and without AuNP, the dose enhancement ratio (DER) was calculated for each shell. This was defined as

$$DER = \frac{E_{dep} \text{ per photon with AuNP}}{E_{dep} \text{ per photon without AuNP}} \quad (16)$$

The results show a DER of more than 500 in the low nanometer range, but a very quick decrease within the first 200 nm (cf. Figure 2). On micrometer scale the DER drops even further and for most scenarios it becomes relatively ineffective after around 20 μm (cf. Figure 3). Since grown cells usually have a diameter in the two-digit μm range, these results prove that it might not be sufficient to just transport AuNPs into tumor cells, but also their destiny within these cells are a crucial factor for their efficiency.

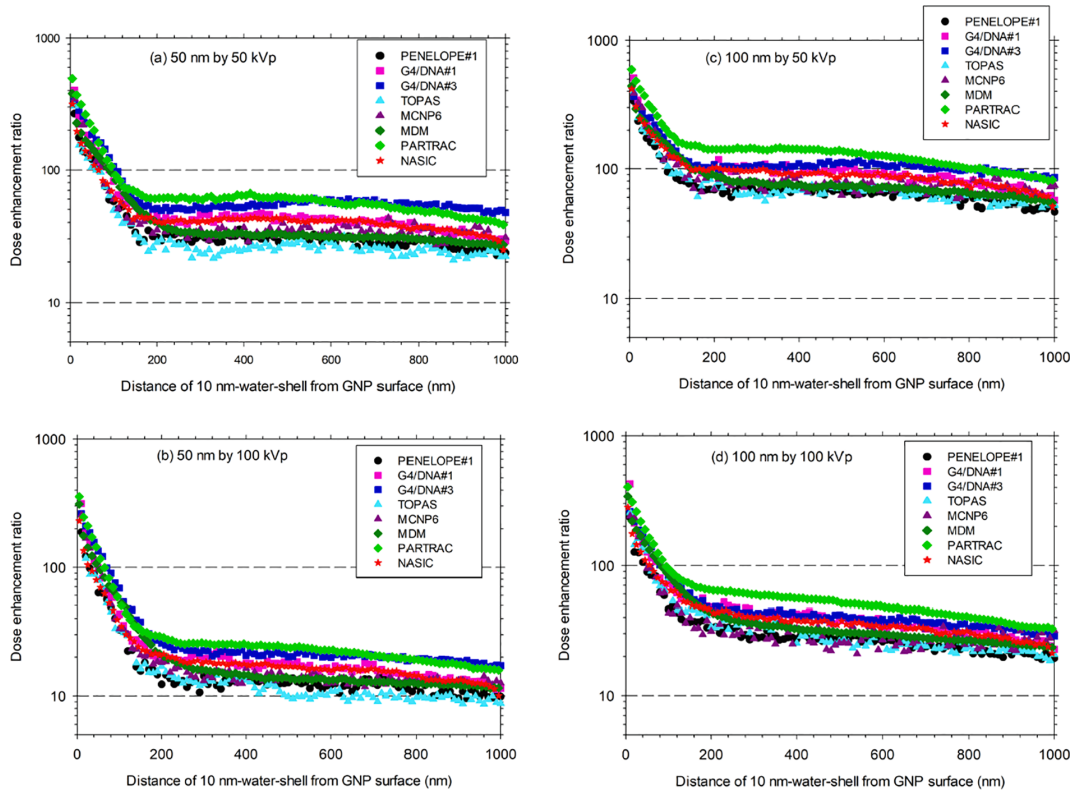


Figure 2.: **DER in nanometer range calculated by simulations with a single AuNP:** Results provided by myself are labeled as “G4/DNA#3”. Source: Li et al. (2020): Corrigendum to “Intercomparison of dose enhancement ratio and secondary electron spectra for gold nanoparticles irradiated by X-rays calculated using multiple Monte Carlo simulation codes” [Phys. Med. 69 (2020) 147-163] [5].

4.4. Multi-scale MC simulations

To combine the results from previous projects and eventually simulate the interactions during preclinical *in vivo* experiments in the field of NP-assisted radiotherapy, I developed a multi-step methodology for Monte Carlo simulations on multiple scales.

TOPAS-nBio was chosen as the primary programming environment because of reasons listed below. Its focus on simulating ionizing radiation meant that it included all the necessary physics and chemistry models from Geant4, which is already with optimized parameters for nanoscale DNA damage applications. As an extension to TOPAS it is much more user friendly than Geant4 and enables the combination and usage of existing geometries without any programming skills. This means the results of my work are much easier to replicate and advance in future studies. In addition,

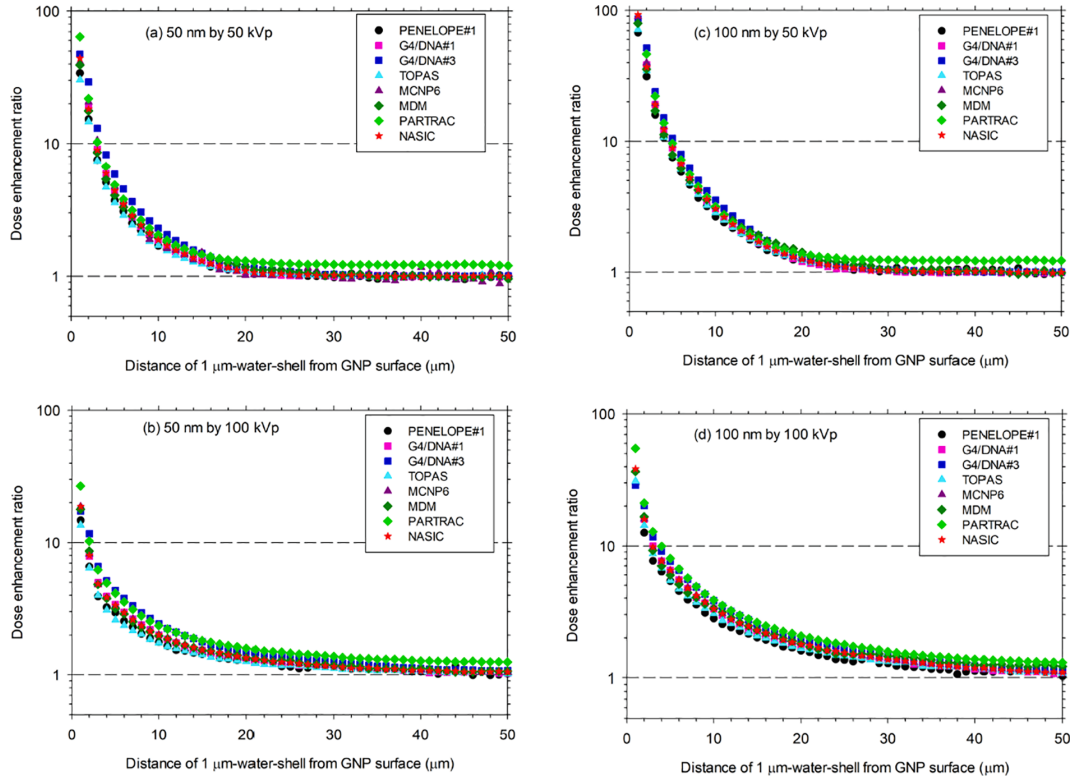


Figure 3.: **DER in micrometer range calculated by simulations with a single AuNP:** Results provided by myself are labeled as “G4/DNA#3”. Source: Li et al. (2020): Corrigendum to “Intercomparison of dose enhancement ratio and secondary electron spectra for gold nanoparticles irradiated by X-rays calculated using multiple Monte Carlo simulation codes” [Phys. Med. 69 (2020) 147-163] [5].

TOPAS-nBio is currently in a constant process of development ensuring state of the art models and methods in our field of research.

The development of the simulation code can essentially be divided into 4 major steps.

4.4.1. Mouse model

Based on the existing TOPAS extensions for voxelized components, I wrote an extension for the inclusion of a voxel-based model. It is specialized for models in the form of binary files with one line, where the material for each voxel is defined by a single integer value (i.e. flag) in the binary file. Each material is, therefore, represented by a distinct flag. The list of materials in our case, their respective flags

and the Geant4 material assigned to them can be found in Table 1. This means, for example, that a binary file containing only the vector (9, 9, 9, 27) would produce a model consisting of 3 air voxels and 1 skeleton voxel. The number of voxels on each axis of the model, as well as the voxel dimensions, are defined separately in the TOPAS parameter file.

Table 1.: **Flags and materials in the mouse model simulations:** For each body part, either the regarding Geant4 Material or G4_WATER with an adjusted density was applied. A similar table can be found in Klapproth et al. (2021): Multi-scale Monte Carlo simulations of gold nanoparticle-induced DNA damages for kilovoltage X-ray irradiation in a xenograft mouse model using TOPAS-nBio [3].

Flag	Body Part	G4 Material	Density in g/cm ³
8	Normal Tissue	G4_TISSUE_SOFT_ICRP	1.03
9	Air	G4_AIR	$1.205 \cdot 10^{-3}$
11	Skin	G4_SKIN_ICRP	1.09
12	Heart	G4_WATER	1.06
13	Blood	G4_WATER	1.00
14	Liver	G4_WATER	1.05
15	Gallbladder	G4_WATER	1.03
16	Lung	G4_LUNG_ICRP	1.04
17	Stomach	G4_WATER	1.04
18	Airway	G4_AIR	$1.205 \cdot 10^{-3}$
19	Pancreas	G4_WATER	1.05
20	Kidney	G4_WATER	1.05
21	Spleen	G4_WATER	1.06
22	Small Intestine	G4_WATER	1.04
23	Large Intestine	G4_WATER	1.04
24	Bladder	G4_WATER	1.04
25	Vas Deferens	G4_WATER	1.04
26	Testes	G4_TESTIS_ICRP	1.04
27	Skeleton	G4_BONE_COMPACT_ICRU	1.85
28	Brain	G4_BRAIN_ICRP	1.04
29	Thyroid	G4_WATER	1.05
-	Tumor	G4_WATER	1.00

Although it is an important region of interest in many MC studies, the model or phantom of a living body usually does not contain a tumor. Therefore, my extension included the possibility to insert an ellipsoidal tumor at any location within the boundaries of the voxel model. Size, dimensions and position of the tumor can be defined by the user in the parameter file. This is done by replacing all air, skin and

normal tissue inside the defined area by tumor tissue. If the tumor stretches outside the mouse body, a one voxel thick layer of skin is planted around the overlapping tumor surface. In our case the tumor is placed near the left hind leg of the mouse to represent a mammary gland tumor with diameters $5 \text{ mm} \times 4 \text{ mm} \times 5 \text{ mm}$ on the X, Y and Z axis respectively. A visualization of the model used in our final simulations can be found in Figure 4. It was provided by Dr. Tianwu Xie from the Geneva University Hospital [74].

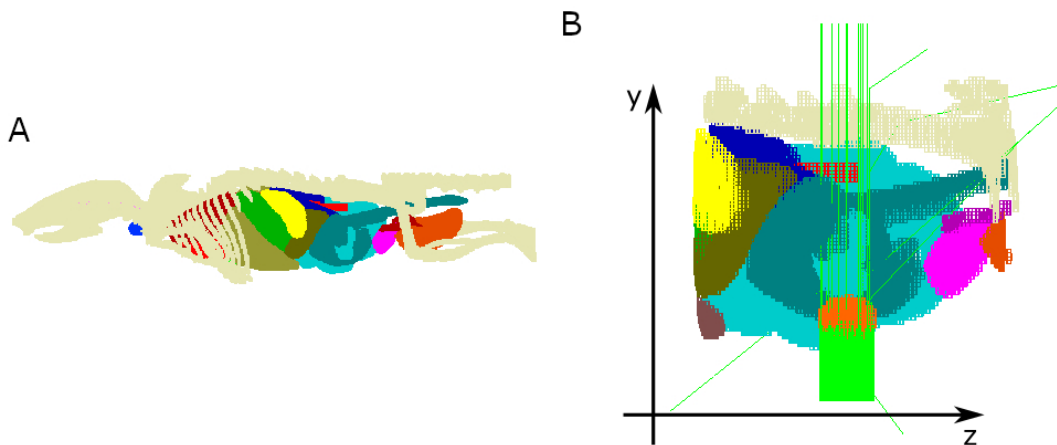


Figure 4.: **Sketch of the voxel model simulations:** **A** displays a visualization of the implemented mouse model, where each color represents a different organ. **B** shows the approach of the simulations. The source consists of parallel photon beams (displayed in green) and is aimed directly at the mammary gland tumor (displayed in orange). The coordinate system has been added for orientation, not to mark the actual origin of the simulation geometry. Source: Klapproth et al. (2021): Multi-scale Monte Carlo simulations of gold nanoparticle-induced DNA damages for kilovoltage X-ray irradiation in a xenograft mouse model using TOPAS-nBio [3].

In the parameter file the model can also be placed and rotated at will and additional geometry components can be added. For this work, I included a circular radiation source that produces parallel photons with a kVp spectrum, which can be defined by the user as well. I produced two different spectra (100 kVp and 200 kVp) for our simulations with SpekCalc [75, 76, 77]. The parameters for generating the spectra were chosen to conform to the radiation source in the small animal radiation research platform (SARRP) device, which is often used by our work group at the Klinikum rechts der Isar for *in vivo* irradiation experiments [78]. Figure 5 illustrates

the resulting spectra. The radius of the source was equal to the tumor radius and it was placed 20 cm below (i.e. along the Y-axis) the tumor center. Therefore, each photon that does not encounter any interaction beforehand reaches the tumor and each part of the tumor can possibly be irradiated. Regardless of the spectrum, 220,000 photons were produced by the initial source.

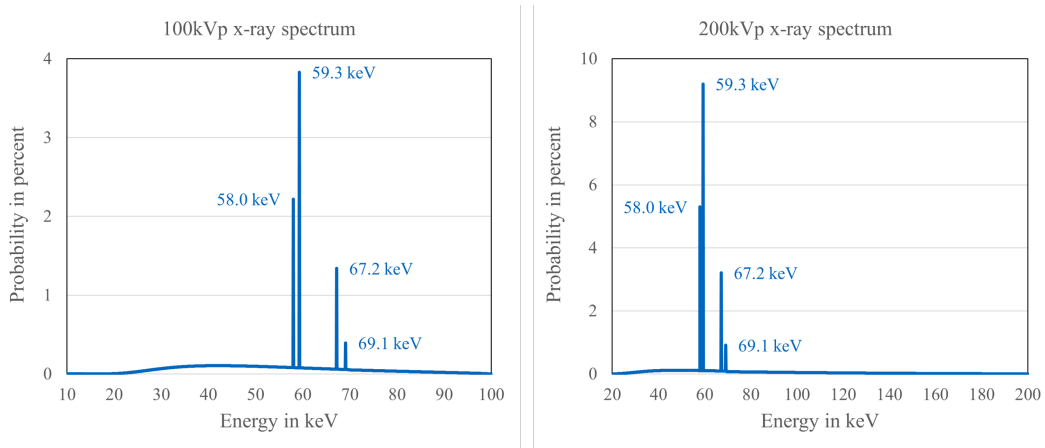


Figure 5.: **X-ray photon spectra:** The 100kVp spectrum ranges from 10 to 100 keV with a bin size of 0.05 keV and the 200kVp spectrum from 20 to 200 keV with bin size 0.1 keV. The energy for each created particle is chosen randomly based on the percentages defined by the respective spectrum. Source: Klapproth et al. (2021): Multi-scale Monte Carlo simulations of gold nanoparticle-induced DNA damages for kilovoltage X-ray irradiation in a xenograft mouse model using TOPAS-nBio [3].

For all simulations the tumor consisted of liquid water since the current Geant4-DNA models, which were used due to their accuracy, can only be applied in the G4_WATER material. The fact that cells including their DNA consist of water is a common assumption in the field [79, 80, 81]. The standard Geant4 electromagnetic physics list option 3 was used in this first step, since it is recommended as the standard model for medical applications in the micrometer range or above [47, 82]. More accurate physics lists are available and applied in later steps, but on the relatively large scale of a mouse model they only would have caused a disproportionate increase in computation time. The benefit on the other hand would have been without significance since most of the very time-consuming low energy tracks would have occurred outside the regions of interest, which are inside the tumor.

The essential parameters for all particles entering the tumor were stored in a file called (mouse model \rightarrow tumor) phase space. It contains each stored particle in a separate line, including its location, momentum, particle type, and energy. Geant4 computes the progression of each particle individually and in discrete steps. Hence a particle gets scored when the pre-step location is outside and the post-step position inside the tumor for one of its steps. Afterwards the track is killed since there is no further evaluation in this first simulation. As it would have been too time-consuming to simulate enough photons in a macro-scale geometry to achieve results in the 1 Gy area, I had to start with 220,000 photons. Each particle scored in the phase space was then stored in the phase space 750 times. This means that every time a particle entered the tumor in the simulation, 750 new lines were added to the phase space, each having the same particle type and energy as the scored particle. However, momentum and position were chosen randomly for each duplicate to increase variance between particles in subsequent simulation steps. One of two different randomization modes was chosen based on the arrival momentum of the scored particle. If a particle still had its initial momentum of $(0,1,0)$, it was assumed to have reached the tumor without any interaction. In this case each individual phase space entry was made by computing a random position on the bottom or rather Y-Minus-side of the tumor. For that a random point within the X-Z-ellipsis (i.e. an ellipsis with diameters $5 \text{ mm} \times 5 \text{ mm}$) was generated and then the Y-coordinate was calculated, so the resulting point lays on the bottom side of the tumor surface. The reasoning behind this is that a particle without interaction could also have been generated at any other possible location of the initial source and reach the tumor in the same way. If a scored particle has any other momentum, however, there is no doubt that it has undergone some type of interaction on its way to the tumor. In that case each duplicate is rotated around the y-axis going through the tumor center. That way the particle diversion of previous interactions is not lost through the duplication process. Both randomization modes are visualized in Figure 6.

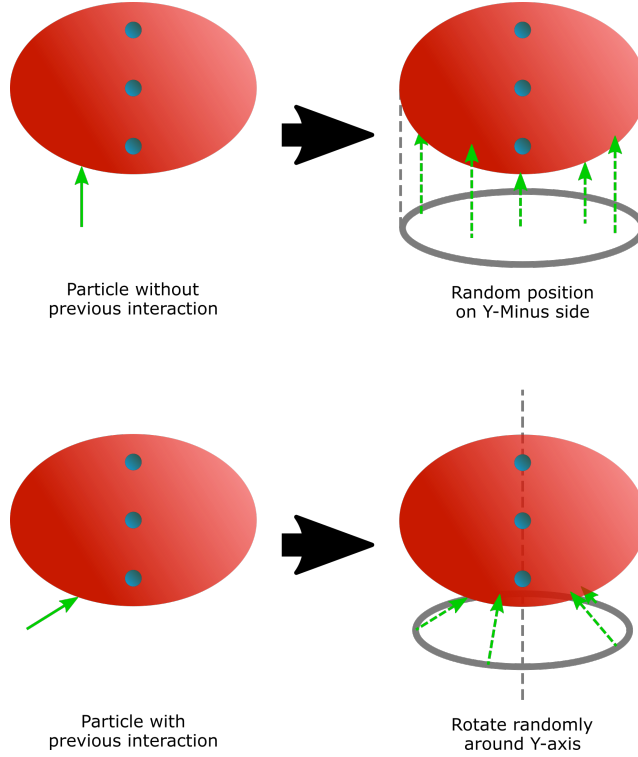


Figure 6.: **Visualization of the randomization modes for particles in the (mouse model \rightarrow tumor) phase space:** The applied mode for an incoming particle (green) is chosen based on its momentum.

4.4.2. Tumor

The tumor was defined as an ellipsoid consisting of water and diameters $5 \text{ mm} \times 4 \text{ mm} \times 5 \text{ mm}$. Its center is at the origin of the coordinate plane. At three different locations inside the tumor I defined spheres with a diameter of $100 \text{ }\mu\text{m}$, which will be called cell regions (CRs). The coordinates of the CR centers are $M_{Front} = (0 \text{ mm}, -1.89 \text{ mm}, 0 \text{ mm})$, $M_{Center} = (0 \text{ mm}, 0 \text{ mm}, 0 \text{ mm})$ and $M_{Back} = (0 \text{ mm}, 1.89 \text{ mm}, 0 \text{ mm})$ respectively. The denotation stems from the direction of the initial photon source. Since the distance between the border of the front CR and the tumor surface is just $60 \text{ }\mu\text{m}$, it can be reached by particles almost immediately after entering the tumor. A sketch of the geometric concept (not to scale) can be found in Figure 7.

My early simulation concepts even included 9 CRs at different locations inside the tumor to investigate the effect of shifts along the X-axis (which due to overall symmetry should be equivalent to shifts along the Z-axis). Yet first results already

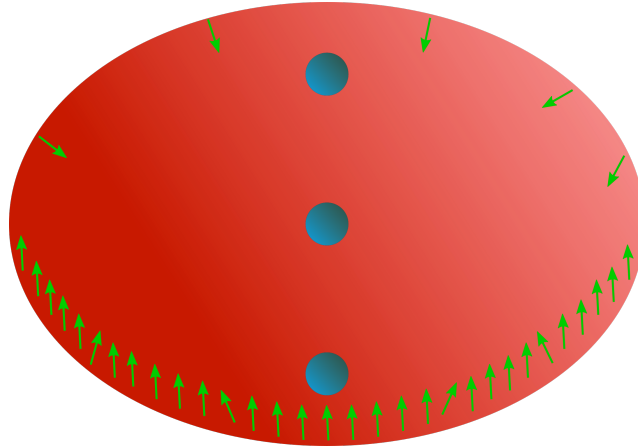


Figure 7.: **Sketch of the Tumor simulations:** The particle source, which is shown in green, is the (mouse model \rightarrow tumor) phase space file. Most particles enter the tumor with their initial momentum without previous interaction, but particles can enter from any direction. Cell-sized spheres are defined at three different positions. All particles entering a cell are stored in its respective phase space. Source: Klapproth et al. (2021): Multi-scale Monte Carlo simulations of gold nanoparticle-induced DNA damages for kilovoltage X-ray irradiation in a xenograft mouse model using TOPAS-nBio [3].

showed that there were no significant differences between data points, when cells changed their position on the X-axis, so I focused only on Y-axis effects.

Although the cell diameters, as will be discussed later, were assumed to be $20\ \mu\text{m}$, all particles entering these $100\ \mu\text{m}$ CRs were scored. This way a higher variance between scored particles could be achieved. Similarly to the approach of the (mouse model \rightarrow tumor) phase space, all scored particles were duplicated 100 times before they were stored in the (tumor \rightarrow cell) phase space file. The position of all duplicates was shifted towards the CR center, so their distance was reduced to $10\ \mu\text{m}$ and then rotated randomly around the Y-axis. The pre-step point was used as the base value of this calculation. The particle's momentum was rotated accordingly, while particle type and energy were stored as they were scored.

4.4.3. Cell

The cell was designed with 4T1 mouse tumor cells in mind. These are a popular choice for xenograft mouse models, since they are similar in several ways to triple-

negative human breast cancer cells. They metastasize in the mammary gland, even when implanted somewhere else, and the speed and further spreading of the tumors is similar to the human disease [83, 84]. As triple-negative breast cancer cells they represent one of the cancer categories that is hardest to treat. It means that the cells test negative for the expression of estrogen and progesterone receptors and the overexpression of the HER protein. Consequently, these tumors cannot be treated by common methods like endocrine therapy or trastuzumab and patients usually have to be treated with chemotherapy. As a result patients with triple-negative breast cancer usually have a poor chance of survival in comparison to other cancer types [85]. They are, therefore, of high interest for new treatment modalities [86, 87, 88, 89].

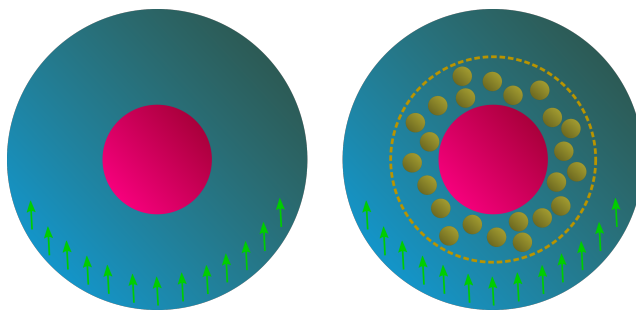


Figure 8.: **Sketch of the Cell simulations:** The cytoplasm is shown in blue, the nucleus in pink, and photons in green. Separate simulations are performed for each cell in the presence and absence of AuFeNPs. The nucleus includes a detailed cell model, where direct and indirect SSBs and DSBs are calculated. Source: Klapproth et al. (2021): Multi-scale Monte Carlo simulations of gold nanoparticle-induced DNA damages for kilovoltage X-ray irradiation in a xenograft mouse model using TOPAS-nBio [3].

According to the parameters of 4T1 cells the cells in my simulations had a diameter of $20\ \mu\text{m}$ and a nucleus diameter of $13.8\ \mu\text{m}$ [88]. Each simulation was performed once with and once without AuFeNPs, as illustrated in Figure 8. In the AuFeNP simulations 1 million NPs were placed randomly in an $100\ \text{nm}$ thick shell around the nucleus, which was located at the center of the cell. The respective algorithm was developed by modifying an algorithm to find any random point within a sphere based on polar coordinates [90]. It is explained in detail in section 4.4.4. The resulting concentration of AuFeNPs inside the cell is 0.225% by weight, which is relatively low compared to previous studies [41, 42], but more realistic considering that high

amounts of injected AuNPs have been shown to have repercussions for the whole body [33].

The physical assumptions for the cell simulations were largely based on previous publications to test the methodology with tried parameters and ensure comparability with other studies. As is very common in the field the cell was assumed to consist of water [20]. This also ensured that the precise Geant4-DNA physics and chemistry lists, which are also available in TOPAS-nBio, could be used [55, 91]. Consequently, the standard G4_WATER material was used for the cytoplasm. In the AuFeNPs, however, it was not possible to use Geant4-DNA models since cross sections for gold and other heavy materials had not been included in Geant4-DNA at the time of this study. Thus, Geant4 Livermore physics models were applied inside gold and Fe₂O₃. The minima for production cuts and electromagnetic range were both set to 15 eV and the maxima to 1 MeV, which is equivalent to having no upper limit at all since the maximum possible energy from the initial photon source had been 200 keV. The cut for electrons was set very low to 0.1 nm to ensure high accuracy in this vital step of our investigation. Two regions were defined in simulations with AuFeNPs to allow the application of different physics models in the same simulation. Region 1 included just the AuFeNPs and region 2 the rest of the cell including the nucleus. Unfortunately, there are still no available chemistry models for gold and Fe₂O₃ in Geant4, so the chemistry had to be shut off entirely inside region 1. This means no chemical interactions could be simulated within the NPs and chemical effects of the gold surface on its surroundings had to be neglected. This is a big limitation of this study since AuNPs have been shown to enhance the production of reactive oxygen species (ROS) and could, therefore, even have a reducing effect on cell survivability on their own [92, 93, 94, 95].

4.4.4. Randomization algorithm for AuFeNPs

The task of randomly distributing 1 million AuFeNPs around the nucleus with a maximum distance of 100 nm was substantial. The NPs had not only to be distributed uniformly, but also any overlap had to be avoided. In addition, the algo-

rithm had to place all AuFeNPs in a reasonable amount of time.

To avoid overlaps the algorithm had to first compute a random location as the newest AuFeNP center inside the placement area and then check all previously assigned AuFeNP centers to make sure the distance between those and the new one was large enough. Since the number of assigned AuFeNPs and, therefore, the number of necessary comparisons and potential overlaps rises over time, the computation time increases exponentially as a function of the number of previously placed NPs. Therefore, I decided to first divide the placement area into 100 sectors, denoted by S_1, S_2, \dots, S_{100} , and let the algorithm fill the sectors consecutively with 10,000 AuFeNPs each. That way the computation time for NP placement was decreased substantially in comparison to the same algorithm placing all 1 million AuFeNPs randomly inside the entire placement area.

However, this way of placing the NPs posed a new problem. Although the center of each AuFeNP was located inside a certain sector, its border could still protrude into one of the two neighboring sectors and overlaps with an AuFeNP that is placed there. Restricting the placement of NPs, so all of them are located fully within one sector, would be undesirable since it would imply that all sector borders would be “AuFeNP-free”, which would be unrealistic. Thus, the algorithm not only compared the newly computed AuFeNP location with the previous locations from the current sector, but also with the ones from the previously filled one. This means that e.g. for sector S_{11} each new AuFeNP center was computed repeatedly until it was more than 4 nm (i.e. the uniform AuFeNP diameter) away from each other AuFeNP center inside sector S_{11} , as well as from each one inside sector S_{10} . NP centers from the last sector to be filled (S_{100}) were not only compared to the ones from S_{99} , but also to the ones from S_1 , since S_{100} is the only sector bordering two previously filled ones.

To uniformly randomize a point within one of the sectors, I adjusted an existing algorithm for choosing a random point within a sphere based on polar coordinates [90]. Spherical coordinates can be used to describe a point in three-dimensional space and are defined by a radius r and two angles θ and φ . Assuming the nucleus

center is at (0,0,0) and the maximum distance from the nucleus is entirely inside the cell, a possible AuNP center in sector S_i is defined by the following equations:

$$\theta = 2\pi(i - 1) \div 100 + 2\pi \cdot R_1 \div 100 \quad (17)$$

$$\varphi = \arccos(2R_2 - 1) \quad (18)$$

$$r = r_{Nuc} + r_{NP} + R_3(d_{max} - 2r_{NP}) \quad (19)$$

R_1 , R_2 and R_3 are random values between 0 and 1, r_{Nuc} and r_{NP} denote the radii of the nucleus and one AuFeNP respectively and d_{max} the maximum distance of AuFeNPs from the nucleus. In our case $r_{Nuc} = 6.9 \mu\text{m}$, $r_{NP} = 2 \text{ nm}$ and $d_{max} = 100 \text{ nm}$. Angle θ of the AuFeNP center's polar coordinates is computed in equation (17). Its first summand ensures that points are only chosen in the current sector and in the second summand a random angle is chosen between 0 and $2 \cdot \pi \div 100$, which is the size of one sector. Angle φ is chosen in equation (18) as the arcus cosinus of a random number between -1 and 1, which produces an angle between 0 and π . In equation (19), r is set to a random point in interval $I = [r_{Nuc} + r_{NP}, r_{Nuc} + d_{max} - r_{NP}]$. This ensures that every NP, whose center's distance from the nucleus center (which is assumed to be (0,0,0)) is in I , is in its entirety outside the nucleus and inside the defined maximum range d_{max} . The polar coordinates are then converted to cartesian coordinates (x, y, z) by executing equations (20-22):

$$x = r \cdot \cos(\theta) \cdot \sin(\varphi) \quad (20)$$

$$y = r \cdot \sin(\theta) \cdot \sin(\varphi) \quad (21)$$

$$z = r \cdot \cos(\varphi) \quad (22)$$

As explained earlier, the NP center (x, y, z) is then compared to all previously computed AuFeNP locations in S_i . If $i > 1$, it is also compared to all locations in S_{i-1} and if $i = 100$, it is additionally compared to all locations in S_1 . Whenever the

distance between (x, y, z) and the center of the AuFeNP it is currently compared to is less than $2r_{NP}$, both NPs would overlap. In that case, (x, y, z) is discarded and equations (17-22) are performed again. Only if there is no overlap between (x, y, z) and all previous AuFeNPs, the coordinates are stored, and a NP is placed there.

4.4.5. Nucleus

The nucleus consists of a detailed mouse DNA model. It is a modification of the recently developed human DNA model for TOPAS-nBio by Zhu et al. [57, 96]. To fit to the genome of a male mouse inside a 4T1 cell, voxel count and structure has been adjusted so the nucleus had a diameter of 13.8 μm and included an overall amount of 5.19 Giga base pairs of DNA. The number of voxels per chromosome corresponds to the data of the Genome Reference Consortium and can be found in Table 2. 24,464 cubical voxels with a border length of 3.833 μm are arranged to a sphere building the nucleus. Each voxel is assigned to a certain chromosome. The nucleus partition schematic in chromosomes is illustrated in Figure 9. To reduce computing time the internal voxel structure is defined once in the programming and then applied for each nucleus voxel in the simulations. Every voxel contains 14 fibers, aligned along two parallel space filling 3D Hilbert curves with one iteration, as is visualized in Figure 10A [56, 97]. The half-cylindrical base volumes and quarter-cylindrical sugar-phosphate backbone volumes are surrounded by a hydration shell. This construct builds the DNA double helix, which is wrapped around the cylindrical histone protein complex, therefore, building the nucleosome. 51 nucleosomes are connected by nucleotide pairs to build the chromatin fiber, which is formed like a helix, as can be seen in Figure 10B. All in all, each chromatin fiber includes 15.15 kilo base pairs of DNA.

Geant4-DNA physics and chemistry lists could be applied in the entire nucleus since it included no AuFeNPs and the standard G4_WATER material could be used. The only exception is the DNA backbone, where the density of water was adjusted to 1.407 g/cm^3 [98]. DNA damage was divided into direct and indirect damage. Physical particles like photons and electrons produce direct damage by

Table 2.: **Number of voxels and base pairs per chromosome.** Source of genome data: Genome Reference Consortium (<https://www.ncbi.nlm.nih.gov/genome/52>). Source of the table: Klapproth et al. (2021): Multi-scale Monte Carlo simulations of gold nanoparticle-induced DNA damages for kilovoltage X-ray irradiation in a xenograft mouse model using TOPAS-nBio [3].

Chromosome ID	Voxels	Base pairs in Mbp
1 & 2	922	195.6
3 & 4	859	182.2
5 & 6	755	160.1
7 & 8	738	156.5
9 & 10	716	151.9
11 & 12	706	149.7
13 & 14	686	145.5
15 & 16	610	129.4
17 & 18	587	124.5
19 & 20	616	130.7
21 & 22	576	122.2
23 & 24	566	120.0
25 & 26	568	120.5
27 & 28	589	124.9
29 & 30	491	104.1
31 & 32	463	98.20
33 & 34	448	95.02
35 & 36	428	90.78
37 & 38	290	61.51
X	806	171.0
Y	430	91.20

depositing energy on their location, whereas indirect damage is produced by water radiolysis of chemical radicals. Parallel to the work of Zhu et al. (2020) the DNA backbone was the only region, where direct damage was scored [57]. A direct strand break (SB) was scored if at least 17.5 eV of energy was deposited by physical interactions within a single back bone during the same time range. The value of 17.5 eV was fitted by Lampe et al. and published in 2018 and has already been used in other MC studies [80, 81, 99]. The chemistry models of TOPAS-nBio are based on the ones from Geant4-DNA but use optimized chemistry parameters [100]. The duration of the chemical stage was set to 1.0 ns along the lines of previous studies [57, 99, 101, 102, 103]. I measured the number of produced chemical species for

all six particle types from the standard Geant4-DNA chemistry extension that were included in the simulations. They were hydrogen radicals ($\text{H}\cdot$), molecular hydrogen (H_2), hydrogen peroxide (H_2O_2), hydronium (H_3O^+), solvated electrons (e_{aq}) and two types of hydroxyls (OH) - hydroxide (OH^-) and hydroxyl radicals ($\cdot\text{OH}$). We assumed that no water radiolysis occurs inside DNA regions, so chemical species there were immediately killed, as were $\text{H}\cdot$, e_{aq} and $\cdot\text{OH}$ diffusing into DNA regions. Indirect SBs could only be produced by $\cdot\text{OH}$ radicals entering the DNA backbone with a probability of 40% [79, 81].

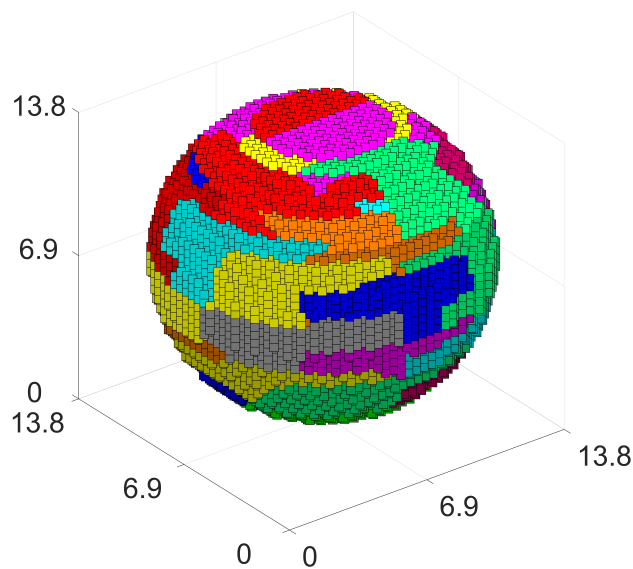


Figure 9.: **Voxelized nucleus model:** The nucleus is divided into 40 chromosomes, each represented by one color. Axes are displayed in μm . Source: Klapproth et al. (2021): Multi-scale Monte Carlo simulations of gold nanoparticle-induced DNA damages for kilovoltage X-ray irradiation in a xenograft mouse model using TOPAS-nBio [3].

There are direct SBs generated by physical interactions and indirect SBs produced by water radiolysis. If two SBs occur on opposing DNA strands with a distance of 10 or fewer base pairs, they are defined as an DSB, all other SBs as SSBs. Based on the underlying SBs, the DSBs are classified into direct, indirect and hybrid DSBs.

In addition, the overall dose, which was deposited inside the nucleus in consequence of physical interactions, was measured in each simulation. Through that,

the dose enhancement ratio could be calculated for each scenario.

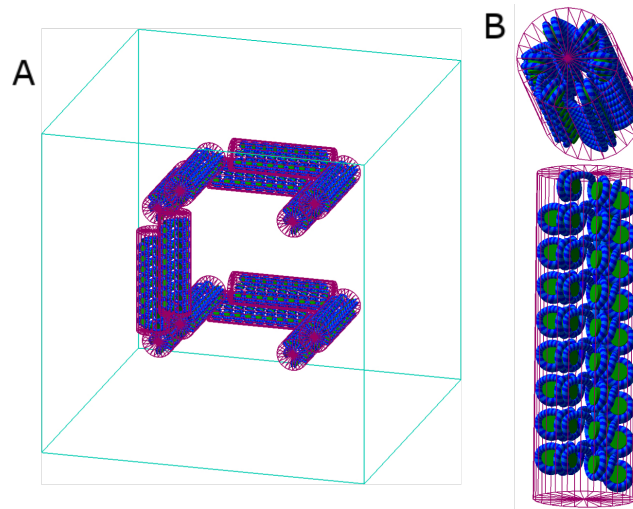


Figure 10.: **TOPAS visualization depicting voxel structure:** **A** displays one voxel including 14 fibers, which are placed alongside two parallel first order 3D Hilbert space filling curves. **B** provides a closer look at one fiber from two different angles. Visible elements are histones (green) and hydration shells for each DNA helix (blue). Source: Klapproth et al. (2021): Multi-scale Monte Carlo simulations of gold nanoparticle-induced DNA damages for kilovoltage X-ray irradiation in a xenograft mouse model using TOPAS-nBio [3].

4.5. Publication summary: Multi-scale Monte Carlo simulations of DNA damages with and without AuNPs

Computer simulations of *in vivo* experiments can be very valuable since they can be used to calibrate the parameters before performing the experiments and eventually reduce the amount of required animals and resources. For studies involving ionizing radiation Monte Carlo simulations are a popular tool. Previously, those simulations were usually restricted to a certain area, for example, inside the nucleus or the immediate surroundings of a NP. I developed a new methodology that allows the inclusion of a whole mouse model in the simulations and still yields detailed results on the amount of DNA damage in single cells. The method and its first results were published in *Cancer Nanotechnology* under the title *Multi-scale Monte Carlo simulations of gold nanoparticle-induced DNA damages for kilovoltage X-ray*

irradiation in a xenograft mouse model using TOPAS-nBio [3].

The simulations were performed in TOPAS v3.2 for Linux machines and Geant4 v10.5p1. I developed all the TOPAS parameter files and most of the extensions. I also came up with all the solutions to the problems regarding the variance and randomization of duplicated particles and NPs. Authorship of each file has been documented in its headlines. They have been made available to the public under the following link: https://github.com/AKlapproth/MultiScale_AuNP_TOPAS. The simulations were split into three steps, each representing a different scale. Phase spaces were used to transfer particles to the next step.

For the first step we used the model of a 21 g mouse provided by Tianwu Xie. I equipped the code that inserts the model into the simulation with the feature to insert a tumor at any location. In that way a mammary gland tumor was inserted near the left hind leg. It was irradiated by either a 100 kVp or a 200 kVp photon beam.

The second step was the tumor itself: 3 locations at different depths were defined as cells. Their parameters were chosen to simulate 4T1 mouse tumor cells.

The third step were simulations inside single cells. Each cell simulation was performed both with and without NPs. We chose to use NPs with a gold coating and an Fe₂O₃ core (AuFeNPs), a type of NP that was already used for *in vivo* experiments. Their iron oxide core brings both diagnostic and theranostic advantages since the NPs can be traced via MRI scan. The cell nucleus includes a detailed DNA model, which was established by Hongyu Zhu for human cells and adjusted to murine cells by me.

Results were in the form of strand breaks (SBs), dose deposited inside the nucleus and produced chemical species. Dose and the number of both SBs and chemical species were all enhanced in the presence of AuFeNPs for all scenarios. The depths inside the tumor also played a visible role in the results as all three of the measurements were reduced the farther away the cell was from the radiation source.

Although the concentration of NPs was relatively low compared to previous AuNP

studies we could show their radiosensitization effect on tumor cells. The newly developed methodology proved itself useful by producing valuable and understandable results. Due to its many adjustable parameters it can be used in the future for multiple different settings of *in vivo* Monte Carlo studies with or without NPs involving ionizing radiation.

5. Discussion and Literature Review

5.1. SPIONs

The application of NPs in the field of tumor therapy requires a lot of preparation since a plethora of factors could play an important role. In the first part of this work we investigated how the injection mode can affect the biodistribution of NPs, in particular that of SPIONs. Possible applications of SPIONs in oncology are ample and range from contrast agents in MRI diagnostics to various utilizations in tumor therapy [104].

Due to their ferromagnetic properties SPIONs can be used to deliver drugs to a desired destination using an external magnet [105, 106]. Through this Abed et al. (2019) successfully assembled magnetic NPs inside a CT26 tumor in mice for radiosensitization [107]. Inside tumors SPIONs can be used to deliver chemotherapeutic drugs amongst others [108]. These and other promising results indicate that SPIONs can be used to deliver therapeutic agents directly into the tumor and thereby reduce both the required dose and toxicity to surrounding normal tissues [109].

SPIONs themselves can also be used as theranostic agents [66]. An alternating magnetic field can be applied to induce Brownian and Néel relaxation, causing the SPIONs to heat up and thus induce hyperthermia inside the tumor [110]. Temperatures around 41-46 °C have been shown to lead to an increased failure in cell productivity and eventual apoptosis [111]. Higher temperatures can cause instant cell death and severe damage to the tissue [112]. If applied correctly this can be a valuable tool to treat cancer cells in the future.

Recent studies on SPIONs have produced promising results in the field of glio-

blastoma. One of the main obstacles for drug assisted brain tumor therapy is the blood-brain barrier (BBB) [113]. In 2016, Huang et al. showed the possibility to allow SPIONs breach the BBB by magnetizing the target area [114]. Sukumar et al. (2019) successfully increased the efficiency of targeted NP therapy inside the brain of mice through intranasal delivery [115]. Furthermore, due to their small size even SPIONs are more likely to breach the BBB than most other theranostic agents [113]. A small percentage of the SPIONs in our study could be measured inside the brain [1, 2]. This provides hope that with the inclusion of tumor targeting, i.v. injected SPIONs have the potential to be clinically used to support the treatment of brain tumors.

5.2. PBPK model

The presented PBPK model has proven helpful in predicting the biodistribution of SPIONs after injection. It shows a similar basic structure as the previously published PBPK model by Henrique Silva et al. (2017), however, we added the tumor and a more elaborate alimentary tract [116]. The differences in tumor concentration over time between intratumoral and i.v. injection were particularly visible in the results. The model can also predict the continuing progression of SPION concentrations after the last measurement point and shows that liver and spleen are the most likely eventual destination for most NPs in each scenario assuming a limited amount of time. Since there is no additional uptake of SPIONs into the system as a whole after the initial injection, there would never occur an equilibrium as the SPIONs are slowly excreted through the alimentary track. Yet it would take an extensive amount of time to excrete all SPIONs from the system. The body parts, where they are accumulated before excretion, can, therefore, be regarded as their destination from a biological point of view. The results of the simulations underline the importance of tumor targeting for i.v. injected SPIONs.

The applied parameter estimation methods delivered satisfactory results and we could produce a good fit for the experimental data. Raue et al. (2013) showed in

a comparison between estimation strategies that a multi-start approach, as I also chose to use in this work, produced the best results for complex biological systems, while also performing swiftly [117].

5.3. AuFeNPs

A major limitation of SPIONs is their agglomeration tendency due to magnetic attraction, van der Waals forces and high surface energy [118]. Agglomerated SPIONs cluster together and lose a big portion of their functionality [66]. That is why various inorganic coatings have been tested to counteract clustering and in some cases even add further helpful characteristics to the NPs [119]. Those coatings include silica and numerous noble metals [120, 121, 107, 112]. Especially gold-coated SPIONs are popular research targets [119]. The coating adds functionalities such as high X-ray absorption, biocompatibility and increased stability as reported in recent reviews [119, 120, 122]. We chose to use this type of NP (i.e. AuFeNP) for our simulations and our planned *in vivo* experiments, in particular, because of the radiosensitizing potential of the gold coating and its resulting radiotherapy applications.

5.4. MC simulations

The MC simulation methodology presented in this thesis was built on the preceding results of many other research groups. The voxelization codes used to insert the mouse model in the TOPAS simulations was an extension of the work presented by Zhu et al. (2020) to place DNA containing voxels inside a nucleus [57, 96]. A possible improvement would be to use G4VNestedParameterisation instead of G4VPVParameterisation as navigation algorithm, since Schuemann et al. showed in 2012 that G4VNestedParameterisation requires less simulation time and memory space [52]. This would allow for an increase of initial photon beams and, therefore, reduce the number of necessary duplications while storing particles in the phase space files. The work of Zhu et al. (2020) was also the basis for the DNA model building the nucleus in our simulations, as were the radiobiology studies of McNamara et al.

(2017 and 2018), in which many useful cell geometry components were developed and tested [56, 57, 96, 123]. Another important part of our simulations were the water radiolysis models used to compute DNA damages caused by chemical reactions. They were first introduced to Geant4-DNA by Karamitros et al (2011 and 2014) [124, 125]. Ramos-Méndez et al. (2018) implemented those models in TOPAS-nBio, where they tested them and even improved some of the parameters [100]. In 2019 Rudek et al. published their work, in which they tested the radio-enhancement caused by AuNPs using TOPAS-nBio with the mentioned chemistry models [80]. All these previous studies were important sources of data to compare with our results for validation of our methodology. Through this we found that the ratios between direct and indirect damage, as well as the proportions of DSBs and SSBs, were similar to previous studies. In comparison to other studies like the ones from Sung et al (2017 and 2018), we were using much smaller concentrations of NPs and could still measure a clear increase in dose, DNA damage and chemical species [41, 126]. This gives hope that MC simulations are on a right path towards realistically simulating AuNP enhanced radiotherapy since there is still a discrepancy between simulation results and *in vivo* data, where concentrations as low as 10 μg gold per g body weight have shown effective radiosensitization [127].

5.4.1. Limitations

Several limitations regarding the models used for our simulations should be kept in mind. Recent comparisons between different MC simulation codes conducted by Li et al. (2020) and Rabus et al. (2021) show that there is a significant discrepancy between those tools, when comparing results from several work groups that used their code of choice on the same simple task of irradiating a single AuNP [4, 5, 6]. The Geant4-DNA models have some proven uncertainties as well. Thomson and Kawrakow (2011) could show an uncertainty of 5% for 1 keV electrons in water regarding position and momentum, which increases to 17-20% at 100 eV [128]. Chemical and biological parameters are difficult to establish for general purposes and are usually derived from experimental reactions performed *in vitro*. Therefore, they can

show even larger uncertainties simulations like ours. In 2020 Zhu et al. estimated discrepancies of up to 34% for SSBs and 16% for DSBs in their simulations with the DNA model on which we based our nucleus geometry. In addition, they found high sensitivity of the results to the threshold energy of 17,5 eV and the probability of radicals for producing an indirect SB, which was set to 40% [96]. It is safe to assume that these uncertainties apply to our work as well, especially considering that both projects produced similar results regarding overall trends and proportions of direct and indirect DNA damage.

Another limitation is the fact that Geant4-DNA models were not applicable to gold or Fe_2O_3 at the time of this study, which caused problems for our setup for both physical and chemical interactions. In terms of physics lists we had to use Livermore models inside AuFeNPs and possibly switch between physics lists within the same simulation based on the location of the current track. Livermore models have been shown to produce unsatisfying results for energies below 100 eV, which is a very important range for our simulations. This is the case because a large amount of DNA damage is produced by small energy electrons after a full Auger cascade [129]. Improvement of gold cross sections and the respective physics models will, therefore, be an important step in the future of our research field.

The lack of Geant-DNA chemistry models for gold and Fe_2O_3 especially impacts the indirect damage results since at time of this study there were no other chemistry models to which we could switch. Consequently, all chemical tracks were killed as soon as they reached an AuFeNP, which is equivalent to them being absorbed by the NP without any further reaction. Arguably, this leads to a notable underestimation of indirect damage as there are several findings that suggest that the gold surface of our AuFeNPs would rather increase the amount of indirect damage in their surroundings. It has been well established that the surface chemistry of gold inside cells can enhance the production of ROS, which can lead to oxidative stress and a decrease in cell survivability [92, 93, 94, 95]. Gold can also enhance the chemical activity in water, most likely through activation of its atoms due to superoxides [130]. To make NPs viable for *in vivo* studies they are often functionalized with an

additional coating. One of the most common choices is the polymeric coating with polyethylene glycol (PEG). NPs with this coating repel each other, which ensures a good spatial distribution of PEG-coated NPs, which is desired in most cases [131]. In 2011 Xiao et al. found that coating gold layered NPs can reduce their radiosensitization effect and also cause additional chemical reactions in their surrounding area [132]. This adds even more chemical action in the surface area of AuFeNPs, which we can currently not consider in our simulations. The chemical characteristics of different NP coatings thus require further investigation. Not only did we have to ignore several known chemical interactions around AuFeNPs in our current simulations, they even worked as a radical-scavenger, due to the complete lack of available chemistry models. This means that through the mechanism of chemical species being killed when encountering an AuFeNP they reduce the overall production of some chemical species [80]. We encountered this phenomenon too, as can be seen in Table 3 of *Multi-scale Monte Carlo simulations of gold nanoparticle-induced DNA damages for kilovoltage X-ray irradiation in a xenograft mouse model using TOPAS-nBio* [3]. In addition to termination of the radicals on the AuFeNP surface this can be explained by a change in energy disposition caused by the NPs, chemical species not being able to be produced inside AuFeNPs, or the termination of required reaction partners [80].

6. Outlook

Our combined results leave no doubt that AuFeNPs are very promising agents for the improvement of cancer therapy with radiation. An important next step towards viability for clinics will be the inclusion of tumor targeting. As mentioned in the introduction Hsp70 has been shown to be a suitable target for many tumor types. AuFeNPs conjugated with the cmHsp70.1 antibody, which was designed in our work group, are safe and show an increased uptake rate for the tumor [34, 35, 36]. This leads to a higher accumulation of AuFeNPs inside the tumor and consequently decreased concentrations of NPs in all other organs and healthy tissues. Targeting can also be included in the PBPK model by introducing a factor or appropriate nonlinear function modifying the tumor uptake rate. Lastly, if we would assume a higher NP concentration inside tumor cells, we could adjust the MC simulations accordingly and, therefore, measure the effect on cell survival.

Another important next step will be the comparison of our MC simulation results to experimental data. Alternations in the biodistribution of NPs through the mentioned targeting first have to be measured in *in vivo* experiments. This data can then be used to adjust the PBPK model appropriately. The macro scale MC simulations, including a voxel mouse model, could be validated by *in vivo* dosimetry results on mice. This would also feature an opportunity to measure the radiation dose in vital organs to optimize the incident angle of the initial source to minimize negative side effects. Since DNA damages were computed in separate simulations in single cells they can be compared to *in vitro* cell studies, including our AuFeNPs. Through the application of a mechanistic model developed by McMahon et al., DNA damage in the form of SSBs and DSDs can be translated into an estimation of cell survival

[133]. Recently they even developed the possibility to directly read out data in the SDD format, which we also used for DNA damage output in our study [134]. The resulting cell survivability data can be directly compared to *in vitro* experimental results on irradiated cells with and without AuFeNPs.

Due to the separation into several steps an advantage of our multi-scale methodology is that many parameters of the setup are comprehensible and individually adjustable, as is the geometry of each individual step. The geometry of the tumor step, for example, was kept fairly simple in this work though there are ways to improve it in the future. It is a well-known fact that tumors in real life can be heavily heterogeneous in terms of all important phenotypic features [135]. This has shown to impact their radiosensitivity, which thus can differ vastly among different regions within the same tumor [135, 136, 137, 138]. Mathematical models predict that through “survival of the fittest” this causes the entire tumor to become more radioresistant over the course of radiotherapy treatment [138]. Tumor heterogeneity could be added by changing water density in the tumor step for certain regions or assuming modified parameters in the cell step. Possible cell parameter adjustments to model increased radioresistancy include an increased necessary amount of deposited energy for direct SBs, a reduced probability for indirect SBs or a higher DNA repair coefficient when calculating the cell survival rate. Another factor that could be included is the distinction between non-necrotic and necrotic areas, which is a geometric measure that can be considered for treatment planning [139].

As mentioned before the improvement and addition of detailed physics and chemistry models for small energy tracks in tissue and gold will be crucial for the advancement of Monte Carlo simulations of DNA damage. Results with novel gold cross-sections to be included in the Geant-DNA toolkit have already been reported, however, they were not yet available to the public at the point of this study [140, 141]. At some point simulations should also include chemical radicals produced by the gold surface inside the cytoplasm because they might be part of the reason why AuNPs are so effective in reducing cell survivability after irradiation.

As a final point it should be mentioned that the multi-scale Monte Carlo method-

ology, which was presented in this work, has many possible applications apart from studies on the effect of NPs on x-ray irradiation. The radiation type can be easily swapped for others like MeV photons or protons to study the DNA damage they would cause with or without NPs. The mouse model can also be replaced by other voxel models, such as a human phantom, and other tumor or cell parameters can be chosen to simulate other types of cancer cells. The user friendliness of TOPAS and the transparent modeling structure make it easy to adjust the methodology to a wide variety of studies.

A. Included publications

A.1. A new pharmacokinetic model describing the biodistribution of i.v. and intratumorally administered superparamagnetic iron oxide nanoparticles (SPIONs) in a GL261 xenograft glioblastoma model

Authors: A.P. Klapproth, M. Shevtsov, S. Stangl, W.B. Li, G. Multhoff

A.1.1. Article

A New Pharmacokinetic Model Describing the Biodistribution of Intravenously and Intratumorally Administered Superparamagnetic Iron Oxide Nanoparticles (SPIONs) in a GL261 Xenograft Glioblastoma Model

This article was published in the following Dove Press journal:
International Journal of Nanomedicine

International Journal of Nanomedicine downloaded from <https://www.dovepress.com/> by 185.22.143.171 on 30-Jun-2020
For personal use only.

Alexander P Klapproth^{1,2,*}
Maxim Shevtsov^{1,3-7,*}
Stefan Stangl¹
Wei Bo Li²
Gabriele Multhoff¹

¹Center for Translational Cancer Research Technische Universität München (TranslaTUM), Klinikum Rechts Der Isar, Munich, Germany; ²Institute of Radiation Medicine, Helmholtz Zentrum München, German Research Center for Environmental Health (GmbH), Munich, Germany; ³Institute of Cytology of the Russian Academy of Sciences (RAS), St. Petersburg, Russia; ⁴Department of Biotechnology, First Pavlov State Medical University of St. Petersburg, St. Petersburg, Russia; ⁵Almazov National Medical Research Centre, Russian Polenov Neurosurgical Institute, St. Petersburg, Russia; ⁶National Center for Neurosurgery, Nur-Sultan, Kazakhstan; ⁷Department of Biomedical Cell Technologies, Far Eastern Federal University, Vladivostok, Russia

*These authors contributed equally to this work

Background: Superparamagnetic iron oxide nanoparticles (SPIONs) have displayed multifunctional applications in cancer theranostics following systemic delivery. In an effort to increase the therapeutic potential of local therapies (including focal hyperthermia), nanoparticles can also be administered intratumorally. Therefore, the development of a reliable pharmacokinetic model for the prediction of nanoparticle distribution for both clinically relevant routes of delivery is of high importance.

Materials and Methods: The biodistribution of SPIONs (of two different sizes – 130 nm and 60 nm) radiolabeled with zirconium-89 or technetium-99m following intratumoral or intravenous injection was investigated in C57/Bl6 mice bearing subcutaneous GL261 glioblastomas. Based on PET/CT biodistribution data, a novel pharmacokinetic model was established for a better understanding of the pharmacokinetics of the SPIONs after both administration routes.

Results: The PET image analysis of the nanoparticles (confirmed by histology) demonstrated the presence of radiolabeled nanoparticles within the glioma site (with low amounts in the liver and spleen) at all investigated time points following intratumoral injection. The mathematical model confirmed the dynamic nanoparticle redistribution in the organism over a period of 72 h with an equilibrium reached after 100 h. Intravenous injection of nanoparticles demonstrated a different distribution pattern with a rapid particle retention in all organs (particularly in liver and spleen) and a subsequent slow release rate.

Conclusion: The mathematical model demonstrated good agreement with experimental data derived from tumor mouse models suggesting the value of this tool to predict the real-time pharmacokinetic features of SPIONs in vivo. In the future, it is planned to adapt our model to other nanoparticle formulations to more precisely describe their biodistribution in in vivo model systems.

Keywords: mathematical modeling, SPIONs, superparamagnetic iron oxide nanoparticles, pharmacokinetic model, glioblastoma, biodistribution

Background


Recent developments in nanotechnology have introduced novel diagnostic and therapeutic (ie, theranostic) applications of nanoparticles in translational and clinical oncology after intravenous injection.¹ Superparamagnetic iron oxide nanoparticles

Correspondence: Maxim Shevtsov;
Wei Bo Li
Email maxim.shevtsov@tum.de;
wli@helmholtz-muenchen.de

submit your manuscript | www.dovepress.com
DovePress    
<https://doi.org/10.2147/IJN.S254745>

International Journal of Nanomedicine 2020:15 4677–4689

4677

 © 2020 Klapproth et al. This work is published and licensed by Dove Medical Press Limited. The full terms of this license are available at <https://www.dovepress.com/terms.php> and incorporate the Creative Commons Attribution – Non Commercial (unported, v3.0) License (<http://creativecommons.org/licenses/by-nc/3.0/>). By accessing the work you hereby accept the Terms. Non-commercial uses of the work are permitted without any further permission from Dove Medical Press Limited, provided the work is properly attributed. For permission for commercial use of this work, please see paragraphs 4.2 and 5 of our Terms (<https://www.dovepress.com/terms.php>).

(SPIONs), specifically, have been identified as potential candidates for the development of innovative anti-tumor therapies due to their beneficial physico-chemical properties, biodistribution, biocompatibility and easy fabrication and functionalization.^{2,3} Apart from intravenous injection, SPIONs can also be injected intratumorally to locally increase the temperature inside tumors after hyperthermia treatment.⁴⁻⁷ Upon exposure to an external alternating magnetic field (AMF) and due to the Brownian and Néel relaxation and hysteresis loss, which is accompanied with the generation of thermal energy, a rise of the local tissue temperature up to 41–43 °C can be achieved.⁸ Several studies reported the therapeutic potency of hyperthermia in preclinical models.⁹⁻¹³ Apart from magnetic hyperthermia, other applications of functionalized SPIONs in translational oncology have been reported,¹⁴ including the delivery of chemotherapeutic drugs, siRNA and small molecules.^{3,14-19} In a recent study of our group SPIONs were decorated with the pro-apoptotic serine protease granzyme B (GrB-SPIONs). Administration of GrB-SPIONs resulted in significant delay of tumor progression and an increased overall survival in tumor-bearing animals.³ Furthermore, the addition of photosensitizing agents to the composition of iron oxide nanoparticles enabled multimodal applications for both magnetic resonance imaging (MRI) and photothermal therapy.²⁰ In past decades, intravenous and intratumoral administrations of SPIONs have been extensively studied.²¹⁻²⁴ Compared to an intravenous injection mode, a local delivery of nanoparticles can significantly increase the concentrations of nanoparticles inside the tumor, while decreasing unfavorable off-target effects in healthy tissues.

The growing interest in nanoparticles as a vehicle for a targeted delivery of pharmaceutical agents have led to a vast increase in the development of novel physiologically based pharmacokinetic (PBPK) models.^{25,26} These have been proven as valuable tools to simulate transportation kinetics of nanoparticles inside the body and to fill knowledge gaps for tissues that do not allow reliable measurements.²⁷ Several reviews have been published during the last decade summarizing the vast amount of novel PBPK models.^{26,28-32} Partially responsible for the constant need of new and adjusted models is the large variability in pharmacokinetic behavior of nanoparticles differing in structural properties such as size, shape, material or coating compositions.³² For choosing an appropriate model it is crucial to take into account not only biokinetic properties of the nanoparticles and the

biological environment, but also the amount of available data. Many existing models split the circulating blood into two compartments, namely venous and arterial flux.³³⁻³⁶ As measurements in most cases lack differentiation between these two compartments, the ratio between their respective concentrations can only be estimated. In practice, this is done either by fixing the ratio to a certain value, based on previous knowledge^{33,36} or basically an additional degree of freedom for fitting the model parameters.^{34,35} The latter should be avoided, when there are no reliable measurements available that validate the resulting ratio, as it rises the risk of overfitting. Therefore, in our model blood was treated as one compartment. An important factor present in the majority of PBPK models for nanoparticles³³⁻³⁷ is the partition coefficient of blood and tissue which describes the ratio between concentration in a compartment and its outflow into the bloodstream.³⁸ However, due to the unique targeting properties of SPIONs in our experiment, we made the assumption that they do not accumulate within the tissue of organs, but enter the iron metabolism. This also reduces the degrees of freedom in the parameter estimation by omitting unnecessary features, bringing the model in line with the extent of available data.

In the present study, we have established a new pharmacokinetic model that mimics biological features of SPIONs after intratumoral or intravenous injection and prevents overfitting by focusing on predominant pathways specific to these nanoparticles. The model helps to understand the biodistribution of SPIONs over time and allows first predictions about their destiny inside the body after the two different injection routes.

Methods

Experiments

Superparamagnetic Iron Oxide Nanoparticles

The iron oxide dextran composite nanoparticles (Perimag[®]-COOH) with a hydrodynamic diameter of 130 nm and 60 nm were obtained from Micromod Partikeltechnologie GmbH. The zeta potential of nanoparticles characterized by electrophoretic measurements constituted -13.4 mV. The colloidal stability of these nanoparticles was analyzed for Perimag[®]-COOH formulations in H₂O distilled water, PBS buffer, and 5% human serum albumin (HSA) solution. Dynamic light scattering (DLS) measurements did not reveal any significant changes of the size distributions over a period of 3 months.

Before intratumoral or intravenous injection, particles were resuspended in PBS buffer (pH = 7.4).

Cells

Mouse GL261 glioblastoma cells were provided by Tumorbank Deutsches Krebsforschungszentrum (Heidelberg, Germany). Cells were cultured in RMPI-1640 medium supplemented with 10% fetal calf serum (FCS), 1 mM sodium pyruvate, 2 mM L-glutamine, and antibiotics (100 µg/mL streptomycin, 10 IU/mL penicillin) at 37 °C in 5% CO₂-incubator. For experiments, single-cell suspension was obtained employing Trypsin/0.53 mM EDTA.

Animals

Female, 8–10 weeks old C57Bl/6 mice were purchased from Charles River (Sulzfeld, Germany). All mice were kept and bred under specific pathogen-free conditions in accordance with the guidelines of the Federation of European Laboratory Science Association (FELASA). All animal experiments were performed in compliance with European Union law and approved by the ethical committee of First Pavlov State Medical University of St. Petersburg (St. Petersburg, Russia).

Glioblastoma Mouse Model

C57Bl/6 mice were anesthetized via i.p. injection of fentanyl 0.05 mg/kg, midazolam (5 mg/kg) and medetomidine (0.5 mg/kg). GL261 cells (5×10^6 cells suspended in 100 µL of phosphate-buffer solution) were injected into the right flank. After reaching a size of 50 mm³, nanoparticles were injected either intravenously or intratumorally into the mice. Intravenous injection of nanoparticles was performed through the tail vein employing 0.3 mL insulin syringes (30 G) at a speed of 25 µL/min (total volume of injected solution constituted 200 µL). Intratumoral injections were performed using 0.3 mL insulin syringes (30 G) at a speed of 4 µL/min.

Radiolabeling of SPIONs with Zirconium-89 [⁸⁹Zr]

Radiolabeling of the nanoparticles with ⁸⁹Zr was performed as described previously.³⁹ Briefly, 35.6 MBq of Zirconium-89-oxalate (⁸⁹Zr⁴⁺ in 1 M oxalic acid, PerkinElmer) was added to an Eppendorf tube with subsequent addition of Chelex-treated water (200 µL). The pH was raised to 8 employing 1 M Na₂CO₃ (aq.). Following addition of Chelex-36, treated water SPIONs Perimag[®]-COOH (400 µL, 50 mg Fe/mL) were added for the co-incubation period of 60 minutes at 100 °C. After cooling of the reaction to 22 °C, DTPA (50 µL, 10 mM (pH 7.5)) were added and left to stir at room

temperature (for 30 minutes). The nanosuspension was purified employing size exclusion chromatography (SEC) (PD10 Sephadex, G25) and eluted with fractions of sterile PBS (recovery = 81%). Radiolabeled ⁸⁹Zr-Perimag[®]-COOH nanoparticles were diluted at a concentration of 20 mg Fe/mL employing sterile PBS with subsequent characterization using a nanosizer DLS (size constituted 134 ± 4.8 nm; Z-potential constituted -4.11 mV). Decay of ⁸⁹Zr was calculated employing www.radprocalculator.com/Decay.aspx with Gaussian filtering of 0.8.

PET/CT Imaging of Intratumorally Administered SPIONs

⁸⁹Zr-Perimag[®]-COOH solution (1.76 mg Fe/kg, 100 µL) was intravenously injected into the tail vein of the mice. PBS solution (100 µL) was used as control. In case of an intratumoral administration, nanoparticles were injected in an injection volume of 0.34 µL/mm³ glioblastoma nodule. At designated time points animals were anesthetized with isoflurane (2% in O₂) and placed on a preheated bed (set at 38 °C) of the scanner. Whole body static PET scans were acquired employing nanoScan PET/CT (Mediso, Budapest, Hungary) with subsequent CT image acquisition. PET images were acquired employing 1–5 coincidence mode and recorded for 20 minutes. CT images were acquired at 300 ms exposure time in 720 projections with an acquisition time of 7 minutes employing a 50 kVp X-ray source. Subsequently, PET images were reconstructed by Tera-TomoTM 3D PET reconstruction software (Mediso version 2.01). Nucline software (Mediso version 2.01) was used to reconstruct CT images with a voxel size of 68 × 68 × 68 mm³. VivoQuant software (InviCRO version 1.23patch3) was used for three-dimensional (3D) visualization and image analysis.

Biodistribution Analysis of the SPIONs

Animals under anesthesia employing Monastat Carter Multi-Channel Precision Pump (Barant Company, Montreal) were transcatheterially perfused with 0.1 M phosphate buffer (PB) to eliminate the blood from the tissues and organs. Briefly, following thoracotomy and exposure of the beating heart, perfusion tube was inserted into the left ventricle (another incision was performed in the right atrium) for perfusion of 200 mL of PB for 20 minutes. The obtained organ samples were employed for subsequent biodistribution analysis. Each tissue sample was weighed and counted employing a gamma counter (LKB computerized gamma for ^{99m}Tc studies, Wizard 2480 PerkinElmer for ⁸⁹Zr studies), together with standards prepared from

a sample of radiolabeled SPIONs. For each tissue type the percent of injected dose per gram (%ID/g) of tissue was calculated (after 24, 48 and 27 hours for intratumorally injected ^{89}Zr -Perimag[®]-COOH SPIONs; after 80 minutes and 24 hours for i.v. injected ^{89}Zr -Perimag[®]-COOH SPIONs; after 24 hours for i.v. injected $^{99\text{m}}\text{Tc}$ -ferucarbo-tran). To exclude the predominant accumulation of nanoparticles in macrophages at the tumor site the glioma sections were additionally stained for CD11b+ tumor-associated macrophages (TAMs) (Abcam, USA).

Pharmacokinetic Model

To describe the biodistribution of nanoparticles within mice after injection, a pharmacokinetic model was established. In this model the body is divided into distinct compartments (here: blood, organs and tumor), each describing a possible location of the investigated substance (here: SPIONs).

Model Structure

The transition between compartments is in this case described by linear, first-order ordinary differential equations with constant coefficients. Figure 1 shows the model structure and relation between different compartments. Equations (1–14) describe the change of the amount of SPIONs in each respective compartment as a function of time. The set of compartments is composed of blood and body parts, the latter including organs and the tumor. Blood is assumed to be the predominant way for transport of the nanoparticles between body parts. Therefore, the model differs from previous pharmacological models for both humans^{40,41} and mice.^{42–44} This systemic circulation (Figure 1B) is coupled with transport via the alimentary tract (Figure 1C).^{45,46} Iron contained in in vivo administered SPIONs is predominantly included into the normal iron metabolism and therefore remains inside the body for a long-term period compared to other formulations of nanoparticles. Hence, excretion via urine was left out of the model. Each transition rate is described by one constant kinetic parameter $k_{i,j}$, with unit $1/t$, as no saturation effects or delay are expected. Since the SPIONs were administered intratumorally, the initial values $S(0h)$ for each compartment other than the tumor were set to 0. As the data points were in the form of concentrations and normalized, the initial value for the tumor $S_{tumor}(0h)$ was set as $(w_{tumor} \cdot 100\%/g)$, with w_{tumor} denoting the mean tumor weight, which was presumed to be constant in the course of the experiment. The

normalization of the data implies that 100% stands for the measurable dose released by the initially injected amount of SPIONs per gram tissue. The model is described by the following ordinary differential equations:

$$\dot{S}_{blood}(t) = \sum_{i=2}^{14} (k_{i,1} \cdot S_i(t) - k_{1,i} \cdot S_{blood}(t)) \quad (1)$$

$$\dot{S}_{tumor}(t) = -k_{2,1} \cdot S_{tumor}(t) + k_{1,2} \cdot S_{blood}(t) \quad (2)$$

$$\begin{aligned} \dot{S}_{liver}(t) &= -k_{3,1} \cdot S_{liver}(t) + k_{1,3} \cdot S_{blood}(t) \\ &\quad - k_{3,8} \cdot S_{liver}(t) \end{aligned} \quad (3)$$

$$\dot{S}_{spleen}(t) = -k_{4,1} \cdot S_{spleen}(t) + k_{1,4} \cdot S_{blood}(t) \quad (4)$$

$$\dot{S}_{kidney}(t) = -k_{5,1} \cdot S_{kidney}(t) + k_{1,5} \cdot S_{blood}(t) \quad (5)$$

$$\dot{S}_{heart}(t) = -k_{6,1} \cdot S_{heart}(t) + k_{1,6} \cdot S_{blood}(t) \quad (6)$$

$$\dot{S}_{lung}(t) = -k_{7,1} \cdot S_{lung}(t) + k_{1,7} \cdot S_{blood}(t) \quad (7)$$

$$\begin{aligned} \dot{S}_{intestine}(t) &= -k_{8,1} \cdot S_{intestine}(t) + k_{1,8} \cdot S_{blood}(t) \\ &\quad + k_{3,8} \cdot S_{liver}(t) - k_{8,9} \cdot S_{intestine}(t) \\ &\quad + k_{10,8} \cdot S_{stomach}(t) \end{aligned} \quad (8)$$

$$\begin{aligned} \dot{S}_{colon}(t) &= -k_{9,1} \cdot S_{colon}(t) + k_{1,9} \cdot S_{blood}(t) \\ &\quad + k_{8,9} \cdot S_{intestine}(t) - k_{Exc} \cdot S_{colon}(t) \end{aligned} \quad (9)$$

$$\begin{aligned} \dot{S}_{stomach}(t) &= -k_{10,1} \cdot S_{stomach}(t) + k_{1,10} \cdot S_{blood}(t) \\ &\quad - k_{10,8} \cdot S_{stomach}(t) \end{aligned} \quad (10)$$

$$\dot{S}_{brain}(t) = -k_{11,1} \cdot S_{brain}(t) + k_{1,11} \cdot S_{blood}(t) \quad (11)$$

$$\dot{S}_{muscle}(t) = -k_{12,1} \cdot S_{muscle}(t) + k_{1,12} \cdot S_{blood}(t) \quad (12)$$

$$\dot{S}_{bone}(t) = -k_{13,1} \cdot S_{bone}(t) + k_{1,13} \cdot S_{blood}(t) \quad (13)$$

$$\dot{S}_{skin}(t) = -k_{14,1} \cdot S_{skin}(t) + k_{1,14} \cdot S_{blood}(t) \quad (14)$$

Parameter Estimation

Parameter estimation and simulations were performed in MATLAB. Ex vivo data with 3 different time points were used to estimate a set of optimal kinetic parameters, denoted by K . First, the measurements were converted from concentrations to data that are comparable in a pharmacokinetic model. For that, the experimental data points were multiplied by the mean weight

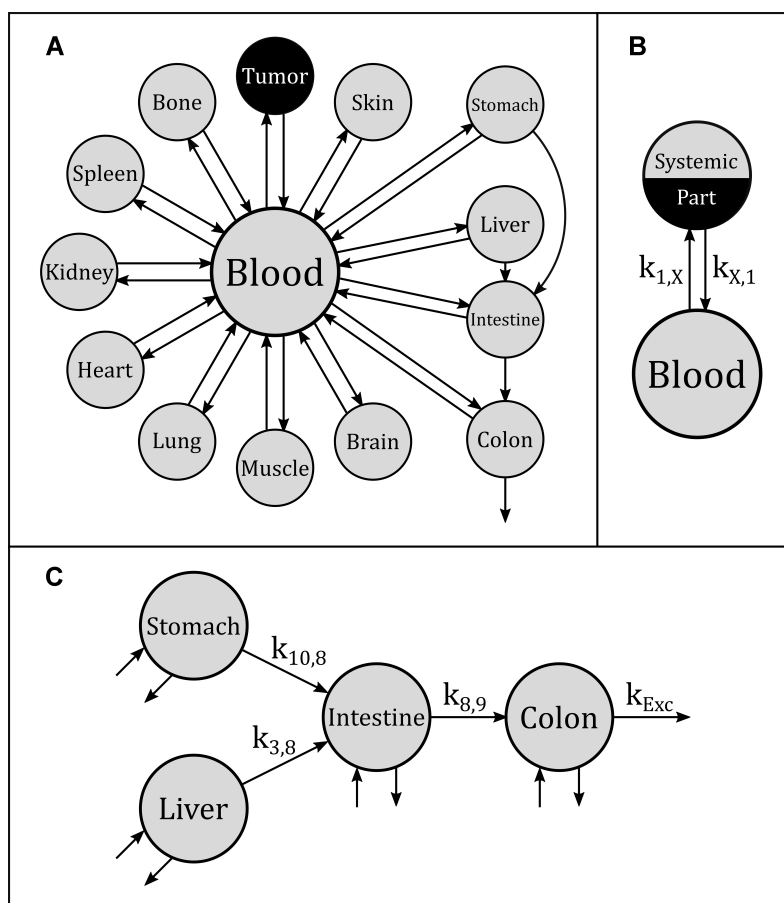


Figure 1 A mouse pharmacokinetic model for the kinetics of the biodistribution of SPIONs. **(A)** Overall model structure: Each bubble denotes one compartment and each arrow one pathway. The transition rate of each pathway $a \rightarrow b$ is described by one kinetic constant $k_{a,b}$. The intestine compartment represents the contents of the small intestine. **(B)** Systemic circulation: As blood is assumed to be the main transport mechanism between body parts, most pathways describe either the uptake rate constant from blood into a systemic part ($k_{1,X}$) or the emission rate constant from a systemic part into the blood ($k_{X,1}$). **(C)** Alimentary tract: Further transition parameters describe the pathways between organs that are part of the alimentary tract.

of the respective organs, which are described in literature.^{42,47–52} The parameters were estimated in two steps, both employing a least squares objective function with added constraints and weights. First, the two parameters for each body part were approximated successively, starting with $k_{1,2}$ and $k_{2,1}$, followed by $k_{1,3}$ and $k_{3,1}$, etc. This was done by minimizing an individual objective function for each parameter pair with highly increased weights for said parameters. This was followed in the second step by a global multistart fit around the best values found during the first step and $N = 1000$. The objective function in this step had an added constraint that increases the function even further,

if the observables are outside the confidence intervals of the experimental data points.

Results

In vivo Analysis of the Radiolabeled [⁸⁹Zr]-SPION Biodistribution

In order to quantify the retention of intratumorally administered SPIONs within GL261 glioblastoma, systemic biodistribution studies were performed, utilizing ⁸⁹Zr-labeled SPIONs. Nanoparticles were injected intratumorally in a volume of $0.34 \mu\text{L}/\text{mm}^3$. Treated mice were subsequently imaged using PET-CT at 1, 24, 48 and 72 h following

injection (n = 4). The image analysis of a single animal at all time points clearly demonstrated the localization of the signal within the tumor site or around the injection canal at all time points. Subsequent Prussian blue staining was performed to confirm the presence of iron oxide nanoparticles inside tumor cells (cf. [Supplementary Figure S1](#)).

Following injection of the SPIONs ex vivo organ counting was performed at 24, 48 and 72 h (n = 3 per group). The analysis proved that the majority of the injected nanoparticles were present either within the skin and adjunctive tissue of the tumor or within the glioblastoma. Additionally, uptake was observed in the liver, which is indicative for transport of the nanoparticles via blood circulation to this organ. Subsequent estimation of the ID across all time points demonstrated that nearly 50% of the ID accumulated with the glioblastoma (21–87%, n = 9). At the end of the follow-up period at 72 h 46% of the ID was retained in the tumor site (36–57%, n = 3). The precise comparison of the tumor to tissue ratio indicated an over 50-fold increase in nanoparticle retention in the tumor tissue compared to other tissues.

Pharmacokinetic Model

The mathematical model was established as a dynamical system (ie, changing over time) of distinct compartments, each containing a certain amount of ⁸⁹Zr-Perimag[®]-COOH SPIONs at each point in time (cf. [Figure 1](#)). This amount was measured using a gamma counter and normalized. The initial amount of injected SPIONs $S_{tumor}(0h)$ was indicated as 100% per g and the measured values accordingly as percentages per g. To have comparable numbers in regard to a pharmacokinetic model these values were each multiplied by the respective mean organ weight derived from literature.^{42,47-52}

Intratumorally Injected SPIONs

The developed pharmacokinetic model was used to estimate optimal kinetic parameters that best describe the measured data. The set of estimated parameters, denoted by K , can be found in [Table 1](#).

The kinetic parameters contained in K were used for simulations, starting from initial values $S(0h)$. As shown in [Figure 2](#), the simulations fit the measurements very well, except for body parts with very low values and too much background noise. Due to the intratumoral injection, all SPIONs are located inside the tumor at $t = 0$. According to both experimental data and simulations, a rapid release of SPIONs from the tumor occurs within

Table 1 Computed Kinetic Parameters (K). Each Value in the Upper Part Describes the Rate Constant of Either the Uptake of SPIONs into a Body Part from Blood or the Emission from a Body Part into Blood. The Values in the Lower Part Each Describe One Rate Constant of the Alimentary Tract. The Unit of Each Constant Is 1/h

Body Part	Uptake Rate ($k_{i,x}$)	Emission Rate ($k_{x,i}$)
Tumor	327.4	40.06
Liver	0.1159	$5.067 \cdot 10^{-4}$
Spleen	$9.780 \cdot 10^{-4}$	$1.409 \cdot 10^{-5}$
Kidney	3.804	15.66
Colon	0.7151	689.6
Stomach	7.411	896.0
Lung	1.903	148.5
Small Intestine	68.93	59.41
Muscle	194.2	62.39
Bone	62.60	38.58
Skin	9.380	27.58
Brain	5.439	795.6
Heart	2.416	490.5
Pathway	Notation	Rate
Liver → Sm. Intest.	$k_{3,8}$	$4.947 \cdot 10^{-4}$
Stomach → Sm. Intest.	$k_{10,8}$	64.71
Sm. Intest. → Colon	$k_{8,9}$	3.447
Colon → Excretion	k_{Exc}	$4.244 \cdot 10^{-3}$

the first 30 min after intratumoral injection. After 30 min the release of nanoparticles from the tumor steadily decreases. Nanoparticles released from the tumor also accumulate rapidly in other organs within the first 30 min. Then the uptake slows down during the following 100 h until an equilibrium is reached, with a certain amount of SPIONs retained in every compartment (cf. [Supplementary Figure S2](#)). In contrast, liver and spleen show a steady, low uptake of the nanoparticles over the whole period of time according to the model. Liver and spleen are therefore the major destiny of SPIONs. These results are confirmed by recent findings of other groups.⁵³⁻⁵⁵

Intravenously Injected SPIONs

To further validate the model two data sets from mice with intravenously injected SPIONs were analyzed.³⁹ The experimental data of both experiments could be described very well with the pharmacokinetic model (cf. [Figure 3](#)). The first set of data resulted from biodistribution studies with ^{99m}Tc-ferucarbotran injected into the tail vein of GL261 tumor bearing C57BL/6 mice. Although no data were available for the

International Journal of Nanomedicine downloaded from https://www.dovepress.com/ by 185.22.143.171 on 30-Jun-2020 For personal use only.

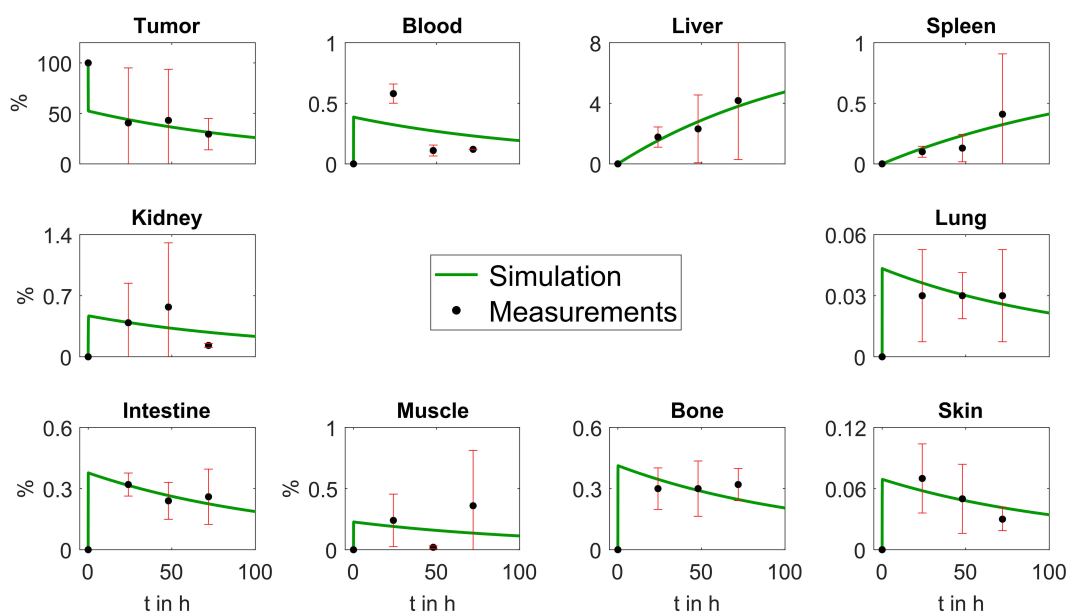


Figure 2 Plots depicting comparative analysis of ex vivo biodistribution data from intratumorally injected ^{89}Zr -Perimag[®]-COOH and simulation results calculated by our mathematical model. Each plot shows the results for one compartment. The black dots represent the mean values of the measured biodistribution data at a single time point and the red bars their standard deviation. The green curves depict the outcome of the simulations using the mathematical model and the set of estimated kinetic parameters K . All x-axes run from 0 to 100 h. The y-axes represent percentages of the released dose per gram of the initially injected amount of SPIONs. "Intestine" represents the contents of the small intestine. The respective plots for heart, colon, stomach and brain were below 0.005% at each time point (data not shown).

amount of SPIONs inside the skin, the previous uptake parameters from K for the skin could be used to make predictions. The parameters for the organs with available measurements were estimated anew by a parameter fit using the measurements (cf. [Supplementary Table S1](#)).

A similar analysis was performed on data from studies using ^{89}Zr -Perimag[®]-COOH nanoparticles (130 nm) that were injected into the tail vein of tumor-free C57BL/6 mice. Biodistribution data were acquired 80 min and 24 h after injection. As there was no data available for heart and skin, the already found parameters were again adopted from K to make predictions for the uptake inside these body parts (cf. [Supplementary Table S2](#)). The data for the other organs could be described very well with our pharmacokinetic model (cf. [Figure 4](#)).

Comparing the plots in [Figures 3](#) and [4](#) shows that the progression of the curves is very similar for most organs with the exception of spleen and bone. The data points for the spleen in [Figure 4](#) are very similar, which suggests a rapid increase within 80 min, when the amount inside the spleen has already reached its equilibrium. In [Figure 3](#), however, the model predicts a slower increase of nanoparticles inside the

spleen. The difference in the bone curves is due to the fact that the uptake of ^{89}Zr -Perimag[®]-COOH nanoparticles persists from 80 min to 24 h, whereas that of $^{99\text{m}}\text{Tc}$ -ferucarboxan nanoparticles further increases after 24 h.

There are also notable differences between the curve progressions of the plots from intratumoral injection data and intravenous injection data. These can be explained by the huge and rapid decrease in blood after i.v. injection compared to the relatively slow decrease inside the tumor tissue after intratumoral injection. While for the latter the increase in most other organs is also very fast in the beginning, the increase stops, when a more stable state is reached. Thereafter, a slow transport of SPIONs into liver and spleen from all other organs occurs. After i.v. injection, however, the SPIONs are rapidly emitted into all organs, causing a short peak inside most of them, before most nanoparticles are immediately transported into organs with higher retention capacity. Also notable is that after i.v. injection the liver directly absorbs a large amount of SPIONs, whereas the increase is much slower, yet more steady and lasting after intratumoral injection.

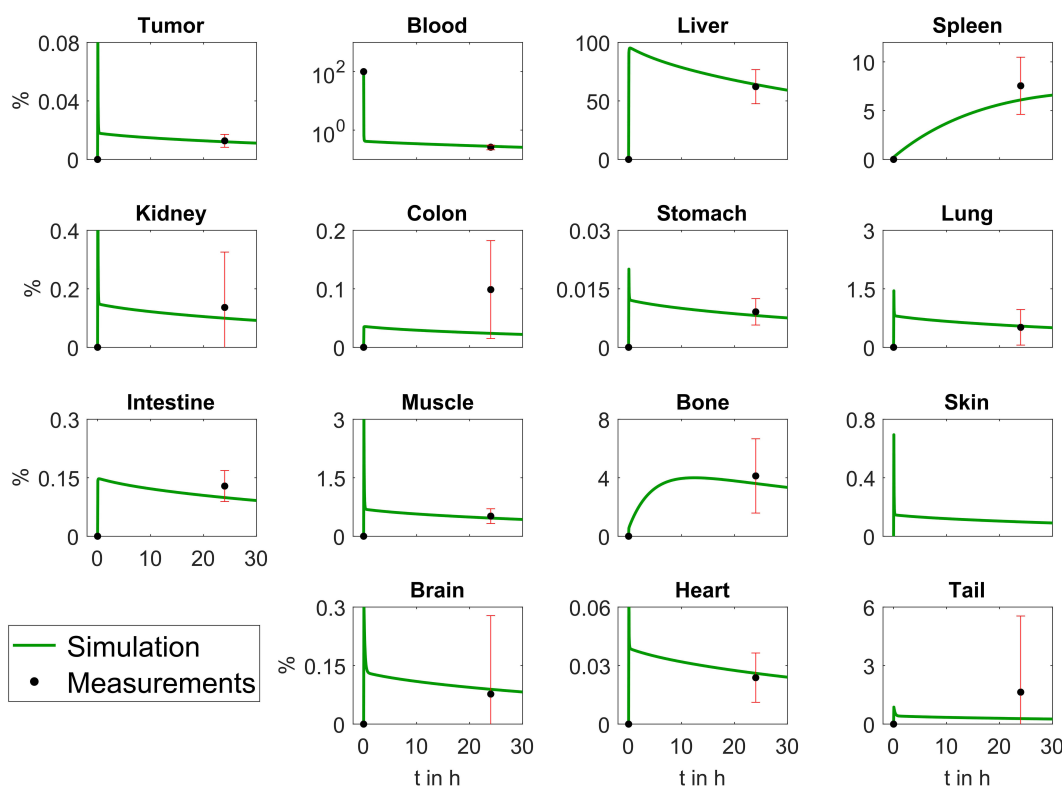


Figure 3 Plots depicting comparative analysis of ex vivo biodistribution data from i.v. injected ^{99m}Tc-ferucarbotran and simulation results. The black dots represent the mean values of the measured biodistribution data at *t* = 24 h and the red lines their respective error bars. The green curves depict the outcome of the simulations using the mathematical model. All x-axes run from 0 to 30 h.

Discussion

Applications of nanotechnology have enabled the development of anti-cancer diagnostic and therapeutic agents that provided promising results for translational and clinical oncology.^{56–58} One possible route for the administration of nanoparticles is the intratumoral injection, which can provide (i) a high local concentration of the agent, (ii) reduction of the particle clearance (ie, renal or hepatic clearance) that increases the bioavailability of nanoparticles, (iii) decrease in the off-target side effects, and (iv) avoidance of the natural histo-hematic barriers (eg, brain-blood barrier). In the current study, we analyzed the biodistribution of intratumorally injected SPIONs into brain tumors for which we developed a new mathematical model for prediction of particle clearance from the injection site. We observed a predominant retention (46% of the ID) of the radiolabeled ⁸⁹Zr-Perimag[®]-COOH in the GL261 glioblastoma over a period of 72 h. To show a potential localization of

nanoparticles in tumor-associated macrophages the glioma sections were stained for CD11b, which is a marker for TAMs. Only very few CD11b+ TAMs were found with intracellular localized nanoparticles in a field of view (×20) inside the tumor (data not shown). These data indicate that most nanoparticles are taken up by tumor cells and not by CD11b+ TAMs. Intriguingly, some uptake of the SPIONs was observed within the liver and spleen tissues at 48 and 72 h post-injection. Presumably, these nanoparticles reached these tissues via the blood circulation. The main limitation of the implemented non-orthotopic tumor mouse model is the elimination of the brain-blood barrier (BBB) that could hamper the delivery of theranostic agents to the glioma site in the brain. However, the applied dose of the intratumorally administered nanoparticles (ie, 0.34 μg/mm³) was too high for an orthotopic glioblastoma model. The large volume would result in intracranial hypertension with subsequent brain dislocation. To avoid these

International Journal of Nanomedicine downloaded from https://www.dovepress.com/ by 185.22.143.171 on 30-Jun-2020 For personal use only.

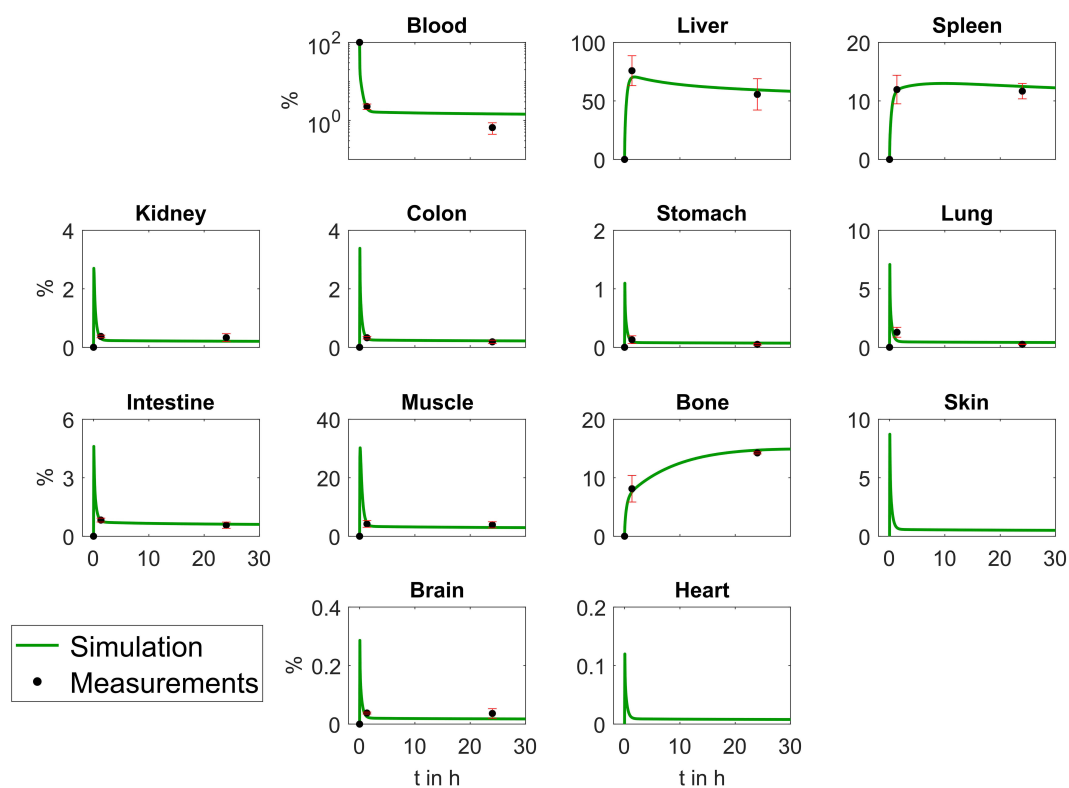


Figure 4 Plots depicting comparative analysis of ex vivo biodistribution data from i.v. injected ^{89}Zr -Perimag[®]-COOH and simulation results. The black dots represent the mean values of the measured biodistribution data at $t = 24$ h and the red lines their respective standard deviation. The green curves depict the outcome of the simulations using the mathematical model. All x-axes run from 0 to 30 h.

complications our modeling experiments were performed in GL261 tumors which were implanted into the flank of the mice.

The obtained data of the pharmacokinetics of the labeled nanoparticles are in line with previously published in vivo data on the biodistribution of locally injected nanoparticles of various formulations.^{59–61} Xie et al reported the biodistribution of intratumorally infused copper-64 (^{64}Cu) nanoshells labelled with radionuclide in the head and neck squamous cell carcinoma xenograft in nude mice.⁶¹ Employing positron emission tomography/computer tomography (PET/CT) imaging the authors demonstrated higher retention of ^{64}Cu nanoshells for a period of 44 h post-injection inside the tumor with low concentrations in healthy tissues.⁶¹ In another study by Chi et al intratumorally injected ^{131}I gelatin microspheres (^{131}I -GMSs) remained in human hepatocellular carcinoma (HepG2) of nude Balb/c mice for a period of 32 days and resulted in a suppressed tumor growth and an increased

overall survival.⁵⁹ To increase the accuracy of the magnetic nanoparticle imaging novel, highly sensitive technologies, particularly magnetic particles imaging (MPI), are necessary for the detection of nanoparticles at very low concentrations (2 pg per cell).^{4–6}

In line with the in vivo biodistribution studies, the developed mathematical model allowed us to predict the behavior of SPIONs after intratumoral and intravenous injection (cf. Figure 2). However, certain limitations should be kept in mind, when employing this model. Weights of all body parts were assumed to be equal for all mice. Particularly the tumor weight may differ vastly between different groups of animals and information about the tumor size is an important part of adjustments of parameters in the model. A suggestion for further studies would therefore be to estimate the parameters separately for each test subject and perform a statistical analysis on the comparability of the resulting parameters. Differences

between measurement points in compartments with unsatisfactory fits can be explained by substantial noise or other uncertainties. Adding multiple parameters to the affected parameters to increase the quality of the fits may result in overfitting and incorrect conclusions. The parameters were estimated by comparing simulated observables with the means of the experimental data points, while employing an additional penalty constraint for observables outside the confidence intervals of the data. The initial values for each fit were chosen randomly around previously found values. Multistart sampling like this has been proven to be very effective for modeling complex biological systems.⁶² More advanced models that take specific biomechanical features of the compartments into account are planned, when more experimental data are available.

Long-term local deposition and low clearance of nanoparticles could be employed for the prolonged local anti-tumor therapies that could include hyperthermia treatment, chemo/radiotherapy or a combination of these therapeutic modalities. Indeed, several studies reported on improved tumor outcome after locally delivered nanoparticle-based agents.^{60,63-67} Thus, in the recent study by Li et al intratumorally injected MnS@Bi₂S₃-PEG nanoparticles in combination with hyperthermia treatment significantly boosted the efficacy of radiotherapy, indicating the synergistic anti-tumor effect.⁶⁴

The properties that are known to affect the biodistribution and clearance of nanoparticles include the size, chemical composition, surface charge and chemistry and shape.⁶⁸ The main limitation of the current study is that for our mathematical modeling SPIONs with a diameter of ≈ 130 nm were used. Though the developed pharmacokinetic model could describe the behavior of nanoparticles of this size, the computed parameters are very likely to differ for other sizes of nanoparticles or mouse models. To test the impact of the size of the nanoparticles on the mathematical model ^{99m}Tc-ferucarbotran-labeled nanoparticles with a diameter of approximately 60 nm were used for i.v. administration. As expected, the analysis of these data sets showed that even though the mathematical model is applicable also for intravenous injection, the parameters differed strongly for ^{99m}Tc-ferucarbotran nanoparticles with a size of 60 nm after i.v. injection into C57BL/6 mice. Due to the smaller size, these nanoparticles are taken up and metabolized through different pathways compared to larger nanoparticles. To investigate if these changes are due to differences in SPION characteristics

or mouse models, further studies are necessary. Although the assumptions allow the application of the model for other iron oxide nanoparticles, the process of parameter estimation should be repeated in studies involving nanoparticles with different biochemical and biophysical properties.

The analysis of the data from intravenously administered SPIONs showed that at least without targeting the number of particles reaching the tumor is surely below the desired amount. The model predicts that immediately after injection the dose inside the tumor peaks at around 0.07% of the initially injected dose. After that most of the nanoparticles are transported to liver and spleen. In comparison, after intratumoral injection around 80% of the initial dose stays inside the tumor for more than two days. To raise the peak after i.v. injection to the same scale, the overall injected dose would have to be increased by at least a three-digit factor. Such a concentration would be toxic for other organs like liver and spleen, which would suffer from an increased uptake by the same factor, and is therefore not possible. To overcome this problem one could employ functionalized targeting nanoparticles with an improved accumulation inside the tumor. Previously, several studies reported the enhanced accumulation of functionalized tumor-targeted nanoparticles as compared to non-coated particles.^{16,69,70} The effect of tumor targeting on biodistribution both biologically and mathematically will hence be the next important step in further studies, since ways to make intravenous injections viable may be a crucial part of making nanoparticle-based agents viable for clinical application.

In conclusion, the developed pharmacokinetic model is applicable for biodistribution studies on iron oxide nanoparticles. As Henrique Silva et al already indicated, pharmacokinetic models provide a valuable tool in understanding the biodistribution of SPIONs.⁵³ In this case, the common structure of PBPK models was reduced to only predominant pathways to predict meaningful results for the available experimental data sets. This enables applications of the model to in vivo studies on SPIONs for further experimental investigations, where collecting large amounts of time dependent data is usually difficult. Yet it is important to regard the potentially large effects of changes in nanoparticle properties on biological behavior, which are likely to result in specific kinetic transfer parameters for each type of nanoparticle. Further experimental investigations of SPIONs in mice and humans can provide additional pharmacokinetic data and

may provide insights into biochemical and physiological processes of nanoparticles in organs and tumors, possibly even on a cellular level. This can further improve the model structure and the transfer coefficients. The pharmacokinetic model developed in this study can be further modified by employing available experimental data and adapted to describe the kinetic processes of other therapeutic nanoparticles, such as gold nanoparticles in in vivo xenograft model.

Acknowledgments

The study was supported by the Russian Foundation for Basic Research (RFBR) according to the research project № 20-38-70039 and DFG grant (SFB824/3, STA1520/1-1), Technische Universität München (TUM) within the DFG funding program Open Access Publishing. Additional financial support was provided by TaGoNaX DFG project № 336532926.

Disclosure

The authors declare no conflict of interest. The funders had no role in the design of the study; in the collection, analyses, or interpretation of data; in the writing of the manuscript, or in the decision to publish the results.

References

- Jahangirian H, Kalantari K, Izadiyan Z, Rafiee-Moghaddam R, Shameli K, Webster TJ. A review of small molecules and drug delivery applications using gold and iron nanoparticles. *Int J Nanomedicine*. 2019;14:1633–1657. doi:10.2147/IJN.S184723
- Shevtsov M, Multhoff G. Recent developments of magnetic nanoparticles for theranostics of brain tumor. *Curr Drug Metab*. 2016;17(8):737–744. doi:10.2174/1389200217666160607232540
- Shevtsov M, Stangl S, Nikolaev B, et al. Granzyme B functionalized nanoparticles targeting membrane Hsp70-positive tumors for multimodal cancer theranostics. *Small*. 2019;15(13):e1900205. doi:10.1002/smll.201900205
- Abed Z, Beik J, Laurent S, et al. Iron oxide-gold core-shell nanotheranostic for magnetically targeted photothermal therapy under magnetic resonance imaging guidance. *J Cancer Res Clin Oncol*. 2019;145(5):1213–1219. doi:10.1007/s00432-019-02870-x
- Asadi M, Beik J, Hashemian R, et al. MRI-based numerical modeling strategy for simulation and treatment planning of nanoparticle-assisted photothermal therapy. *Phys Med*. 2019;66:124–132. doi:10.1016/j.ejmp.2019.10.002
- Beik J, Asadi M, Khoei S, et al. Simulation-guided photothermal therapy using MRI-traceable iron oxide-gold nanoparticle. *J Photochem Photobiol B*. 2019;199:111599. doi:10.1016/j.jphotobiol.2019.111599
- Janko C, Ratschker T, Nguyen K, et al. Functionalized superparamagnetic iron oxide nanoparticles (SPIONs) as platform for the targeted multimodal tumor therapy. *Front Oncol*. 2019;9:59. doi:10.3389/fonc.2019.00059
- Deatsch AE, Evans BA. Heating efficiency in magnetic nanoparticle hyperthermia. *J Magn Magn Mater*. 2014;354:163–172. doi:10.1016/j.jmmm.2013.11.006
- Chao Y, Chen G, Liang C, et al. Iron nanoparticles for low-power local magnetic hyperthermia in combination with immune checkpoint blockade for systemic antitumor therapy. *Nano Lett*. 2019;19(7):4287–4296. doi:10.1021/acs.nanolett.9b00579
- Jordan A, Scholz R, Maier-Hauff K, et al. The effect of thermotherapy using magnetic nanoparticles on rat malignant glioma. *J Neurooncol*. 2006;78(1):7–14. doi:10.1007/s11060-005-9059-z
- Popescu RC, Andronescu E, Grumezescu AM. In vivo evaluation of Fe(3)O(4) nanoparticles. *Rom J Morphol Embryol*. 2014;55(3 Suppl):1013–1018.
- Wang R, Chen C, Yang W, Shi S, Wang C, Chen J. Enhancement effect of cytotoxicity response of silver nanoparticles combined with thermotherapy on C6 rat glioma cells. *J Nanosci Nanotechnol*. 2013;13(6):3851–3854. doi:10.1166/jnn.2013.7156
- Yi GQ, Gu B, Chen LK. The safety and efficacy of magnetic nanoparticle hyperthermia therapy on rat brain glioma. *Tumour Biol*. 2014;35(3):2445–2449. doi:10.1007/s13277-013-1324-8
- Mukherjee S, Liang L, Veisoh O. Recent advancements of magnetic nanomaterials in cancer therapy. *Pharmaceutics*. 2020;12(2):147. doi:10.3390/pharmaceutics12020147
- Choi KY, Liu G, Lee S, Chen X. Theranostic nanoplateforms for simultaneous cancer imaging and therapy: current approaches and future perspectives. *Nanoscale*. 2012;4(2):330–342. doi:10.1039/C1NR11277E
- Hadjipanayis CG, Machaidze R, Kaluzova M, et al. EGFRvIII antibody-conjugated iron oxide nanoparticles for magnetic resonance imaging-guided convection-enhanced delivery and targeted therapy of glioblastoma. *Cancer Res*. 2010;70(15):6303–6312. doi:10.1158/0008-5472.CAN-10-1022
- Schleich N, Sibret P, Danhier P, et al. Dual anticancer drug/superparamagnetic iron oxide-loaded PLGA-based nanoparticles for cancer therapy and magnetic resonance imaging. *Int J Pharm*. 2013;447(1–2):94–101. doi:10.1016/j.ijpharm.2013.02.042
- Zhu L, Zhou Z, Mao H, Yang L. Magnetic nanoparticles for precision oncology: theranostic magnetic iron oxide nanoparticles for image-guided and targeted cancer therapy. *Nanomedicine (Lond)*. 2017;12(1):73–87. doi:10.2217/nmm-2016-0316
- Xing R, Bhirde AA, Wang S, et al. Hollow iron oxide nanoparticles as multidrug resistant drug delivery and imaging vehicles. *Nano Res*. 2012;6(1):1–9. doi:10.1007/s12274-012-0275-5
- Zhou Z, Sun Y, Shen J, et al. Iron/iron oxide core/shell nanoparticles for magnetic targeting MRI and near-infrared photothermal therapy. *Biomaterials*. 2014;35(26):7470–7478. doi:10.1016/j.biomaterials.2014.04.063
- Giustini AJ, Ivkov R, Hoopes PJ. Magnetic nanoparticle biodistribution following intratumoral administration. *Nanotechnology*. 2011;22(34):345101. doi:10.1088/0957-4484/22/34/345101
- Gultepe E, Reynoso FJ, Jhaveri A, et al. Monitoring of magnetic targeting to tumor vasculature through MRI and biodistribution. *Nanomedicine (Lond)*. 2010;5(8):1173–1182. doi:10.2217/nmm.10.84
- Natarajan A, Gruettner C, Ivkov R, et al. NanoFerrite particle based radioimmunonanoparticles: binding affinity and in vivo pharmacokinetics. *Bioconjug Chem*. 2008;19(6):1211–1218. doi:10.1021/bc800015n
- Shevtsov MA, Nikolaev BP, Ryzhov VA, et al. Brain tumor magnetic targeting and biodistribution of superparamagnetic iron oxide nanoparticles linked with 70-kDa heat shock protein study by nonlinear longitudinal response. *J Magn Magn Mater*. 2015;388:123–134. doi:10.1016/j.jmmm.2015.04.030
- Jacquez JA. Compartmental analysis in biology and medicine. *BioMedware*. 1996.
- Li M, Zou P, Tyner K, Lee S. Physiologically based pharmacokinetic (PBPK) modeling of pharmaceutical nanoparticles. *AAPS J*. 2017;19(1):26–42. doi:10.1208/s12248-016-0010-3
- Hagens WL, Oomen AG, de Jong WH, Cassee FR, Sips AJ. What do we (need to) know about the kinetic properties of nanoparticles in the body? *Regul Toxicol Pharmacol*. 2007;49(3):217–229. doi:10.1016/j.yrtph.2007.07.006

28. Li M, Al-Jamal KT, Kostarelos K, Reineke J. Physiologically based pharmacokinetic modeling of nanoparticles. *ACS Nano*. 2010;4(11):6303–6317. doi:10.1021/nn1018818
29. Sager JE, Yu J, Ragueneau-Majlessi I, Isoherranen N. Physiologically based pharmacokinetic (PBPK) modeling and simulation approaches: a systematic review of published models, applications, and model verification. *Drug Metab Dispos*. 2015;43(11):1823–1837. doi:10.1124/dmd.115.065920
30. Yellepeddi V, Rower J, Liu X, Kumar S, Rashid J, Sherwin CMT. State-of-the-art review on physiologically based pharmacokinetic modeling in pediatric drug development. *Clin Pharmacokinet*. 2019;58(1):1–13. doi:10.1007/s40262-018-0677-y
31. Yoshida K, Budha N, Jin JY. Impact of physiologically based pharmacokinetic models on regulatory reviews and product labels: frequent utilization in the field of oncology. *Clin Pharmacol Ther*. 2017;101(5):597–602. doi:10.1002/cpt.622
32. Yuan D, He H, Wu Y, Fan J, Cao Y. Physiologically based pharmacokinetic modeling of nanoparticles. *J Pharm Sci*. 2019;108(1):58–72. doi:10.1016/j.xphs.2018.10.037
33. Carlander U, Li D, Jolliet O, Emond C, Johanson G. Toward a general physiologically-based pharmacokinetic model for intravenously injected nanoparticles. *Int J Nanomedicine*. 2016;11:625–640. doi:10.2147/IJN.S94370
34. Li D, Morishita M, Wagner JG, et al. In vivo biodistribution and physiologically based pharmacokinetic modeling of inhaled fresh and aged cerium oxide nanoparticles in rats. *Part Fibre Toxicol*. 2016;13(1):45. doi:10.1186/s12989-016-0156-2
35. Li M, Panagi Z, Avgoustakis K, Reineke J. Physiologically based pharmacokinetic modeling of PLGA nanoparticles with varied mPEG content. *Int J Nanomedicine*. 2012;7:1345–1356. doi:10.2147/IJN.S23758
36. Sweeney LM, MacCalman L, Haber LT, Kuempel ED, Tran CL. Bayesian evaluation of a physiologically-based pharmacokinetic (PBPK) model of long-term kinetics of metal nanoparticles in rats. *Regul Toxicol Pharmacol*. 2015;73(1):151–163. doi:10.1016/j.yrtph.2015.06.019
37. Péry ARR, Brochot C, Hoet PHM, Nemmar A, Bois FY. Development of a physiologically based kinetic model for 99mTc-technetium-labelled carbon nanoparticles inhaled by humans. *Inhal Toxicol*. 2009;21(13):1099–1107. doi:10.3109/08958370902748542
38. Kousba A, Sultatos LG. Continuous system modeling of equilibrium dialysis for determinations of tissue partitioning of parathion and paraoxon. *Toxicol Lett*. 2002;133(2):153–159. doi:10.1016/S0378-4274(02)00131-5
39. Abdollah MRA, Carter TJ, Jones C, et al. Fucoidan prolongs the circulation time of dextran-coated iron oxide nanoparticles. *ACS Nano*. 2018;12(2):1156–1169. doi:10.1021/acsnano.7b06734
40. Li WB, Höllriegel V, Roth P, Oeh U. Influence of human biokinetics of strontium on internal ingestion dose of 90Sr and absorbed dose of 89Sr to organs and metastases. *Radiat Environ Biophys*. 2008;47(2):225–239. doi:10.1007/s00411-007-0154-8
41. Human alimentary tract model for radiological protection. ICRP Publication 100. *Ann ICRP*. 2006;36(1–2):25–30. doi:10.1016/j.icrp.2006.03.004
42. Baxter LT, Zhu H, Mackensen DG, Jain RK. Physiologically based pharmacokinetic model for specific and nonspecific monoclonal antibodies and fragments in normal tissues and human tumor xenografts in nude mice. *Cancer Res*. 1994;54(6):1517–1528.
43. Garg A, Balthasar JP. Physiologically-based pharmacokinetic (PBPK) model to predict IgG tissue kinetics in wild-type and FeRn-knockout mice. *J Pharmacokinet Pharmacodyn*. 2007;34(5):687–709. doi:10.1007/s10928-007-9065-1
44. Polli JR, Engler FA, Balthasar JP. Physiologically based modeling of the pharmacokinetics of “catch-and-release” anti-carcinoembryonic antigen monoclonal antibodies in colorectal cancer xenograft mouse models. *J Pharm Sci*. 2019;108(1):674–691. doi:10.1016/j.xphs.2018.09.037
45. Guyton AC, Hall JE. *Textbook of Medical Physiology*. Philadelphia, PA: Elsevier Sanders; 2006.
46. Paquet F, Bailey MR, Leggett RW; on Radiological Protection IC. Occupational intakes of radionuclides: part 2. ICRP publication 134. *Ann ICRP*. 2016;45(3–4):7–349. doi:10.1177/0146645316670045
47. Bigham ML, Cockrem F. Body weights, tail lengths, body temperatures, food intakes, & some slaughter data for four strains of mice reared at three different environmental temperatures. *New Zeal J Agri Res*. 2012;12(4):658–668. doi:10.1080/00288233.1969.10421217
48. Konarzewski M, Diamond J. Evolution of basal metabolic rate and organ masses in laboratory mice. *Evolution*. 1995;49(6):1239–1248. doi:10.1111/j.1558-5646.1995.tb04450.x
49. Kumral A, Tugyan K, Gonenc S, et al. Protective effects of erythropoietin against ethanol-induced apoptotic neurodegeneration and oxidative stress in the developing C57BL/6 mouse brain. *Brain Res Dev Brain Res*. 2005;160(2):146–156. doi:10.1016/j.devbrainres.2005.08.006
50. Riches AC, Sharp JG, Thomas DB, Smith SV. Blood volume determination in the mouse. *J Physiol*. 1973;228(2):279–284. doi:10.1113/jphysiol.1973.sp010086
51. Wang Q, Sun P, Li G, Zhu K, Wang C, Zhao X. Inhibitory effects of *Dendrobium candidum* Wall ex Lindl. on azoxymethane- and dextran sulfate sodium-induced colon carcinogenesis in C57BL/6 mice. *Oncol Lett*. 2014;7(2):493–498. doi:10.3892/ol.2013.1728
52. Xiao F, Furuta T, Takashima M, Shirai N, Hanai H. Involvement of cyclooxygenase-2 in hyperplastic gastritis induced by *Helicobacter pylori* infection in C57BL/6 mice. *Aliment Pharmacol Ther*. 2001;15(6):875–886. doi:10.1046/j.1365-2036.2001.00965.x
53. Henrique Silva A, Lima Jr E, Vasquez Mansilla M, et al. A physiologically based pharmacokinetic model to predict the superparamagnetic iron oxide nanoparticles (SPIONs) accumulation in vivo. *Eur J Nanomed*. 2017;9(2):79. doi:10.1515/ejnm-2017-0001
54. Pham BTT, Colvin EK, Pham NTH, et al. Biodistribution and clearance of stable superparamagnetic maghemite iron oxide nanoparticles in mice following intraperitoneal administration. *Int J Mol Sci*. 2018;19(1):205. doi:10.3390/ijms19010205
55. Yu Q, Xiong XQ, Zhao L, et al. Biodistribution and toxicity assessment of superparamagnetic iron oxide nanoparticles in vitro and in vivo. *Curr Med Sci*. 2018;38(6):1096–1102. doi:10.1007/s11596-018-1989-8
56. Han X, Xu K, Taratula O, Farsad K. Applications of nanoparticles in biomedical imaging. *Nanoscale*. 2019;11(3):799–819. doi:10.1039/C8NR07769J
57. Shevtsov MA, Multhoff G. *Targeted and Theranostic Applications for Nanotechnologies in Medicine: Nanoparticles for Brain Tumor Targeting*. Elsevier; 2017; 487–511.
58. Vangijzegeem T, Stanicki D, Laurent S. Magnetic iron oxide nanoparticles for drug delivery: applications and characteristics. *Expert Opin Drug Deliv*. 2019;16(1):69–78. doi:10.1080/17425247.2019.1554647
59. Chi JL, Li CC, Xia CQ, et al. Effect of 131I gelatin microspheres on hepatocellular carcinoma in nude mice and its distribution after intratumoral injection. *Radiat Res*. 2014;181(4):416–424, 419. doi:10.1667/RR13539.1
60. Liu H, Xu H, Wang Y, He Z, Li S. Effect of intratumoral injection on the biodistribution and therapeutic potential of novel chemophor EL-modified single-walled nanotube loading doxorubicin. *Drug Dev Ind Pharm*. 2012;38(9):1031–1038. doi:10.3109/03639045.2011.637050
61. Xie H, Goins B, Bao A, Wang ZJ, Phillips WT. Effect of intratumoral administration on biodistribution of 64Cu-labeled nanoshells. *Int J Nanomedicine*. 2012;7:2227–2238. doi:10.2147/IJN.S30699
62. Raue A, Schilling M, Bachmann J, et al. Lessons learned from quantitative dynamical modeling in systems biology. *PLoS One*. 2013;8(9):e74335. doi:10.1371/journal.pone.0074335
63. Gogoi M, Jaiswal MK, Sarma HD, Bahadur D, Banerjee R. Biocompatibility and therapeutic evaluation of magnetic liposomes designed for self-controlled cancer hyperthermia and chemotherapy. *Integr Biol (Camb)*. 2017;9(6):555–565. doi:10.1039/C6IB00234J

64. Li Y, Sun Y, Cao T, et al. A cation-exchange controlled core-shell MnS@Bi₂S₃ theranostic platform for multimodal imaging guided radiation therapy with hyperthermia boost. *Nanoscale*. 2017;9(38):14364–14375. doi:10.1039/C7NR02384G
65. Liu Q, Li R, Zhu Z, et al. Enhanced antitumor efficacy, biodistribution and penetration of docetaxel-loaded biodegradable nanoparticles. *Int J Pharm*. 2012;430(1–2):350–358. doi:10.1016/j.ijpharm.2012.04.008
66. Nguyen HT, Tran TH, Thapa RK, et al. Incorporation of chemotherapeutic agent and photosensitizer in a low temperature-sensitive liposome for effective chemo-hyperthermic anticancer activity. *Expert Opin Drug Deliv*. 2017;14(2):155–164. doi:10.1080/17425247.2017.1266330
67. Wang Y, Xu H, Liu H, Wang Y, Sun J, He Z. Efficacy and biodistribution of tocopheryl polyethylene glycol succinate noncovalent functionalized single walled nanotubes loading doxorubicin in sarcoma bearing mouse model. *J Biomed Nanotechnol*. 2012;8(3):450–457. doi:10.1166/jbn.2012.1390
68. Ernsting MJ, Murakami M, Roy A, Li SD. Factors controlling the pharmacokinetics, biodistribution and intratumoral penetration of nanoparticles. *J Control Release*. 2013;172(3):782–794. doi:10.1016/j.jconrel.2013.09.013
69. Dong Q, Yang H, Wan C, et al. Her2-functionalized gold-nanosheilded magnetic hybrid nanoparticles: a theranostic agent for dual-modal imaging and photothermal therapy of breast cancer. *Nanoscale Res Lett*. 2019;14(1):235. doi:10.1186/s11671-019-3053-4
70. Shevtsov MA, Nikolaev BP, Ryzhov VA, et al. Ionizing radiation improves glioma-specific targeting of superparamagnetic iron oxide nanoparticles conjugated with cmHsp70.1 monoclonal antibodies (SPION-cmHsp70.1). *Nanoscale*. 2015;7(48):20652–20664. doi:10.1039/C5NR06521F

International Journal of Nanomedicine

Dovepress

Publish your work in this journal

The International Journal of Nanomedicine is an international, peer-reviewed journal focusing on the application of nanotechnology in diagnostics, therapeutics, and drug delivery systems throughout the biomedical field. This journal is indexed on PubMed Central, MedLine, CAS, SciSearch®, Current Contents®/Clinical Medicine,

Journal Citation Reports/Science Edition, EMBase, Scopus and the Elsevier Bibliographic databases. The manuscript management system is completely online and includes a very quick and fair peer-review system, which is all easy to use. Visit <http://www.dovepress.com/testimonials.php> to read real quotes from published authors.

Submit your manuscript here: <https://www.dovepress.com/international-journal-of-nanomedicine-journal>

A.1.2. Supplementary information

A new pharmacokinetic model describing the biodistribution of intravenously and intratumorally administered superparamagnetic iron oxide nanoparticles (SPIONs) in a GL261 xenograft glioblastoma model

Alexander P. Klapproth ^{1,2,†}
Maxim Shevtsov ^{1,3-7,†,*}
Stefan Stangl ¹
Wei Bo Li ^{2,*}
Gabriele Multhoff ¹

¹Center for Translational Cancer Research Technische Universität München (TranslaTUM), Klinikum rechts der Isar, Munich, Germany; ²Institute of Radiation Medicine, Helmholtz Zentrum München, German Research Center for Environmental Health (GmbH), Munich, Germany; ³Institute of Cytology of the Russian Academy of Sciences (RAS), St. Petersburg, Russia; ⁴First Pavlov State Medical University of St.Petersburg, St. Petersburg, Russia; ⁵Almazov National Medical Research Centre, Russian Polenov Neurosurgical Institute, St. Petersburg, Russia; ⁶National Center for Neurosurgery, Nur-Sultan, Kazakhstan; ⁷Far Eastern Federal University, Vladivostok, Russia

† These authors contributed equally to this work.

Correspondence: Maxim Shevtsov, Wei Bo Li
Email: maxim.shevtsov@tum.de; wli@helmholtz-muenchen.de

Supplementary Files

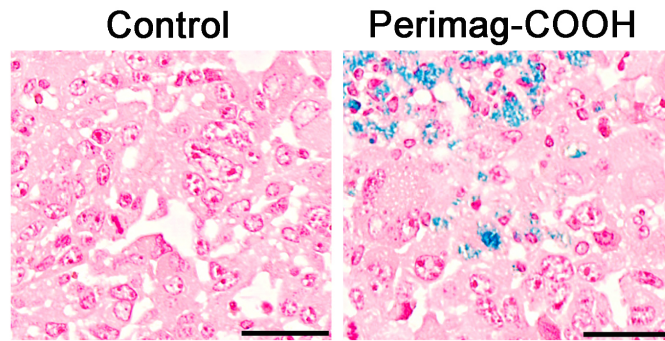


Figure S1: Prussian blue staining of the mouse GL261 glioblastoma 24 hours following intratumoral injection of nanoparticles. Scale bar: 25 μm .

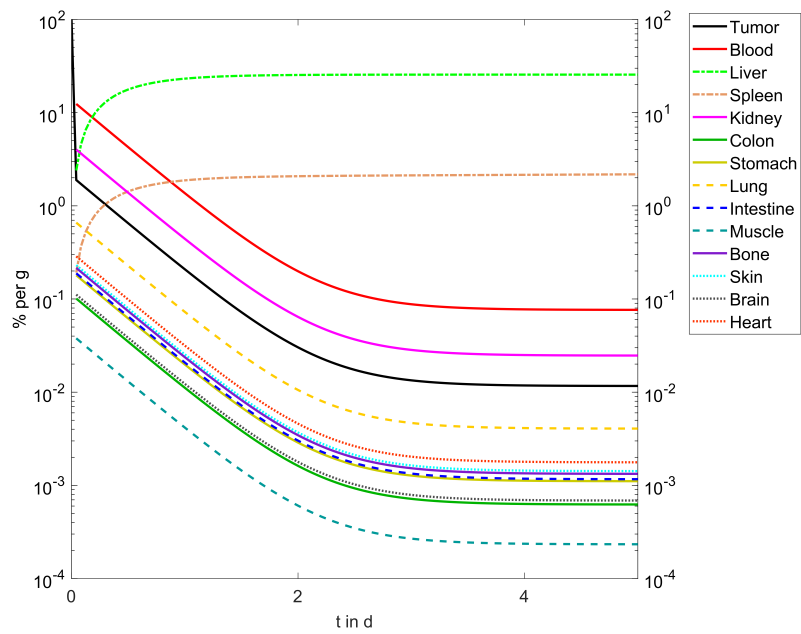


Figure S2: Simulated pharmacokinetics of ^{89}Zr -Perimag@-COOH SPIONs after intratumoral injection in a long running simulation.

Table S1: Computed kinetic parameters for i.v. injected ^{99m}Tc -ferucarbotran (cf. Figure 3). The unit of each constant is 1/h.

Body Part	Uptake Rate ($k_{1,X}$)	Emission Rate ($k_{X,1}$)
Tumor	0.7620	18.06
Liver	571.7	1.462
Spleen	1.646	$7.227 \cdot 10^{-2}$
Kidney	16.32	221.7
Colon	0.8175	$3.151 \cdot 10^3$
Stomach	12.70	287.7
Lung	609.8	209.0
Small Intestine	0.1167	11.20
Muscle	23.72	18.06
Bone	3.409	0.3710
Brain	1.437	9.102
Heart	9.866	192.5
Tail	3.503	4.283

Pathway	Notation	Rate
Liver \rightarrow Sm. Intest.	$k_{3,8}$	1.722
Stomach \rightarrow Sm. Intest.	$k_{10,8}$	82.52
Sm. Intest. \rightarrow Colon	$k_{8,9}$	748.6
Colon \rightarrow Excretion	k_{Exc}	36.12

Table S2: Computed kinetic parameters for i.v. injected ^{89}Zr -Perimag®-COOH (cf. Figure 4). The unit of each constant is 1/h.

Body Part	Uptake Rate ($k_{1,X}$)	Emission Rate ($k_{X,1}$)
Liver	10.43	0.1244
Spleen	1.555	0.1833
Kidney	2.554	15.74
Colon	37.17	294.2
Stomach	17.74	206.3
Lung	34.97	96.40
Small Intestine	$4.089 \cdot 10^{-2}$	24.24
Muscle	20.20	9.050
Bone	0.9360	$9.164 \cdot 10^{-2}$
Brain	2.435	166.5

Pathway	Notation	Rate
Liver \rightarrow Sm. Intest.	$k_{3,8}$	0.1347
Stomach \rightarrow Sm. Intest.	$k_{10,8}$	115.5
Sm. Intest. \rightarrow Colon	$k_{8,9}$	6.403
Colon \rightarrow Excretion	k_{Exc}	1.029

**A.2. Erratum: A new pharmacokinetic model describing the
biodistribution of i.v. and intratumorally administered
superparamagnetic iron oxide nanoparticles (SPIONs)
in a GL261 xenograft glioblastoma model
[corrigendum]**

Authors: A.P. Klapproth, M. Shevtsov, S. Stangl, W.B. Li, G. Multhoff



CORRIGENDUM

A New Pharmacokinetic Model Describing the Biodistribution of Intravenously and Intratumorally Administered Superparamagnetic Iron Oxide Nanoparticles (SPIONs) in a GL261 Xenograft Glioblastoma Model [Corrigendum]

Klapproth AP, Shevtsov M, Stangl S, Li WB, Multhoff G. *Int J Nanomedicine*. 2020;15:4677–4689.

The authors have advised the author and affiliation list on page 4677 is incorrect. The correct author list and affiliations are as follows.

Alexander P Klapproth^{1,2,*}
Maxim Shevtsov^{1,3–7,*}
Thomas J Carter⁸
Stefan Stangl¹
Kerry Chester⁸
Wei Bo Li²
Gabriele Multhoff¹

¹Center for Translational Cancer Research Technische Universität München (TranslaTUM), Klinikum Rechts Der Isar, Munich, Germany; ²Institute of Radiation Medicine, Helmholtz Zentrum München, German Research Center for Environmental Health (GmbH), Munich, Germany; ³Institute of Cytology of the Russian Academy of Sciences (RAS), St. Petersburg, Russia; ⁴Department of Biotechnology, First Pavlov State Medical University of St. Petersburg, St. Petersburg, Russia; ⁵Almazov National Medical Research Centre, Russian Polenov Neurosurgical Institute, St. Petersburg, Russia; ⁶National Center for Neurosurgery, Nur-Sultan, Kazakhstan; ⁷Department of Biomedical Cell Technologies, Far Eastern Federal University, Vladivostok, Russia; ⁸UCL Cancer Institute, University College London, London, UK

*These authors contributed equally to this work

Page 4682, Intravenously Injected SPIONs section, the text “To further validate the model, two datasets from mice with intravenously injected SPIONs were analyzed” should read “To further validate the model, two previously published supplementary datasets from mice with intravenously injected SPIONs were analyzed”.

The authors apologize for these errors.

International Journal of Nanomedicine

Dovepress

Publish your work in this journal

The International Journal of Nanomedicine is an international, peer-reviewed journal focusing on the application of nanotechnology in diagnostics, therapeutics, and drug delivery systems throughout the biomedical field. This journal is indexed on PubMed Central, MedLine, CAS, SciSearch[®], Current Contents[®]/Clinical Medicine,

Journal Citation Reports/Science Edition, EMBase, Scopus and the Elsevier Bibliographic databases. The manuscript management system is completely online and includes a very quick and fair peer-review system, which is all easy to use. Visit <http://www.dovepress.com/testimonials.php> to read real quotes from published authors.

Submit your manuscript here: <https://www.dovepress.com/international-journal-of-nanomedicine-journal>

**A.3. Multi-scale Monte Carlo simulations of gold
nanoparticle-induced DNA damages for kilovoltage
X-ray irradiation in a xenograft mouse model using
TOPAS-nBio**

Authors: A.P. Klapproth, J. Schuemann, S. Stangl, T. Xie, W.B. Li, G. Multhoff


A.3.1. Article

RESEARCH

Open Access



Multi-scale Monte Carlo simulations of gold nanoparticle-induced DNA damages for kilovoltage X-ray irradiation in a xenograft mouse model using TOPAS-nBio

Alexander P. Klapproth^{1,2*} , Jan Schuemann^{3,4*}, Stefan Stangl¹, Tianwu Xie^{5,6}, Wei Bo Li^{2*} and Gabriele Multhoff¹

*Correspondence: klapproth@mytum.de; jschuemann@mgh.harvard.edu; wli@helmholtz-muenchen.de
¹ Center for Translational Cancer Research Technische Universität München (TranslaTUM), Klinikum rechts der Isar, Munich, Germany
² Institute of Radiation Medicine, Helmholtz Zentrum München, German Research Center for Environmental Health (GmbH), Munich, Germany
³ Physics Division, Department of Radiation Oncology, Massachusetts General Hospital, Boston, MA, USA
Full list of author information is available at the end of the article

Abstract

Background: Gold nanoparticles (AuNPs) are considered as promising agents to increase the radiosensitivity of tumor cells. However, the biological mechanisms of radiation enhancement effects of AuNPs are still not well understood. We present a multi-scale Monte Carlo simulation framework within TOPAS-nBio to investigate the increase of DNA damage due to the presence of AuNPs in mouse tumor models.

Methods: A tumor was placed inside a voxel mouse model and irradiated with either 100-kVp or 200-kVp X-ray beams. Phase spaces were employed to transfer particles from the macroscopic (voxel) scale to the microscopic scale, which consists of a cell geometry including a detailed mouse DNA model. Radiosensitizing effects were calculated in the presence and absence of hybrid nanoparticles with a Fe₂O₃ core surrounded by a gold layer (AuFeNPs). To simulate DNA damage even for very small energy tracks, Geant4-DNA physics and chemistry models were used on microscopic scale.

Results: An AuFeNP-induced enhancement of both dose and DNA strand breaks has been established for different scenarios. Produced chemical radicals including hydroxyl molecules, which were assumed to be responsible for DNA damage through chemical reactions, were found to be significantly increased. We further observed a dependency of the results on the location of the cells within the tumor for 200-kVp X-ray beams.

Conclusion: Our multi-scale approach allows to study irradiation-induced physical and chemical effects on cells. We showed a potential increase in cell radiosensitization caused by relatively small concentrations of AuFeNPs. Our new methodology allows the individual adjustment of parameters in each simulation step and therefore can be used for other studies investigating the radiosensitizing effects of AuFeNPs or AuNPs in living cells.

Keywords: Monte Carlo simulation, Nanoparticles, Radiosensitization, Radiation therapy, Geant4, TOPAS, TOPAS-nBio



© The Author(s). 2021. **Open Access** This article is licensed under a Creative Commons Attribution 4.0 International License, which permits use, sharing, adaptation, distribution and reproduction in any medium or format, as long as you give appropriate credit to the original author(s) and the source, provide a link to the Creative Commons licence, and indicate if changes were made. The images or other third party material in this article are included in the article's Creative Commons licence, unless indicated otherwise in a credit line to the material. If material is not included in the article's Creative Commons licence and your intended use is not permitted by statutory regulation or exceeds the permitted use, you will need to obtain permission directly from the copyright holder. To view a copy of this licence, visit <http://creativecommons.org/licenses/by/4.0/>. The Creative Commons Public Domain Dedication waiver (<http://creativecommons.org/publicdomain/zero/1.0/>) applies to the data made available in this article, unless otherwise stated in a credit line to the data.

Background

The optimization of radiotherapy is a wide and thoroughly studied field. A major limitation of external beam radiation therapy is the fact that it cannot be applied without harming healthy normal tissue around the tumor. One promising approach to reduce healthy tissue toxicity is the local enhancement of the radiation dose within the tumor using radiosensitizers, such as gold nanoparticles (AuNPs). AuNPs are among the most investigated nanomaterials for medical application, due to their favorable biocompatibility and their potential use as a contrast agent (Dai et al. 2017; Chen et al. 2016; Xin et al. 2017). The radiosensitizing effect of AuNPs is partially based on their potential to release high numbers of secondary electrons upon irradiation, which has been shown to be especially potent for kilovoltage photon beams around 100 kVp. In this energy range, the dose enhancement is mostly caused by secondary electrons with low energy such as Auger electrons with a limited range (Lechtman and Pignol 2017). Because of the highly localized effects of the radiosensitization and the possibility of AuNPs to accumulate also in healthy tissues, reliable targeting agents such as antibodies are important to make AuNP-based therapies applicable in clinical practice (Schuemann et al. 2016).

Sensitization effects of AuNPs can be studied via Monte Carlo simulations by computing the dose enhancement effect caused by AuNPs in appropriate scenarios. However, it is still not possible to precisely calculate the impact of a single AuNP on its direct microenvironment, although multiple studies have been dedicated to this topic (Li et al. 2014, 2020; Lin et al. 2014; Sung et al. 2016; Rabus et al. 2019; Haume et al. 2018). When it comes to scenarios with multiple AuNPs, a frequently used approach was the employment a local effect model (LEM)-based estimation (Kraft et al. 1999). These models usually calculate the enhancement of the effectiveness of irradiation through the addition of multiple AuNPs by extrapolating radial dose enhancements obtained from MC simulations with a single AuNP. Although they add additional assumptions and uncertainties, LEMs were commonly used to describe the dose enhancement effect of multiple AuNPs, since MC simulations on their own have been shown to underestimate the effects of radiation when compared to experimental results (McMahon et al. 2011). One reason for that is probably the lack of chemical interactions in MC simulations, which usually only compute the effects of physical interactions with a focus on secondary electrons (Kuncic and Lacombe 2018). Chemical radicals produced by water radiolysis have, however, been shown to play a significant role in the radiosensitizing effects of AuNPs (Xie et al. 2015; Rosa et al. 2017).

In this study, we introduce a multi-scale method to directly compute the DNA damage induction of ionized radiation with and without nanoparticles with a gold surface using TOPAS-nBio (Schuemann et al. 2019a). TOPAS-nBio is a radiobiology focused extension to TOPAS (Perl et al. 2012), which is a user friendly Monte Carlo toolkit based on Geant4 (Agostinelli et al. 2003). TOPAS-nBio includes a chemistry interface that employs an updated version of Geant4-DNA water radiolysis models, which were applied in our nano-scale cell simulations (Karamitros et al. 2014; Ramos-Mendez et al. 2018). Rudek et al. (2019) already observed AuNP-induced dose enhancement assuming these models. The effect on DNA damage in a detailed human nucleus model was investigated by Zhu et al. (2020a). We aim to build on both results to gain a better

understanding of the radiosensitization effect of AuNPs in tumor cells by introducing a new methodology of simulating according preclinical in vivo experiments.

Our calculations were performed in three steps: mouse model, tumor and cell. On the macro-scale, a voxel mouse model including a mammary gland tumor was irradiated by an X-ray beam. Phase spaces were employed to move between the scales until detailed DNA damage could be calculated in a nano-scale cell model.

Materials and methods

All MC simulations were carried out in TOPAS v3.2 for Linux machines and Geant4 v10.5p1. For reproducibility, all developed extensions and parameter files were made generally accessible via Github (Link: https://github.com/AKlapproth/MultiScale_AuNP_TOPAS). Simulations were performed in three major steps: mouse model, tumor and cell. The particles were transferred from one step to the next via phase space files. These files take a snapshot of all tracks passing a given surface and include all the necessary information for each scored track to be recreated in the next stage of our simulations. The information included were particle type, energy, location and momentum at the time of scoring. The initial beam spectra were calculated with SpecCalc employing the parameters from the small animal radiation research platform (SARRP) device to simulate a realistic experimental setup (Wong et al. 2008).

For mouse model and tumor simulations, the standard Geant4 electromagnetic physics list option 3 was used. It is focused on electron, hadron and ion tracking outside a magnetic field and the most accurate standard model for medical applications in the micrometer range or above (Physics Lists EM constructors in Geant4 10.4 2021; Allison et al. 2016). The use of more accurate physics lists on these scales would have caused an immense increase in computation time with no significant benefit. This is because most of the low energy tracks, which are the most time-consuming to simulate, occur in locations, where they have no effect on the outcome. For the cell simulations, we applied a combination of two more accurate physics lists to make the outcome on the nanometer scale as accurate as possible. The exact physics setup in the cells is explained in the subsection "Cells".

The nanoparticles, which were used in the cell simulations, were hybrid nanoparticles. While their surface consists of a 1-nm-thick gold layer, they feature an Fe₂O₃ core with a diameter of 2nm, adding up to an overall diameter of 4nm. We selected these nanoparticles to describe an experimental setup that was conducted for theranostic purposes (Kang et al. 2020). The iron oxide core offers advantages for both therapy and diagnostics, since it enables the gold-Fe₂O₃ hybrid nanoparticles (AuFeNPs) to be detectable via MRI scans.

Mouse model

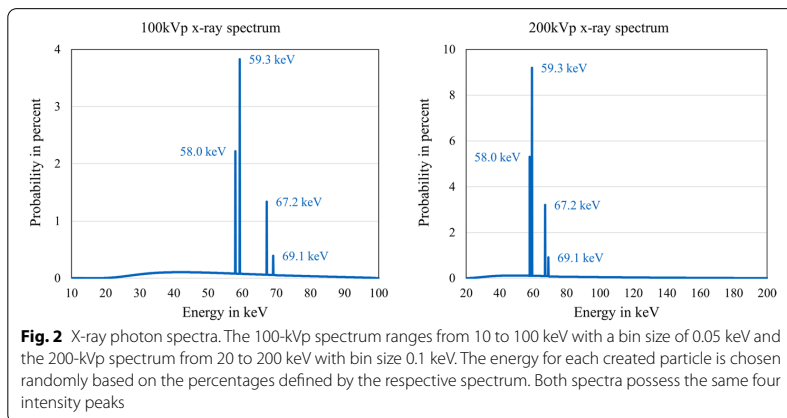
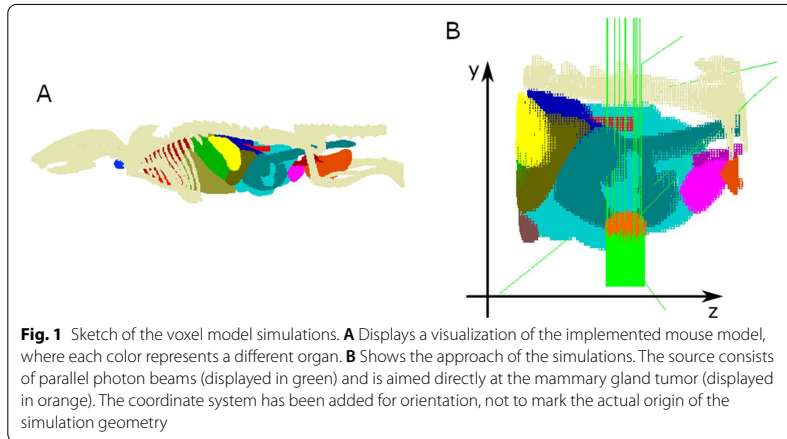
The voxel model of a 21 g mouse developed by Xie and Zaidi (2013) was used and embedded in a 120 × 120 × 160 mm³ box filled with air (cf. Fig. 1A). The model consists of 200 × 200 × 512 cubical voxels with a border length of 200 μm. A new TOPAS extension was developed that allows the insertion of an ellipsoid shaped tumor at any location inside the model. Normal tissue, skin and air in the defined area is then replaced by tumor tissue. In case the tumor extends outside the body, exposed tumor tissue is

covered by a layer of skin with a thickness of one voxel. For this work, a tumor with diameters 5 mm × 4 mm × 5 mm was planted near the left hind leg to simulate a mammary gland carcinoma. Different materials were defined for each component of the model, either a predefined material available in Geant4 or water with an adjusted density (cf. Table 1). The respective densities were chosen according to previous studies with this mouse model (Xie and Zaidi 2013). Since the tumor consisted of water in the following simulation steps due to limitations in the availability of physics parameters for sub-cell scale simulations, standard G4_WATER material was used for the tumor in this step as well to ensure consistency. Two different types of kVp photon beams were used for the simulated treatment, both based on the radiation source used in the SARRP, when set to either 100 kVp or 200 kVp. The respective photon spectra were calculated with the SpekCalc toolkit and are shown in Fig. 2 (Poludniowski et al. 2009). Particle tracks originated from a flat, circular particle source placed 20 cm below (i.e., shifted along the y-axis) the tumor center. Its diameter was set to 5 mm, according to the tumor's X- and Z-diameters (cf. Fig. 1B). All particles entering the tumor were scored in a phase space file and multiplied 750 times, which means for each particle scored during the simulation 750 entries were made in the phase space file, each with the same particle type and energy. To increase variance each duplicated particle was positioned on a randomly generated point on the tumor surface, while its momentum was rotated accordingly around the center. Particles that still possessed the initial momentum along the y-axis

Table 1 Definition of materials in the mouse model simulations

Body part	G4 material	Density in g/cm ³
Air	G4_AIR	1.205 × 10 ⁻³
Normal tissue	G4_TISSUE_SOFT_ICRP	1.03
Skeleton	G4_BONE_COMPACT_ICRU	1.85
Heart	G4_WATER	1.06
Lung	G4_LUNG_ICRP	1.04
Liver	G4_WATER	1.05
Stomach	G4_WATER	1.04
Kidney	G4_WATER	1.05
Small intestine	G4_WATER	1.04
Spleen	G4_WATER	1.06
Bladder	G4_WATER	1.04
Testes	G4_TESTIS_ICRP	1.04
Skin	G4_SKIN_ICRP	1.09
Gallbladder	G4_WATER	1.03
Brain	G4_BRAIN_ICRP	1.04
Thyroid	G4_WATER	1.05
Pancreas	G4_WATER	1.05
Vas deferens	G4_WATER	1.04
Large intestine	G4_WATER	1.04
Airway	G4_AIR	1.205 × 10 ⁻³
Blood	G4_WATER	1.00
Tumor	G4_WATER	1.00

For each body part, either the regarding Geant4 Material or G4_WATER with an adjusted density was applied

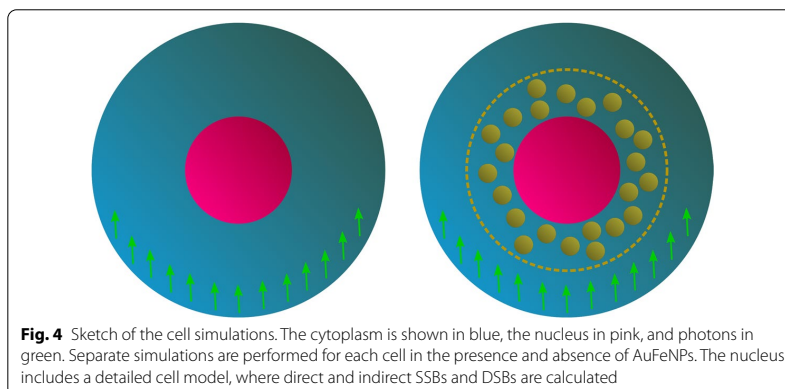
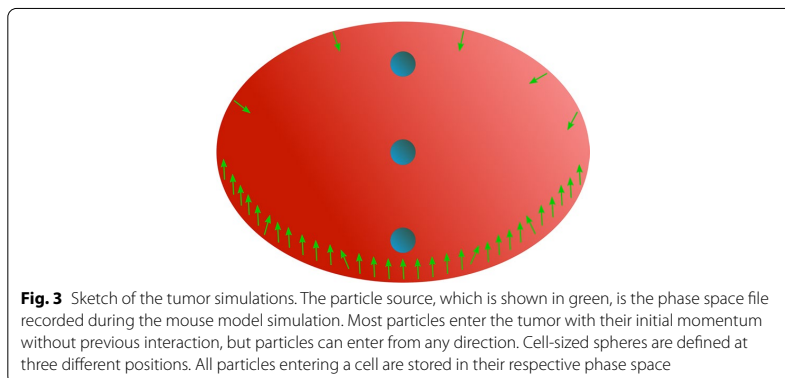


were assigned a random position on the tumor surface at its bottom or Y-Minus side. All other particles were rotated randomly around the y-axis going through the tumor center.

Tumor

For simulations inside the tumor the entire geometry setup consisted of water to ensure consistency throughout the simulation steps. An ellipsoidal water phantom with diameters of 5 mm× 4 mm× 5 mm was defined as the tumor. Spheres with a diameter of 100 μm were placed at 3 different positions inside the tumor to represent cellular regions of interest (cf. Fig. 3). For each of the spheres, all particles entering the volume were scored in a second phase space file.

Parameters were chosen to emulate a mammary carcinoma in a xenograft mouse model. A popular cell line for this purpose is 4T1 mouse tumor cells. Since they tend to metastasize in the mammary gland, when transplanted on another location, and show some similarities to human mammary carcinomas, they are an ideal choice for



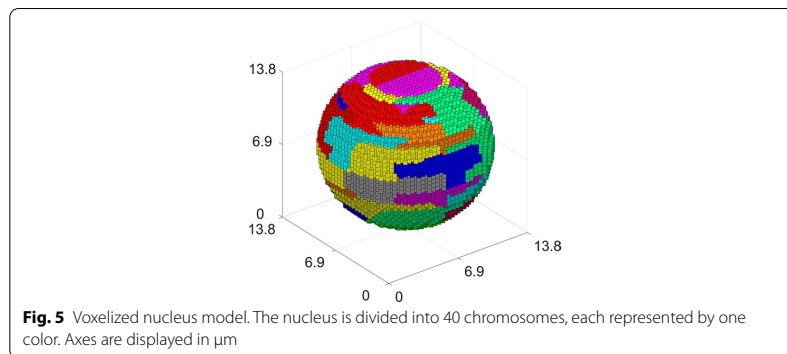
mammary xenograft tumors (Pulaski and Ostrand-Rosenberg 2001). 4T1 cells are triple-negative breast cancer cells, which means they test negative for both the expression of estrogen receptors, progesterone receptors and an overexpression of the HER2 protein. Patients with triple-negative breast cancer usually have a relatively poor prognosis, since the tumors do not respond to many commonly used treatment methods (Foulkes et al. 2010). These tumor cells are therefore of high interest regarding new and optimized treatment methods (Takai et al. 2016).

Cells

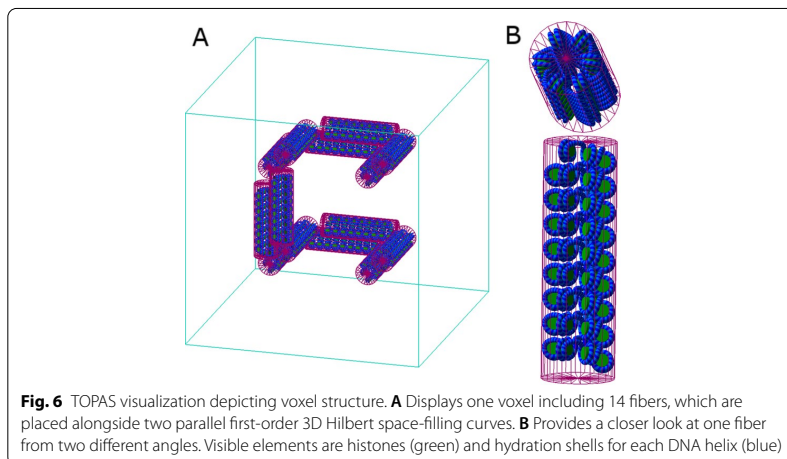
Cells were built as spheres with a diameter of 20 μm and a nucleus diameter of 13.8 μm according to parameters of 4T1 tumor cells (cf. Fig. 4) (Oelze et al. 2004). The nucleus was placed at the center of the cell and filled with DNA using a model based on the human DNA model published by Zhu et al. (2020a, b). The model was modified to conform to the male mouse genome by adjusting the voxel count, voxel size and the number of chromatin fibers per voxel. The resulting nucleus has a diameter of 13.8 μm and each chromosome contains a realistic number of base pairs. The voxels and base pairs per chromosome can be found in Table 2, and a sketch of the resulting nucleus structure

Table 2 Number of voxels and base pairs per chromosome (Source of genome data: Genome Reference Consortium (<https://www.ncbi.nlm.nih.gov/genome/52>))

Chromosome ID	Voxels	Base pairs in Mbp
1 & 2	922	195.6
3 & 4	859	182.2
5 & 6	755	160.1
7 & 8	738	156.5
9 & 10	716	151.9
11 & 12	706	149.7
13 & 14	686	145.5
15 & 16	610	129.4
17 & 18	587	124.5
19 & 20	616	130.7
21 & 22	576	122.2
23 & 24	566	120.0
25 & 26	568	120.5
27 & 28	589	124.9
29 & 30	491	104.1
31 & 32	463	98.20
33 & 34	448	95.02
35 & 36	428	90.78
37 & 38	290	61.51
X	806	171.0
Y	430	91.20



in Fig. 5. The nuclear model is voxelized and possesses the same structural hierarchy as the human model. The DNA double helix consists of half-cylindrical base volumes and quarter-cylindrical sugar-phosphate backbone volumes surrounded by a hydration shell. The DNA is wrapped around the cylindrical histone protein complex, building the nucleosome. Each chromatin fiber is in turn made up of 51 nucleosomes connected to each other by nucleotide pairs and arranged to form a helix (cf. Fig. 6B). 15.15 kilo base pairs of DNA are included in each chromatin fiber, which were placed in each voxel along two space-filling 3D Hilbert curves with one iteration (Lieberman-Aiden et al.



2009; McNamara et al. 2018), as illustrated in Fig. 6A. Figure 6B provides a more detailed depiction of each fiber and how the DNA double helix is wrapped around the histones. The nucleus consists of 24,464 cubical voxels with a border length of 3.833 μm , which are divided into 40 chromosomes. All in all, the nucleus includes around 5.19 Giga base pairs of DNA.

The phase spaces from the tumor simulation were used as source. Each particle's distance to the cell center was reduced to 10 μm , while its momentum, particle type and energy stayed unchanged. Particles were then multiplied 100 times, which means for each particle scored during the tumor simulation, 100 particles originated in the respective cell simulations. To increase variance, position and momentum were rotated randomly around the y -axis going through the cell, while the other parameters remained unchanged. All simulations were performed twice, once without AuFeNPs and once with 1 Mio AuFeNPs placed randomly around the nucleus with a maximum distance of 100 nm (cf. Fig. 4). This results in an AuFeNP concentration of around 0.225% by weight in relation to the cell. The cytoplasm and nucleus consist of water in the simulations, so the Geant4-DNA-based physics and chemistry lists (Incerti et al. 2018), which simulate the full particle track structure and are part of TOPAS-nBio, could be used in these regions. The standard G4_WATER material was used in all regions of the nucleus except the DNA backbone where the density of water was adjusted to 1.407 g/cm^3 (Smialek et al. 2013). Due to limitations in available cross sections in Geant4-DNA, the Geant4 Livermore physics model was applied in gold and Fe_2O_3 . Production cut and electromagnetic range were both set to 10 eV and 1 MeV and the cut for electrons was defined as 0.1 nm. To achieve the combination of two different models two regions were defined, one containing all AuFeNPs and one all other parts within the cell. The simulation switched between the two electromagnetic physics models depending on the region a particle traversed. Accordingly, only physics interactions (condensed histories) were tracked and generated inside AuFeNPs, while in the rest of the cell (water) we also simulated the propagation of chemical species.

For the computation of DNA damage based on our track structure simulations, we chose standard assumptions and parameters used in previous Monte Carlo studies (Ramos-Mendez et al. 2018; Rudek et al. 2019; Lampe et al. 2018; Meylan et al. 2017; Sakata et al. 2019). Direct damage was only produced by interactions in the DNA backbone including the adjacent hydration shells. Indirect damage was only produced in the DNA backbone. If at least 17.5 eV (Rudek et al. 2019; Lampe et al. 2018; Sakata et al. 2019) of deposited energy caused by physical interactions in a single back bone including its hydration shell was scored during one history, it was considered as a direct strand break (SB). The chemistry model was applied according to the work of Zhu et al. (2020a) with a chemical stage time of 1.0 ns. Six different particle types that are included in the standard Geant4-DNA chemistry extension were quantified, namely hydrogen radicals ($\text{H}\cdot$), molecular hydrogen (H_2), hydrogen peroxide (H_2O_2), hydronium (H_3O^+), solvated electrons (e_{aq}) and the hydroxyl group (OH), which includes hydroxide (OH^-) and hydroxyl radicals ($\cdot\text{OH}$). Chemical species produced inside DNA regions were immediately killed to emulate that no water radiolysis occurs there. $\text{H}\cdot$, e_{aq} and $\cdot\text{OH}$ diffusing into DNA regions were also immediately terminated. Only $\cdot\text{OH}$ radicals that had just entered the DNA backbone were able to induce an indirect SB with a probability of 40% (Meylan et al. 2017; Sakata et al. 2019).

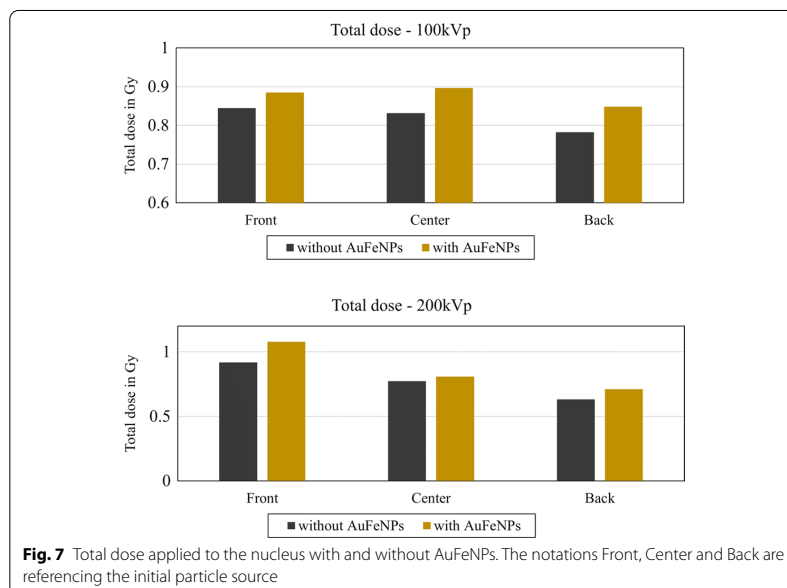
Damage was estimated in form of direct and indirect single-strand breaks (SSBs) and double-strand breaks (DSBs). Direct damage is caused by physical interactions and indirect damage by chemical radicals. Two SBs that occur on opposing DNA strands with a distance of 10 or fewer base pairs were defined as a DSB. When scored, DSBs were classified depending on the types of their underlying SBs into direct DSBs (two direct SBs) indirect DSBs (two indirect SBs) and hybrid DSBs (one of each). The results were displayed in the standard DNA damage (SDD) data format (Schuermann et al. 2019b). In addition, the number of produced chemical species was counted and classified by type.

Results

Our simulation results show that the cell depth as well as the presence of AuFeNPs affects the simulation results. The exact values of the results and the respective standard deviations can be found in Additional file 1: Tables S1–S12.

As shown in Fig. 7, the dose applied to the nucleus is increased in scenarios, where AuFeNPs are present for each cell location inside the tumor. The position itself also plays a role for the results, as the dose decreases the further back a cell lies in relation to the particle source. This location effect was only significant for simulations with 200-kVp photons.

The SB count shows the same behavior and is increased in simulations including AuFeNPs around the nucleus and decreases with increasing depth only for 200-kVp photons (cf. Fig. 8). Indirect SBs generally account for around twice the number of direct SBs, which conforms to previous findings (Zhu et al. 2020a). Notably, the dose and damage increase was observed in all scenarios, although the concentration of AuFeNPs was relatively low in comparison to previous AuNP studies (Sung et al. 2017; Sung and Schuermann 2018).



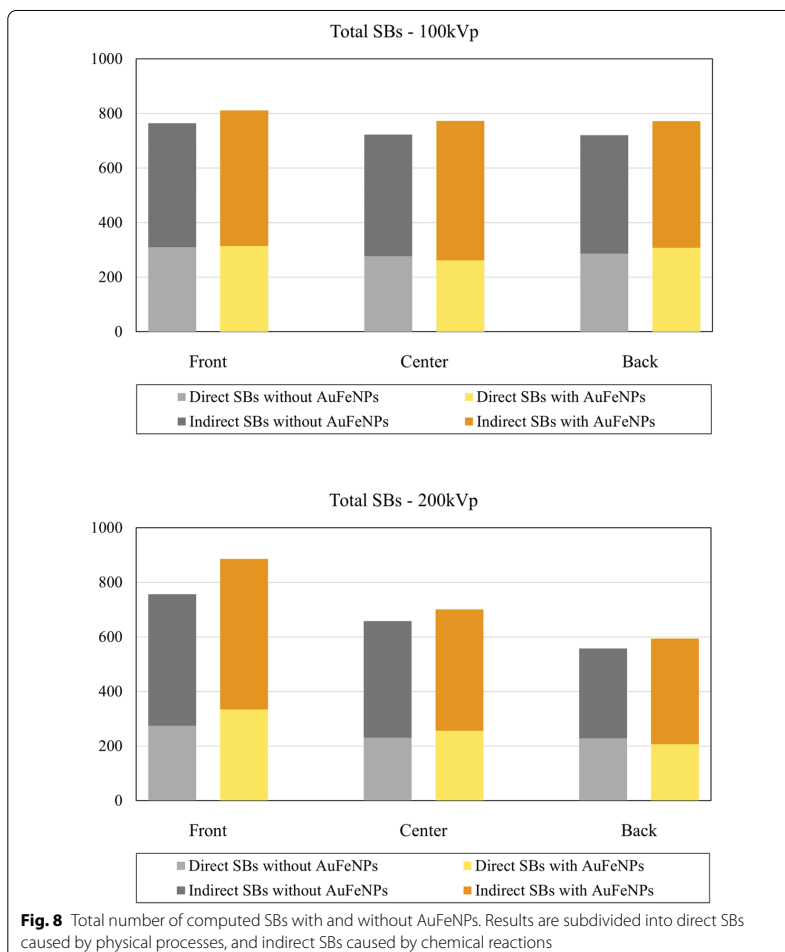
In accordance with the proportion between direct and indirect SBs, indirect and hybrid DSBs outweigh direct DSBs in all simulations (cf. Fig. 9). A clear shift in DSB-type ratios depending on AuFeNP presence or cell location could not be detected.

The effect of AuFeNPs is especially prominent when examining the count of produced chemical species for different scenarios (cf. Fig. 10). A clear enhancement in the presence of AuFeNPs can be observed for each investigated location and photon spectrum. The increase of total numbers is mainly attributed to the very high enhancement ratios of OH and H₂. However, not all chemical radical counts are increased, when adding AuFeNPs. The count of H₃O particles and e_{aq} decrease significantly (cf. Table 3). We exclusively considered ·OH for the scoring of indirect DNA damages, as hydroxyl radicals are generally considered to be the mediator of much of the induced DNA damage (Balasubramanian et al. 1998). Therefore, the increase of produced OH radicals is especially relevant and directly connected to the observed increase in indirect DNA damage. Analogically to the already mentioned results, we also observe an overall decrease of produced chemical species as a function of depth for 200-kVp photons.

Discussion

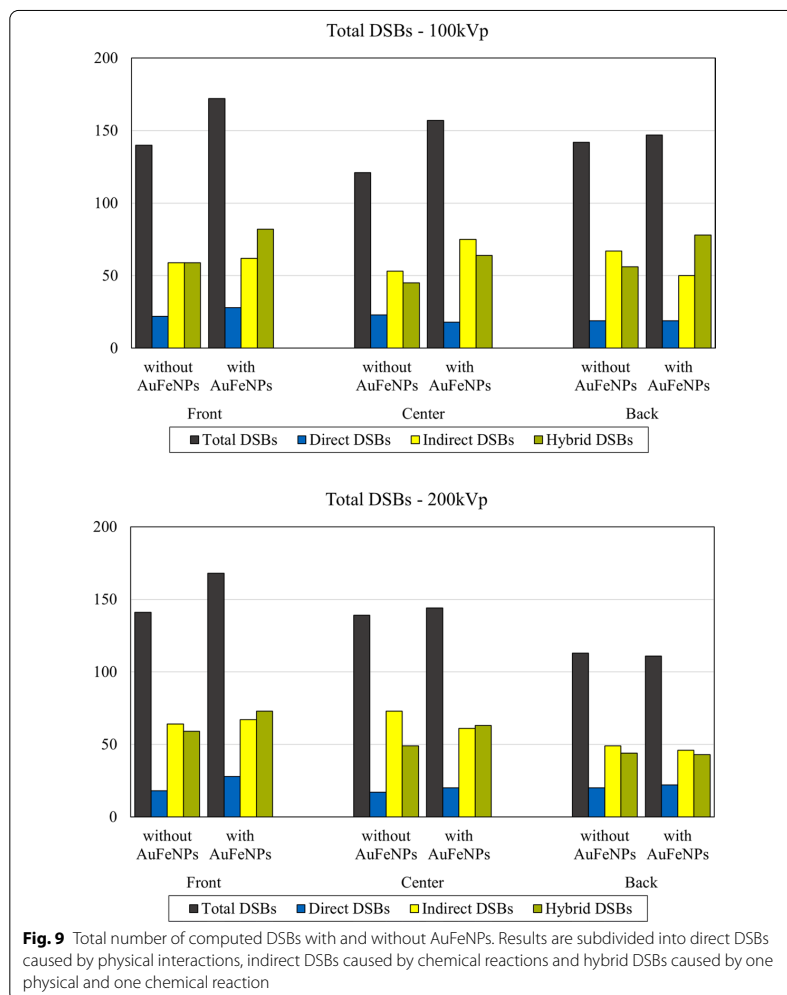
We successfully developed a method for multi-scale simulations of mouse tumor irradiations in radiobiological experiments, from large scale (mouse model) to small scale (DNA). This is a major step away from LEM-based models, allowing for a better understanding and more accurate modeling of in vivo experiments. This was in part achieved by accounting for realistic effects on the radiation field of tumors within the mouse geometry and by including chemical reactions that are induced by radiolysis.

In our simulations, we detected an enhancement of deposited energy and chemical radicals produced by water radiolysis in simulations including AuFeNPs, resulting



in increased DNA damage. The overall trends of the results agree with previous studies, indicating validity of this new, multi-scale methodology (Ramos-Mendez et al. 2018; Rudek et al. 2019; Zhu et al. 2020a, b). When irradiated, the depth of a cell inside the tumor affects the dose that is applied to its nucleus. This naturally also affects the amount of DNA damage, which is illustrated by the number of strand breaks. The addition of gold nanoparticles causes a small but significant increase in both direct and indirect strand breaks, which is caused by secondary electrons and their adjunctive chemical species. However, some limitations have to be kept in mind with regard to the results.

In the MC simulations, many physical, chemical and biological parameters were used, and these parameters are mostly evaluated from experimental data, and they are subject to large uncertainties. The physical parameters such as cross sections for electrons have an uncertainty of 5% at the lower energy of 1 keV, 17–20% uncertainty at very low energy



of 100 eV in water (Thomson and Kawrakow 2011). In contrast, the chemical and biological parameters are mostly derived from in vitro cellular and molecular experimental reactions and radiobiological effects, and they compose even larger uncertainties (Zhu et al. 2020b).

In the present study, we did not perform a detailed uncertainty analysis of the results of SSBs, DSBs and chemical species shown in Figs. 7, 8, 9, 10. Such an analysis would require significant further work on parameters analysis as performed in the work of Zhu et al. However, as Zhu et al. found out, the threshold energy of 17.5 eV used in this study and the probability of radicals for generating an indirect damage, account for most of the uncertainty of SSBs and DBSs. Zhu et al. (2020b) estimated differences of up to 34% and 16% for SSB and DSB yields, respectively, caused by all

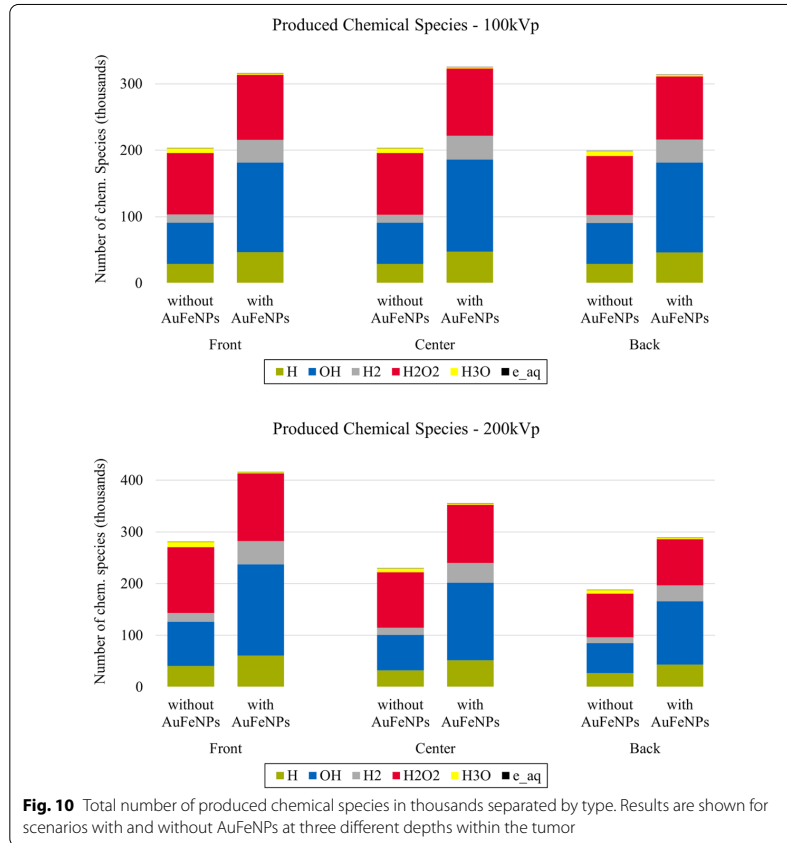


Fig. 10 Total number of produced chemical species in thousands separated by type. Results are shown for scenarios with and without AuFeNPs at three different depths within the tumor

Table 3 The effect of AuFeNPs on the production of chemical species

Type	100 kVp			200 kVp		
	Front	Center	Back	Front	Center	Back
H	1.615	1.645	1.592	1.506	1.603	1.590
OH	2.165	2.232	2.194	2.053	2.176	2.115
H ₂	2.784	2.944	2.893	2.689	2.820	2.753
H ₂ O ₂	1.061	1.094	1.072	1.026	1.052	1.061
H ₃ O	0.295	0.268	0.306	0.230	0.303	0.345
e _{aq}	0.593	0.467	0.553	0.423	0.375	0.5

Each value is the number of produced chemical species in simulations with AuFeNPs divided by the respective number without AuFeNPs

the parameters used in TOPAS-nBio. These uncertainties are applicable to our work as well.

The major limitation for the simulations is the lack of models for chemical interactions inside and on the surface of AuFeNPs. This means that each chemical track

encountering an AuFeNP is instantly eliminated (i.e., equivalent to reacting with the AuFeNP without consequence) and can no longer produce DNA damage. Rudek et al. found that AuNPs could thus lead to a reduction of availability of chemical species when modeled with track structure MC codes (Rudek et al. 2019). This is a considerable discrepancy between simulations and reality, where interactions between chemical radicals and gold atoms exist and can cause downstream reactions. Cheng et al. (2012) detected an enhancement of chemical activity around AuNPs that could not only be explained by water radiolysis caused by X-rays. They attributed this effect to the activation of gold atoms on the surface of AuNPs by superoxides. In addition, there are still no reliable models for the surface chemistry of gold layered nanoparticles themselves, which have been shown to enhance reactive oxygen species (ROS) production (Pan et al. 2009; Liu et al. 2014; Sicard-Roselli et al. 2014; Seo et al. 2017). Possible charge accumulations in the AuFeNPs and their surface could further affect the reactions or influence which species are attracted (or repelled) by the AuFeNPs. Another factor to consider regarding in vivo studies is the nanoparticle coating necessary for targeting and biocompatibility. Xiao et al. (2011) showed that such coatings can decrease the radiosensitization effect of AuNPs significantly. Such coatings can further impact the chemical reactions around the GNPs.

Another limitation is the currently available physics models of Geant4-DNA, which do not yet include cross sections for gold. Thus, standard Livermore models were employed, which show good accuracy for keV electrons, but show limitations below the 100 eV range (Sakata et al. 2018). The detected effect of AuFeNPs was narrow and no increase in the fraction of SBs involved in DSBs was detectable, which might be expected due to the agglomeration of damaging events around the nanoparticles. A possible reason might be the distance of AuFeNPs to regions that contain DNA and thus are relevant for the results, due to the relatively low concentration of DNA inside the nucleus. There was still a definite AuFeNP-related increase in SBs, dose and chemical species detected for all depths, which is in agreement with previous results (Ramos-Mendez et al. 2018; Rudek et al. 2019). The release of additional physics models will be a big help in improving and validating simulation results for the physical effects of AuFeNPs.

The next important step will be the validation of simulation results in biological experiments. As the study of Zhu et al. (2020b) showed, simulations are sensitive to the chosen parameters and physics models. Experimental data will therefore play a crucial role in deciding which simulation parameters can accurately describe observed phenomena. The output in form of SSBs and DSBs can be used to compare cell survival outcomes from in vitro experiments and in vivo studies with mice. The described multi-scale approach can further be used to investigate the effect of AuFeNPs at the involved scales and on the efficiency of AuFeNP-enhanced radiotherapy.

Conclusions

In this work, a new Monte Carlo-based method was established to simulate radiation-induced DNA damages in AuNP or AuFeNP-assisted radiotherapy. This multi-scale approach covers the whole range of preclinical in vivo studies and can therefore be valuable for parameter optimization and analyzing results in clinical cancer radiotherapy settings in the future. Including the AuFeNPs in the simulation geometry, as

opposed to using a LEM-based approach, utilizes the ongoing increase in both processing power of computers and advancement of Monte Carlo models to produce more accurate and traceable results. The detailed nucleus model allows direct counting and classification of SSBs and DSBs and the output in the SDD format makes the results comparable to similar studies and experimental data (Schuemann et al. 2019b). The results show that even low concentrations of gold can cause a noticeable increase in DNA damage after kV irradiations and highlights the importance of taking chemical interactions into account.

The inclusion of the tumor as a separate step allows the consideration of tumor heterogeneity in future studies. It is well known that the tumor landscape can differ vastly for different locations of the same tumor, with changing AuFeNP uptake and penetration, cell type, radiosensitivity and microenvironment (Alfonso and Berk 2019; Dagogo-Jack and Shaw 2018; Marusyk and Polyak 2010; Zhivotovsky et al. 1999). These effects can be taken into account, for example, by including different SB probabilities for different cell locations or adjusting repair parameters, when calculating cell survivability.

This methodology is not restricted to X-ray or metal nanoparticle studies. It can be easily adjusted to cover all investigations of radiation-induced DNA damage. The inclusion of a complete mouse model enables dosimetry applications in organs of interest. Human cell studies can be performed by replacing the mouse model with a phantom displaying the respective area of interest, adjusting cell size, and replacing the mouse DNA model with the already established human equivalent (Zhu et al. 2020a). The kVp photon beam may be replaced by any other radiation source supported by TOPAS, e.g., MV photon beams (LINAC) or proton beams for studies with or without nanoparticles. This work can be used as a template for future multi-scale radiation studies in different settings.

Abbreviations

AuNP: Gold nanoparticle; AuFeNP: Gold-Fe₂O₃ hybrid nanoparticle; LEM: Local effect model; RBE: Relative biological effectiveness; SARRP: Small animal radiation research platform; SB: Strand break; SSB: Single-strand break; DSB: Double-strand break; SDD: Standard DNA damage; ROS: Reactive oxygen species.

Supplementary Information

The online version contains supplementary material available at <https://doi.org/10.1186/s12645-021-00099-3>.

Additional file 1: Table S1. Simulation results and standard deviations - 100 kVp, front cell, without AuFeNPs. **Table S2.** Simulation results and standard deviations - 100 kVp, front cell, with AuFeNPs. **Table S3.** Simulation results and standard deviations - 100 kVp, center cell, without AuFeNPs. **Table S4.** Simulation results and standard deviations - 100 kVp, center cell, with AuFeNPs. **Table S5.** Simulation results and standard deviations - 100 kVp, back cell, without AuFeNPs. **Table S6.** Simulation results and standard deviations - 100 kVp, back cell, with AuFeNPs. **Table S7.** Simulation results and standard deviations - 200 kVp, front cell, without AuFeNPs. **Table S8.** Simulation results and standard deviations - 200 kVp, front cell, with AuFeNPs. **Table S9.** Simulation results and standard deviations - 200 kVp, center cell, without AuFeNPs. **Table S10.** Simulation results and standard deviations - 200 kVp, center cell, with AuFeNPs. **Table S11.** Simulation results and standard deviations - 200 kVp, back cell, without AuFeNPs. **Table S12.** Simulation results and standard deviations - 200 kVp, back cell, with AuFeNPs.

Acknowledgements

We want to thank José Ramos-Méndez for his much-appreciated input regarding water radiolysis simulations.

Authors' contributions

The study was designed by AK, JS and WL. The manuscript was written by AK, JS and WL with substantial revisions of GM and SS. TX designed and provided the mouse model and contributed valuable comments. All authors read and approved the final manuscript.

Funding

This study was supported by DFG grant (SFB824/3, STA1520/1-1), Technische Universität München (TUM) within the DFG funding program Open Access Publishing. The TUM Graduate School Internationalization Grant financially supported Alexander Klapproth's research stay at the Massachusetts General Hospital, Boston. Jan Schuemann was in part supported by the National Institutes of Health (NIH)/National Cancer Institute (NCI), grant no. R01 CA187003.

Availability of data and materials

All data generated or analyzed during this study are included in this published article and its supplementary information. All developed extensions and parameter files necessary for replication are available in the Github repository, (https://github.com/AKlapproth/MultiScale_AuNP_TOPAS).

Declarations**Ethics approval and consent to participate**

Not applicable.

Consent for publication

Not applicable.

Competing interests

The authors declare that they have no competing interests.

Author details

¹Center for Translational Cancer Research Technische Universität München (TranslaTUM), Klinikum rechts der Isar, Munich, Germany. ²Institute of Radiation Medicine, Helmholtz Zentrum München, German Research Center for Environmental Health (GmbH), Munich, Germany. ³Physics Division, Department of Radiation Oncology, Massachusetts General Hospital, Boston, MA, USA. ⁴Harvard Medical School, Boston, MA, USA. ⁵Division of Nuclear Medicine and Molecular Imaging, Geneva University Hospital, Geneva, Switzerland. ⁶Institute of Radiation Medicine, Fudan University, Shanghai, China.

Received: 30 May 2021 Accepted: 12 October 2021

Published online: 24 October 2021

References

- Agostinelli S, Allison J, Amako K, Apostolakis J, Araujo H, Arce P, Asai M, Axen D, Banerjee S, Barrand G, Behner F, Belagamba L, Boudreau J, Broglia L, Brunengo A, Burkhardt H, Chauvie S, Chuma J, Chytráček R, Cooperman G, Cosmo G, Degtyarenko P, Dell'Acqua A, Depaola G, Dietrich D, Enami R, Feliciello A, Ferguson C, Fesefeldt H, Folger G, Foppiano F, Forti A, Garelli S, Giani S, Giannitrapani R, Gibin D, Gómez Cadenas JJ, González I, Gracia Abril G, Greeniaus G, Greiner W, Grichine V, Grossheim A, Guatelli S, Gumplinger P, Hamatsu R, Hashimoto K, Hasui H, Heikkinen A, Howard A, Ivanchenko V, Johnson A, Jones FW, Kallenbach J, Kanaya N, Kawabata M, Kawabata Y, Kawaguti M, Kelner S, Kent P, Kimura A, Kodama T, Kokoulin R, Kossow M, Kurashige H, Lamanna E, Lampén T, Lara V, Lefebvre V, Lei F, Liendl M, Lockman W, Longo F, Magni S, Maire M, Medernach E, Minamimoto K, Mora de Freitas P, Morita Y, Murakami K, Nagamatsu M, Nartallo R, Nieminen P, Nishimura T, Ohtsubo K, Okamura M, O'Neale S, Oohata Y, Paech K, Perl J, Pfeiffer A, Pia MG, Ranjard F, Rybin A, Sadilov S, Di Salvo E, Santin G, Sasaki T, Savvas N, Sawada Y et al (2003) Geant4—a simulation toolkit. *Nucl Instrum Methods Phys Res Sect A Accelerators Spectrometers Detect Assoc Equip* 506(3):250–303. [https://doi.org/10.1016/S0168-9002\(03\)01368-8](https://doi.org/10.1016/S0168-9002(03)01368-8)
- Alfonso JCL, Berk L (2019) Modeling the effect of intratumoral heterogeneity of radiosensitivity on tumor response over the course of fractionated radiation therapy. *Radiat Oncol* 14(1):88. <https://doi.org/10.1186/s13014-019-1288-y>
- Allison J, Amako K, Apostolakis J, Arce P, Asai M, Aso T, Bagli E, Bagulya A, Banerjee S, Barrand G, Beck BR, Bogdanov AG, Brandt D, Brown JMC, Burkhardt H, Canal P, Cano-Ott D, Chauvie S, Cho K, Cirrone GAP, Cooperman G, Cortés-Giraldo MA, Cosmo G, Cuttone G, Depaola G, Desorgher L, Dong X, Dotti A, Elvira VD, Folger G, Francis Z, Galoyan A, Garnier L, Gayer M, Genser KL, Grichine VM, Guatelli S, Guéye P, Gumplinger P, Howard AS, Hřivnáčová I, Hwang S, Incerti S, Ivanchenko A, Ivanchenko VN, Jones FW, Jun SY, Kaitaniemi P, Karakatsanis N, Karamitros M, Kelsey M, Kimura A, Koi T, Kurashige H, Lechner A, Lee SB, Longo F, Maire M, Mancusi D, Mantero A, Mendoza E, Morgan B, Murakami K, Nikitina T, Pandola L, Paprocki P, Perl J, Petrović I, Pia MG, Pokorski W, Quesada JM, Raine M, Reis MA, Ribon A, Ristić Fira A, Romano F, Russo G, Santin G, Sasaki T, Sawkey D, Shin Ji, Strakovsky II, Taborda A, Tanaka S, Tomé B, Toshiro T, Tran HN, Truscott PR, Urban L, Uzhinsky V, Verbeke JM, Verderi M, Wendt BL, Wenzel H, Wright DH, Wright DM, Yamashita T, Yarba J, Yoshida H (2016) Recent developments in geant4. *Nucl Instrum Methods Phys Res Sect A Accelerators Spectrometers Detect Assoc Equip* 835:186–225. <https://doi.org/10.1016/j.nima.2016.06.125>
- Balasubramanian B, Pogozelski WK, Tullius TD (1998) Dna strand breaking by the hydroxyl radical is governed by the accessible surface areas of the hydrogen atoms of the DNA backbone. *Proc Natl Acad Sci U S A* 95(17):9738–43. <https://doi.org/10.1073/pnas.95.17.9738>
- Chen G, Roy I, Yang C, Prasad PN (2016) Nanochemistry and nanomedicine for nanoparticle-based diagnostics and therapy. *Chem Rev* 116(5):2826–85. <https://doi.org/10.1021/acs.chemrev.5b00148>
- Cheng NN, Starkewolf Z, Davidson RA, Sharmah A, Lee C, Lien J, Guo T (2012) Chemical enhancement by nanomaterials under x-ray irradiation. *J Am Chem Soc* 134(4):1950–3. <https://doi.org/10.1021/ja210239k>
- Dagogo-Jack I, Shaw AT (2018) Tumour heterogeneity and resistance to cancer therapies. *Nat Rev Clin Oncol* 15(2):81–94. <https://doi.org/10.1038/nrclinonc.2017.166>
- Dai Y, Xu C, Sun X, Chen X (2017) Nanoparticle design strategies for enhanced anticancer therapy by exploiting the tumour microenvironment. *Chem Soc Rev* 46(12):3830–3852. <https://doi.org/10.1039/c6cs00592f>

- Foulkes WD, Smith IE, Reis-Filho JS (2010) Triple-negative breast cancer. *N Engl J Med* 363(20):1938–48. <https://doi.org/10.1056/NEJMra1001389>
- Haume K, de Vera P, Verkhovtsev A, Surdutovich E, Mason NJ, Solovyov AV (2018) Transport of secondary electrons through coatings of ion-irradiated metallic nanoparticles. *Eur Phys J D* 72(6):116. <https://doi.org/10.1140/epjld/e2018-90050-x>
- Incerti S, Kyriakou I, Bernal MA, Bordage MC, Francis Z, Guatelli S, Ivanchenko V, Karamitros M, Lampe N, Lee SB, Meylan S, Min CH, Shin WG, Nieminen P, Sakata D, Tang N, Villagrasa C, Tran HN, Brown JMC (2018) Geant4-dna example applications for track structure simulations in liquid water: a report from the geant4-DNA project. *Med Phys*. <https://doi.org/10.1002/mp.13048>
- Kang MS, Lee SY, Kim KS, Han DW (2020) State of the art biocompatible gold nanoparticles for cancer theragnosis. *Pharmaceutics*. <https://doi.org/10.3390/pharmaceutics12080701>
- Karamitros M, Luan S, Bernal MA, Allison J, Baldacchino G, Davidkova M, Francis Z, Friedland W, Ivantchenko V, Ivantchenko A, Mantero A, Nieminen P, Santin G, Tran HN, Stepan V, Incerti S (2014) Diffusion-controlled reactions modeling in geant4-dna. *J Comput Phys* 274:841–882. <https://doi.org/10.1016/j.jcp.2014.06.011>
- Kraft G, Scholz M, Bechtold U (1999) Tumor therapy and track structure. *Radiat Environ Biophys* 38(4):229–37. <https://doi.org/10.1007/s004110050163>
- Kuncic Z, Lacombe S (2018) Nanoparticle radio-enhancement: principles, progress and application to cancer treatment. *Phys Med Biol* 63(2):02–01. <https://doi.org/10.1088/1361-6560/aa99ce>
- Lampe N, Karamitros M, Breton V, Brown JMC, Kyriakou I, Sakata D, Sarramia D, Incerti S (2018) Mechanistic dna damage simulations in geant4-dna part 1: a parameter study in a simplified geometry. *Phys Med* 48:135–145. <https://doi.org/10.1016/j.ejmp.2018.02.011>
- Lechtman E, Pignol JP (2017) Interplay between the gold nanoparticle sub-cellular localization, size, and the photon energy for radiosensitization. *Sci Rep* 7(1):13268. <https://doi.org/10.1038/s41598-017-13736-y>
- Li W, Müllner M, Greiter M, Bissardon C, Xie W, Schlattl H, Oeh U, Li J, Hoeschen C (2014) Monte Carlo simulations of dose enhancement around gold nanoparticles used as X-ray imaging contrast agents and radiosensitizers. In: *SPIE medical imaging*, vol. 9033, p. 90331. SPIE, Bellingham <https://doi.org/10.1117/12.2043687>
- Li WB, Belchior A, Beuve M, Chen YZ, Di Maria S, Friedland W, Gervais B, Heide B, Hocine N, Ipatov A, Klapproth AP, Li CY, Li JL, Multhoff G, Poignant F, Qiu R, Rabus H, Rudek B, Schuemann J, Stangl S, Testa E, Villagrasa C, Xie WZ, Zhang YB (2020) Intercomparison of dose enhancement ratio and secondary electron spectra for gold nanoparticles irradiated by x-rays calculated using multiple monte carlo simulation codes. *Phys Med* 69:147–163. <https://doi.org/10.1016/j.ejmp.2019.12.011>
- Lieberman-Aiden E, van Berkum NL, Williams L, Imakaev M, Ragoczy T, Telling A, Amit I, Lajoie BR, Sabo PJ, Dorschner MO, Sandstrom R, Bernstein B, Bender MA, Groudine M, Gnirke A, Stamatoyannopoulos J, Mirny LA, Lander ES, Dekker J (2009) Comprehensive mapping of long-range interactions reveals folding principles of the human genome. *Science* 326(5950):289–93. <https://doi.org/10.1126/science.1181369>
- Lin Y, McMahon SJ, Scarpelli M, Paganetti H, Schuemann J (2014) Comparing gold nano-particle enhanced radiotherapy with protons, megavoltage photons and kilovoltage photons: a monte carlo simulation. *Phys Med Biol* 59(24):7675–89. <https://doi.org/10.1088/0031-9155/59/24/7675>
- Liu R, Wang Y, Yuan Q, An D, Li J, Gao X (2014) The au clusters induce tumor cell apoptosis via specifically targeting thioredoxin reductase 1 (trxr1) and suppressing its activity. *Chem Commun (Camb)* 50(73):10687–90. <https://doi.org/10.1039/c4cc03320e>
- Marusyk A, Polyak K (2010) Tumor heterogeneity: causes and consequences. *Biochim Biophys Acta* 1805(1):105–17. <https://doi.org/10.1016/j.bbcan.2009.11.002>
- McMahon SJ, Hyland WB, Muir MF, Coulter JA, Jain S, Butterworth KT, Schettino G, Dickson GR, Hounsell AR, O'Sullivan JM, Prise KM, Hirst DG, Currell FJ (2011) Nanodosimetric effects of gold nanoparticles in megavoltage radiation therapy. *Radiother Oncol* 100(3):412–6. <https://doi.org/10.1016/j.radonc.2011.08.026>
- McNamara AL, Ramos-Mendez J, Perl J, Held K, Dominguez N, Moreno E, Henthorn NT, Kirkby KJ, Meylan S, Villagrasa C, Incerti S, Faddegon B, Paganetti H, Schuemann J (2018) Geometrical structures for radiation biology research as implemented in the topas-nbio toolkit. *Phys Med Biol* 63(17):175018. <https://doi.org/10.1088/1361-6560/aad8eb>
- Meylan S, Incerti S, Karamitros M, Tang N, Bueno M, Clairand I, Villagrasa C (2017) Simulation of early dna damage after the irradiation of a fibroblast cell nucleus using geant4-dna. *Sci Rep* 7(1):11923. <https://doi.org/10.1038/s41598-017-11851-4>
- Oelze ML, O'Brien JWD, Blue JP, Zachary JF (2004) Differentiation and characterization of rat mammary fibroadenomas and 4t1 mouse carcinomas using quantitative ultrasound imaging. *IEEE Trans Med Imaging* 23(6):764–71. <https://doi.org/10.1109/tmi.2004.826953>
- Pan Y, Leifert A, Ruau D, Neuss S, Bornemann J, Schmid G, Brandau W, Simon U, Jahnhen-Dechent W (2009) Gold nanoparticles of diameter 1.4 nm trigger necrosis by oxidative stress and mitochondrial damage. *Small* 5(18):2067–76. <https://doi.org/10.1002/sml.200900466>
- Perl J, Shin J, Schumann J, Faddegon B, Paganetti H (2012) Topas: an innovative proton monte carlo platform for research and clinical applications. *Med Phys* 39(11):6818–37. <https://doi.org/10.1118/1.4758060>
- Physics Lists EM constructors in Geant4 10.4 (2021) <https://geant4.web.cern.ch/node/1731>
- Poludniowski G, Landry G, Deblois F, Evans PM, Verhaegen F (2009) Spekcalc: a program to calculate photon spectra from tungsten anode x-ray tubes. *Phys Med Biol* 54(19):433–438. <https://doi.org/10.1088/0031-9155/54/19/N01>
- Pulaski BA, Ostrand-Rosenberg S (2001) Mouse 4t1 breast tumor model. *Curr Protoc Immunol Chapter* 20:20–2. <https://doi.org/10.1002/0471142735.im2002s39>
- Rabus H, Gargioni E, Li WB, Nettelbeck H, Villagrasa C (2019) Determining dose enhancement factors of high-z nanoparticles from simulations where lateral secondary particle disequilibrium exists. *Phys Med Biol* 64(15):155016. <https://doi.org/10.1088/1361-6560/ab31d4>
- Ramos-Mendez J, Perl J, Schuemann J, McNamara A, Paganetti H, Faddegon B (2018) Monte carlo simulation of chemistry following radiolysis with topas-nbio. *Phys Med Biol* 63(10):105014. <https://doi.org/10.1088/1361-6560/aac04c>

- Rosa S, Connolly C, Schettino G, Butterworth KT, Prise KM (2017) Biological mechanisms of gold nanoparticle radiosensitization. *Cancer Nanotechnol* 8(1):2. <https://doi.org/10.1186/s12645-017-0026-0>
- Rudek B, McNamara A, Ramos-Mendez J, Byrne H, Kuncic Z, Schuemann J (2019) Radio-enhancement by gold nanoparticles and their impact on water radiolysis for x-ray, proton and carbon-ion beams. *Phys Med Biol* 64(17):175005. <https://doi.org/10.1088/1361-6560/ab314c>
- Sakata D, Kyriakou I, Okada S, Tran HN, Lampe N, Guatelli S, Bordage MC, Ivanchenko V, Murakami K, Sasaki T, Emfietzoglou D, Incerti S (2018) Geant4-DNA track-structure simulations for gold nanoparticles: the importance of electron discrete models in nanometer volumes. *Med Phys* 45(5):2230–2242. <https://doi.org/10.1002/mp.12827>
- Sakata D, Lampe N, Karamitros M, Kyriakou I, Belov O, Bernal MA, Bolst D, Bordage MC, Breton V, Brown JMC, Francis Z, Ivanchenko V, Meylan S, Murakami K, Okada S, Petrovic I, Ristic-Fira A, Santin G, Sarramia D, Sasaki T, Shin WG, Tang N, Tran HN, Villagrana C, Emfietzoglou D, Nieminen P, Guatelli S, Incerti S (2019) Evaluation of early radiation DNA damage in a fractal cell nucleus model using geant4-DNA. *Phys Med* 62:152–157. <https://doi.org/10.1016/j.jeimp.2019.04.010>
- Schuemann J, Berbeco R, Chithrani DB, Cho SH, Kumar R, McMahon SJ, Sridhar S, Krishnan S (2016) Roadmap to clinical use of gold nanoparticles for radiation sensitization. *Int J Radiat Oncol Biol Phys* 94(1):189–205. <https://doi.org/10.1016/j.ijrobp.2015.09.032>
- Schuemann J, McNamara AL, Ramos-Mendez J, Perl J, Held KD, Paganetti H, Incerti S, Faddegon B (2019a) Topas-nbio: an extension to the topas simulation toolkit for cellular and sub-cellular radiobiology. *Radiat Res* 191(2):125–138. <https://doi.org/10.1667/RR15226.1>
- Schuemann J, McNamara AL, Warmenhoven JW, Henthorn NT, Kirkby KJ, Merchant MJ, Ingram S, Paganetti H, Held KD, Ramos-Mendez J, Faddegon B, Perl J, Goodhead DT, Plante I, Rabus H, Nettelbeck H, Friedland W, Kundrat P, Ottolenghi A, Baiocco G, Barbieri S, Dingfelder M, Incerti S, Villagrana C, Bueno M, Bernal MA, Guatelli S, Sakata D, Brown JMC, Francis Z, Kyriakou I, Lampe N, Ballarini F, Carante MP, Davidkova M, Stepan V, Jia X, Cucinotta FA, Schulte R, Stewart RD, Carlson DJ, Galer S, Kuncic Z, Lacombe S, Milligan J, Cho SH, Sawakuchi G, Inaniwa T, Sato T, Li W, Solov'ov AV, Surdutovich E, Durante M, Prise KM, McMahon SJ (2019b) A new standard dna damage (sdd) data format. *Radiat Res* 191(1):76–92. <https://doi.org/10.1667/RR15209.1>
- Seo SJ, Jeon JK, Han SM, Kim JK (2017) Reactive oxygen species-based measurement of the dependence of the coulomb nanoradiator effect on proton energy and atomic z value. *Int J Radiat Biol* 93(11):1239–1247. <https://doi.org/10.1080/09553002.2017.1361556>
- Sicard-Roselli C, Brun E, Gilles M, Baldacchino G, Kelsey C, McQuaid H, Polin C, Wardlow N, Currell F (2014) A new mechanism for hydroxyl radical production in irradiated nanoparticle solutions. *Small* 10(16):3338–46. <https://doi.org/10.1002/sml.201400110>
- Smialek MA, Jones NC, Hoffmann SV, Mason NJ (2013) Measuring the density of dna films using ultraviolet-visible interferometry. *Phys Rev E Stat Nonlin Soft Matter Phys* 87(6):060701. <https://doi.org/10.1103/PhysRevE.87.060701>
- Sung W, Schuemann J (2018) Energy optimization in gold nanoparticle enhanced radiation therapy. *Phys Med Biol* 63(13):135001. <https://doi.org/10.1088/1361-6560/aacab6>
- Sung W, Jung S, Ye SJ (2016) Evaluation of the microscopic dose enhancement for nanoparticle-enhanced auger therapy. *Phys Med Biol* 61(21):7522–7535. <https://doi.org/10.1088/0031-9155/61/21/7522>
- Sung W, Ye SJ, McNamara AL, McMahon SJ, Hainfeld J, Shin J, Smilowitz HM, Paganetti H, Schuemann J (2017) Dependence of gold nanoparticle radiosensitization on cell geometry. *Nanoscale* 9(18):5843–5853. <https://doi.org/10.1039/c7nr01024a>
- Takai K, Le A, Weaver VM, Werb Z (2016) Targeting the cancer-associated fibroblasts as a treatment in triple-negative breast cancer. *Oncotarget* 7(50):82889–82901. <https://doi.org/10.18632/oncotarget.12658>
- Thomson RM, Kawrakow I (2011) On the monte carlo simulation of electron transport in the sub-1 keV energy range. *Med Phys* 38(8):4531–4. <https://doi.org/10.1118/1.3608904>
- Wong J, Armour E, Kazanzides P, Iordachita I, Tryggstad E, Deng H, Matinfar M, Kennedy C, Liu Z, Chan T, Gray O, Verhaegen F, McNutt T, Ford E, DeWeese TL (2008) High-resolution, small animal radiation research platform with x-ray tomographic guidance capabilities. *Int J Radiat Oncol Biol Phys* 71(5):1591–1599. <https://doi.org/10.1016/j.ijrobp.2008.04.025>
- Xiao F, Zheng Y, Cloutier P, He Y, Hunting D, Sanche L (2011) On the role of low-energy electrons in the radiosensitization of DNA by gold nanoparticles. *Nanotechnology* 22(46):465101. <https://doi.org/10.1088/0957-4484/22/46/465101>
- Xie T, Zaidi H (2013) Monte carlo-based evaluation of s-values in mouse models for positron-emitting radionuclides. *Phys Med Biol* 58(1):169–82. <https://doi.org/10.1088/0031-9155/58/1/169>
- Xie WZ, Friedland W, Li WB, Li CY, Oeh U, Qiu R, Li JL, Hoeschen C (2015) Simulation on the molecular radiosensitization effect of gold nanoparticles in cells irradiated by x-rays. *Phys Med Biol* 60(16):6195–212. <https://doi.org/10.1088/0031-9155/60/16/6195>
- Xin Y, Yin M, Zhao L, Meng F, Luo L (2017) Recent progress on nanoparticle-based drug delivery systems for cancer therapy. *Cancer Biol Med* 14(3):228–241. <https://doi.org/10.20892/j.issn.2095-3941.2017.0052>
- Zhivotovskiy B, Joseph B, Orrenius S (1999) Tumor radiosensitivity and apoptosis. *Exp Cell Res* 248(1):10–7. <https://doi.org/10.1006/excr.1999.4452>
- Zhu H, McNamara AL, McMahon SJ, Ramos-Mendez J, Henthorn NT, Faddegon B, Held KD, Perl J, Li J, Paganetti H, Schuemann J (2020a) Cellular response to proton irradiation: a simulation study with topas-nbio. *Radiat Res* 194(1):9–21. <https://doi.org/10.1667/RR15531.1>
- Zhu H, McNamara AL, Ramos-Mendez J, McMahon SJ, Henthorn NT, Faddegon B, Held KD, Perl J, Li J, Paganetti H, Schuemann J (2020b) A parameter sensitivity study for simulating DNA damage after proton irradiation using topas-nbio. *Phys Med Biol* 65(8):085015. <https://doi.org/10.1088/1361-6560/ab7a6b>

Publisher's Note

Springer Nature remains neutral with regard to jurisdictional claims in published maps and institutional affiliations.

A.3.2. Supplementary information

Multi-scale Monte Carlo simulations of gold nanoparticle induced DNA damages for kilovoltage x-ray irradiation in a xenograft mouse model using TOPAS-nBio

Alexander P. Klapproth ^{1,2,*}, Jan Schuemann ^{3-4,*}, Stefan Stangl ¹,
Tianwu Xie ^{5,6}, Wei Bo Li ^{2,*} and Gabriele Multhoff ¹

¹ Center for Translational Cancer Research Technische Universität München (TranslaTUM), Klinikum Rechts der Isar, Munich, Germany

² Institute of Radiation Medicine, Helmholtz Zentrum München, German Research Center for Environmental Health (GmbH), Munich, Germany

³ Physics Division, Department of Radiation Oncology, Massachusetts General Hospital, Boston, MA, United States of America

⁴ Harvard Medical School, Boston, MA, United States of America

⁵ Division of Nuclear Medicine and Molecular Imaging, Geneva University Hospital, Geneva, Switzerland

⁶ Institute of Radiation Medicine, Fudan University, Shanghai, China

Table S1: Simulation results and standard deviations - 100 kVp, front cell, without AuFeNPs

	Overall Value	SD
Total SB	764	$1.08 \cdot 10^{-2}$
Total SB direct	310	$6.879 \cdot 10^{-3}$
Total SB indirect	454	$8.324 \cdot 10^{-3}$
Total SSB	484	$8.595 \cdot 10^{-3}$
Total SSB direct	207	$5.621 \cdot 10^{-3}$
Total SSB indirect	277	$6.502 \cdot 10^{-3}$
Total DSB	140	$4.623 \cdot 10^{-3}$
Total DSB direct	22	$1.833 \cdot 10^{-3}$
Total DSB indirect	59	$3.001 \cdot 10^{-3}$
Total DSB hybrid	59	$3.001 \cdot 10^{-3}$
Dose (Gy)	0.845037	$0.359 \cdot 10^{-3}$
H radicals	28874	$6.624 \cdot 10^{-2}$
OH radicals	62214	$9.699 \cdot 10^{-2}$
H ₂ radicals	12275	$4.325 \cdot 10^{-2}$
H ₂ O ₂ radicals	92414	$1.179 \cdot 10^{-1}$
H ₃ O radicals	7023	$3.272 \cdot 10^{-2}$
e _{aq} radicals	27	$2.03 \cdot 10^{-3}$

Table S2: Simulation results and standard deviations - 100 kVp, front cell, with AuFeNPs

	Overall Value	SD
Total SB	811	$1.113 \cdot 10^{-2}$
Total SB direct	314	$6.923 \cdot 10^{-3}$
Total SB indirect	497	$8.71 \cdot 10^{-3}$
Total SSB	467	$8.443 \cdot 10^{-3}$
Total SSB direct	176	$5.183 \cdot 10^{-3}$
Total SSB indirect	291	$6.665 \cdot 10^{-3}$
Total DSB	172	$5.124 \cdot 10^{-3}$
Total DSB direct	28	$2.067 \cdot 10^{-3}$
Total DSB indirect	62	$3.076 \cdot 10^{-3}$
Total DSB hybrid	82	$3.538 \cdot 10^{-3}$
Dose (Gy)	0.885086	$0.368 \cdot 10^{-3}$
H radicals	46632	$8.407 \cdot 10^{-2}$
OH radicals	134708	$1.419 \cdot 10^{-1}$
H ₂ radicals	34173	$7.204 \cdot 10^{-2}$
H ₂ O ₂ radicals	98057	$1.214 \cdot 10^{-1}$
H ₃ O radicals	2069	$1.777 \cdot 10^{-2}$
e _{aq} radicals	16	$1.563 \cdot 10^{-3}$

Table S3: Simulation results and standard deviations - 100 kVp, center cell, without AuFeNPs

	Overall Value	SD
Total SB	722	$1.066 \cdot 10^{-2}$
Total SB direct	276	$6.594 \cdot 10^{-3}$
Total SB indirect	446	$8.382 \cdot 10^{-3}$
Total SSB	480	$8.695 \cdot 10^{-3}$
Total SSB direct	185	$5.398 \cdot 10^{-3}$
Total SSB indirect	295	$6.817 \cdot 10^{-3}$
Total DSB	121	$4.366 \cdot 10^{-3}$
Total DSB direct	23	$1.903 \cdot 10^{-3}$
Total DSB indirect	53	$2.889 \cdot 10^{-3}$
Total DSB hybrid	45	$2.662 \cdot 10^{-3}$
Dose (Gy)	0.831712	$0.362 \cdot 10^{-3}$
H radicals	28921	$6.734 \cdot 10^{-2}$
OH radicals	62100	$9.842 \cdot 10^{-2}$
H ₂ radicals	12039	$4.351 \cdot 10^{-2}$
H ₂ O ₂ radicals	92726	$1.2 \cdot 10^{-1}$
H ₃ O radicals	7170	$3.359 \cdot 10^{-2}$
e _{aq} radicals	30	$2.174 \cdot 10^{-3}$

Table S4: Simulation results and standard deviations - 100 kVp, center cell, with AuFeNPs

	Overall Value	SD
Total SB	773	$1.103 \cdot 10^{-2}$
Total SB direct	262	$6.424 \cdot 10^{-3}$
Total SB indirect	511	$8.972 \cdot 10^{-3}$
Total SSB	459	$8.503 \cdot 10^{-3}$
Total SSB direct	162	$5.052 \cdot 10^{-3}$
Total SSB indirect	297	$6.84 \cdot 10^{-3}$
Total DSB	157	$4.973 \cdot 10^{-3}$
Total DSB direct	18	$1.684 \cdot 10^{-3}$
Total DSB indirect	75	$3.437 \cdot 10^{-3}$
Total DSB hybrid	64	$3.175 \cdot 10^{-3}$
Dose (Gy)	0.896441	$0.376 \cdot 10^{-3}$
H radicals	47563	$8.623 \cdot 10^{-2}$
OH radicals	138590	$1.461 \cdot 10^{-1}$
H ₂ radicals	35443	$7.451 \cdot 10^{-2}$
H ₂ O ₂ radicals	101424	$1.254 \cdot 10^{-1}$
H ₃ O radicals	1925	$1.741 \cdot 10^{-2}$
e _{aq} radicals	14	$1.485 \cdot 10^{-3}$

Table S5: Simulation results and standard deviations - 100 kVp, back cell, without AuFeNPs

	Overall Value	SD
Total SB	720	$1.079 \cdot 10^{-2}$
Total SB direct	286	$6.798 \cdot 10^{-3}$
Total SB indirect	434	$8.375 \cdot 10^{-3}$
Total SSB	436	$8.394 \cdot 10^{-3}$
Total SSB direct	192	$5.57 \cdot 10^{-3}$
Total SSB indirect	244	$6.28 \cdot 10^{-3}$
Total DSB	142	$4.79 \cdot 10^{-3}$
Total DSB direct	19	$1.752 \cdot 10^{-3}$
Total DSB indirect	67	$3.291 \cdot 10^{-3}$
Total DSB hybrid	56	$3.008 \cdot 10^{-3}$
Dose (Gy)	0.782187	$0.356 \cdot 10^{-3}$
H radicals	28936	$6.822 \cdot 10^{-2}$
OH radicals	61681	$9.934 \cdot 10^{-2}$
H ₂ radicals	11917	$4.384 \cdot 10^{-2}$
H ₂ O ₂ radicals	88797	$1.189 \cdot 10^{-1}$
H ₃ O radicals	7362	$3.447 \cdot 10^{-2}$
e _{aq} radicals	38	$2.478 \cdot 10^{-3}$

Table S6: Simulation results and standard deviations - 100 kVp, back cell, with AuFeNPs

	Overall Value	SD
Total SB	772	$1.117 \cdot 10^{-2}$
Total SB direct	308	$7.055 \cdot 10^{-3}$
Total SB indirect	464	$8.659 \cdot 10^{-3}$
Total SSB	478	$8.789 \cdot 10^{-3}$
Total SSB direct	192	$5.57 \cdot 10^{-3}$
Total SSB indirect	286	$6.798 \cdot 10^{-3}$
Total DSB	147	$4.874 \cdot 10^{-3}$
Total DSB direct	19	$1.752 \cdot 10^{-3}$
Total DSB indirect	50	$2.843 \cdot 10^{-3}$
Total DSB hybrid	78	$3.55 \cdot 10^{-3}$
Dose (Gy)	0.848231	$0.37 \cdot 10^{-3}$
H radicals	46075	$8.597 \cdot 10^{-2}$
OH radicals	135352	$1.463 \cdot 10^{-1}$
H ₂ radicals	34480	$7.444 \cdot 10^{-2}$
H ₂ O ₂ radicals	95191	$1.231 \cdot 10^{-1}$
H ₃ O radicals	2251	$1.907 \cdot 10^{-2}$
e _{aq} radicals	21	$1.842 \cdot 10^{-3}$

Table S7: Simulation results and standard deviations - 200 kVp, front cell, without AuFeNPs

	Overall Value	SD
Total SB	756	$10.801 \cdot 10^{-3}$
Total SB direct	274	$6.503 \cdot 10^{-3}$
Total SB indirect	482	$8.625 \cdot 10^{-3}$
Total SSB	474	$8.553 \cdot 10^{-3}$
Total SSB direct	179	$5.256 \cdot 10^{-3}$
Total SSB indirect	295	$6.747 \cdot 10^{-3}$
Total DSB	141	$4.665 \cdot 10^{-3}$
Total DSB direct	18	$1.667 \cdot 10^{-3}$
Total DSB indirect	64	$3.143 \cdot 10^{-3}$
Total DSB hybrid	59	$3.018 \cdot 10^{-3}$
Dose (Gy)	0.918982	$0.377 \cdot 10^{-3}$
H radicals	40523	$7.883 \cdot 10^{-2}$
OH radicals	85989	$1.144 \cdot 10^{-1}$
H ₂ radicals	16641	$5.061 \cdot 10^{-2}$
H ₂ O ₂ radicals	127663	$1.39 \cdot 10^{-1}$
H ₃ O radicals	9861	$3.898 \cdot 10^{-2}$
e _{aq} radicals	26	$2.003 \cdot 10^{-3}$

Table S8: Simulation results and standard deviations - 200 kVp, front cell, with AuFeNPs

	Overall Value	SD
Total SB	886	$11.693 \cdot 10^{-3}$
Total SB direct	334	$7.179 \cdot 10^{-3}$
Total SB indirect	552	$9.23 \cdot 10^{-3}$
Total SSB	550	$9.213 \cdot 10^{-3}$
Total SSB direct	205	$5.625 \cdot 10^{-3}$
Total SSB indirect	345	$7.297 \cdot 10^{-3}$
Total DSB	168	$5.092 \cdot 10^{-3}$
Total DSB direct	28	$2.079 \cdot 10^{-3}$
Total DSB indirect	67	$3.216 \cdot 10^{-3}$
Total DSB hybrid	73	$3.357 \cdot 10^{-3}$
Dose (Gy)	1.07826	$0.408 \cdot 10^{-3}$
H radicals	61030	$9.659 \cdot 10^{-2}$
OH radicals	176515	$1.628 \cdot 10^{-1}$
H ₂ radicals	44755	$8.282 \cdot 10^{-2}$
H ₂ O ₂ radicals	131031	$1.408 \cdot 10^{-1}$
H ₃ O radicals	2272	$1.872 \cdot 10^{-2}$
e _{aq} radicals	11	$1.303 \cdot 10^{-3}$

Table S9: Simulation results and standard deviations - 200 kVp, center cell, without AuFeNPs

	Overall Value	SD
Total SB	658	$10.159 \cdot 10^{-3}$
Total SB direct	230	$6.007 \cdot 10^{-3}$
Total SB indirect	428	$8.194 \cdot 10^{-3}$
Total SSB	380	$7.721 \cdot 10^{-3}$
Total SSB direct	147	$4.802 \cdot 10^{-3}$
Total SSB indirect	233	$6.046 \cdot 10^{-3}$
Total DSB	139	$4.67 \cdot 10^{-3}$
Total DSB direct	17	$1.633 \cdot 10^{-3}$
Total DSB indirect	73	$3.384 \cdot 10^{-3}$
Total DSB hybrid	49	$2.772 \cdot 10^{-3}$
Dose (Gy)	0.773754	$0.348 \cdot 10^{-3}$
H radicals	32259	$7.096 \cdot 10^{-2}$
OH radicals	68981	$1.035 \cdot 10^{-1}$
H ₂ radicals	13549	$4.605 \cdot 10^{-2}$
H ₂ O ₂ radicals	107197	$1.286 \cdot 10^{-1}$
H ₃ O radicals	7300	$3.382 \cdot 10^{-2}$
e _{aq} radicals	16	$1.584 \cdot 10^{-3}$

Table S10: Simulation results and standard deviations - 200 kVp, center cell, with AuFeNPs

	Overall Value	SD
Total SB	701	$10.486 \cdot 10^{-3}$
Total SB direct	256	$6.337 \cdot 10^{-3}$
Total SB indirect	445	$8.355 \cdot 10^{-3}$
Total SSB	413	$8.049 \cdot 10^{-3}$
Total SSB direct	153	$4.899 \cdot 10^{-3}$
Total SSB indirect	260	$6.386 \cdot 10^{-3}$
Total DSB	144	$4.753 \cdot 10^{-3}$
Total DSB direct	20	$1.771 \cdot 10^{-3}$
Total DSB indirect	61	$3.093 \cdot 10^{-3}$
Total DSB hybrid	63	$3.144 \cdot 10^{-3}$
Dose (Gy)	0.80812	$0.356 \cdot 10^{-3}$
H radicals	51718	$8.971 \cdot 10^{-2}$
OH radicals	150070	$1.516 \cdot 10^{-1}$
H ₂ radicals	38213	$7.719 \cdot 10^{-2}$
H ₂ O ₂ radicals	112756	$1.318 \cdot 10^{-1}$
H ₃ O radicals	2209	$1.861 \cdot 10^{-2}$
e _{aq} radicals	6	$0.97 \cdot 10^{-3}$

Table S11: Simulation results and standard deviations - 200 kVp, back cell, without AuFeNPs

	Overall Value	SD
Total SB	557	$9.478 \cdot 10^{-3}$
Total SB direct	228	$6.064 \cdot 10^{-3}$
Total SB indirect	329	$7.284 \cdot 10^{-3}$
Total SSB	331	$7.306 \cdot 10^{-3}$
Total SSB direct	144	$4.819 \cdot 10^{-3}$
Total SSB indirect	187	$5.492 \cdot 10^{-3}$
Total DSB	113	$4.269 \cdot 10^{-3}$
Total DSB direct	20	$1.796 \cdot 10^{-3}$
Total DSB indirect	49	$2.811 \cdot 10^{-3}$
Total DSB hybrid	44	$2.664 \cdot 10^{-3}$
Dose (Gy)	0.631707	$0.319 \cdot 10^{-3}$
H radicals	27139	$6.601 \cdot 10^{-2}$
OH radicals	58021	$9.628 \cdot 10^{-2}$
H ₂ radicals	11216	$4.249 \cdot 10^{-2}$
H ₂ O ₂ radicals	84361	$1.158 \cdot 10^{-1}$
H ₃ O radicals	6746	$3.297 \cdot 10^{-2}$
e _{aq} radicals	24	$1.967 \cdot 10^{-3}$

Table S12: Simulation results and standard deviations - 200 kVp, back cell, with AuFeNPs

	Overall Value	SD
Total SB	594	$9.787 \cdot 10^{-3}$
Total SB direct	207	$5.778 \cdot 10^{-3}$
Total SB indirect	387	$7.9 \cdot 10^{-3}$
Total SSB	372	$7.746 \cdot 10^{-3}$
Total SSB direct	120	$4.399 \cdot 10^{-3}$
Total SSB indirect	252	$6.375 \cdot 10^{-3}$
Total DSB	111	$4.231 \cdot 10^{-3}$
Total DSB direct	22	$1.884 \cdot 10^{-3}$
Total DSB indirect	46	$2.724 \cdot 10^{-3}$
Total DSB hybrid	43	$2.633 \cdot 10^{-3}$
Dose (Gy)	0.709614	$0.338 \cdot 10^{-3}$
H radicals	43150	$8.313 \cdot 10^{-2}$
OH radicals	122708	$1.393 \cdot 10^{-1}$
H ₂ radicals	30881	$7.04 \cdot 10^{-2}$
H ₂ O ₂ radicals	89501	$1.193 \cdot 10^{-1}$
H ₃ O radicals	2330	$1.938 \cdot 10^{-2}$
e _{aq} radicals	12	$1.391 \cdot 10^{-3}$

List of Figures

1.	PBPK model structure	14
2.	DER in nanometer range calculated by simulations with a single AuNP	19
3.	DER in micrometer range calculated by simulations with a single AuNP	20
4.	Sketch of the voxel model simulations	22
5.	X-ray photon spectra	23
6.	Visualization of the randomization modes for particles in the (mouse model → tumor) phase space	25
7.	Sketch of the Tumor simulations	26
8.	Sketch of the Cell simulations	27
9.	Voxelized nucleus model	33
10.	TOPAS visualization depicting voxel structure	34

List of Tables

1. Flags and materials in the mouse model simulations 21
2. Number of voxels and base pairs per chromosome 32

Bibliography

- [1] A. P. Klapproth, M. Shevtsov, S. Stangl, W. B. Li, and G. Multhoff, “A new pharmacokinetic model describing the biodistribution of intravenously and intratumorally administered superparamagnetic iron oxide nanoparticles (spions) in a gl261 xenograft glioblastoma model,” *Int J Nanomedicine*, vol. 15, pp. 4677–4689, 2020. [Online]. Available: <https://www.ncbi.nlm.nih.gov/pubmed/32669844>
- [2] —, “Erratum: A new pharmacokinetic model describing the biodistribution of intravenously and intratumorally administered superparamagnetic iron oxide nanoparticles (spions) in a gl261 xenograft glioblastoma model [corrigendum],” *Int J Nanomedicine*, vol. 15, p. 6067, aug 2020. [Online]. Available: <https://www.ncbi.nlm.nih.gov/pubmed/32884262>
- [3] A. P. Klapproth, J. Schuemann, S. Stangl, T. Xie, W. B. Li, and G. Multhoff, “Multi-scale monte carlo simulations of gold nanoparticle-induced dna damages for kilovoltage x-ray irradiation in a xenograft mouse model using topas-nbio,” *Cancer Nanotechnology*, vol. 12, no. 1, p. 27, 2021. [Online]. Available: <https://doi.org/10.1186/s12645-021-00099-3>
- [4] W. B. Li, A. Belchior, M. Beuve, Y. Z. Chen, S. Di Maria, W. Friedland, B. Gervais, B. Heide, N. Hocine, A. Ipatov, A. P. Klapproth, C. Y. Li, J. L. Li, G. Multhoff, F. Poignant, R. Qiu, H. Rabus, B. Rudek, J. Schuemann, S. Stangl, E. Testa, C. Villagrasa, W. Z. Xie, and Y. B. Zhang, “Intercomparison of dose enhancement ratio and secondary electron spectra for gold nanoparticles irradiated by x-rays calculated using multiple

- monte carlo simulation codes,” *Phys Med*, vol. 69, pp. 147–163, 2020. [Online]. Available: <https://www.ncbi.nlm.nih.gov/pubmed/31918367>
- [5] W. B. Li, M. Beuve, S. Di Maria, W. Friedland, B. Heide, A. P. Klapproth, C. Y. Li, F. Poignant, H. Rabus, B. Rudek, J. Schuemann, and C. Villagrasa, “Corrigendum to "intercomparison of dose enhancement ratio and secondary electron spectra for gold nanoparticles irradiated by x-rays calculated using multiple monte carlo simulation codes" [phys. med. 69 (2020) 147-163],” *Phys Med*, vol. 80, pp. 383–388, 2020. [Online]. Available: <https://www.ncbi.nlm.nih.gov/pubmed/33203583>
- [6] H. Rabus, W. B. Li, C. Villagrasa, J. Schuemann, P. A. Hepperle, L. de la Fuente Rosales, M. Beuve, S. Di Maria, A. P. Klapproth, C. Y. Li, F. Poignant, B. Rudek, and H. Nettelbeck, “Intercomparison of monte carlo calculated dose enhancement ratios for gold nanoparticles irradiated by x-rays: Assessing the uncertainty and correct methodology for extended beams,” *Phys Med*, vol. 84, pp. 241–253, 2021. [Online]. Available: <https://www.ncbi.nlm.nih.gov/pubmed/33766478>
- [7] N. Yuditceva, N. Mikhailova, D. Bobkov, L. Yakovleva, B. Nikolaev, D. Krasavina, A. Muraviov, T. Vinogradova, P. Yablonskiy, I. Samusenko, V. Ryzhov, V. Deriglazov, Y. Marchenko, G. Multhoff, A. P. Klapproth, W. B. Li, B. Nayak, A. Sonawane, and M. Shevtsov, “Evaluation of the biodistribution of mesenchymal stem cells in a pre-clinical renal tuberculosis model by non-linear magnetic response measurements,” *Frontiers in Physics*, vol. 9, 2021. [Online]. Available: <https://www.frontiersin.org/article/10.3389/fphy.2021.625622>
- [8] H. Rabus, W. B. Li, H. Nettelbeck, J. Schuemann, C. Villagrasa, M. Beuve, S. Di Maria, B. Heide, A. P. Klapproth, F. Poignant, R. Qiu, and B. Rudek, “Consistency checks of results from a monte carlo code intercomparison for emitted electron spectra and energy

- deposition around a single gold nanoparticle irradiated by x-rays,” *Radiation Measurements*, vol. 147, p. 106637, 2021. [Online]. Available: <https://www.sciencedirect.com/science/article/pii/S1350448721001487>
- [9] W. B. Li, S. Stangl, A. Klapproth, M. Shevtsov, A. Hernandez, M. A. Kimm, J. Schuemann, R. Qiu, B. Michalke, M. A. Bernal, J. Li, K. Hurkamp, Y. Zhang, and G. Multhoff, “Application of high-z gold nanoparticles in targeted cancer radiotherapy-pharmacokinetic modeling, monte carlo simulation and radiobiological effect modeling,” *Cancers (Basel)*, vol. 13, no. 21, 2021. [Online]. Available: <https://www.ncbi.nlm.nih.gov/pubmed/34771534>
- [10] Y. Dai, C. Xu, X. Sun, and X. Chen, “Nanoparticle design strategies for enhanced anticancer therapy by exploiting the tumour microenvironment,” *Chem Soc Rev*, vol. 46, no. 12, pp. 3830–3852, 2017. [Online]. Available: <https://www.ncbi.nlm.nih.gov/pubmed/28516983>
- [11] G. Chen, I. Roy, C. Yang, and P. N. Prasad, “Nanochemistry and nanomedicine for nanoparticle-based diagnostics and therapy,” *Chem Rev*, vol. 116, no. 5, pp. 2826–85, 2016. [Online]. Available: <https://www.ncbi.nlm.nih.gov/pubmed/26799741>
- [12] Y. Xin, M. Yin, L. Zhao, F. Meng, and L. Luo, “Recent progress on nanoparticle-based drug delivery systems for cancer therapy,” *Cancer Biol Med*, vol. 14, no. 3, pp. 228–241, 2017. [Online]. Available: <https://www.ncbi.nlm.nih.gov/pubmed/28884040>
- [13] H. Maeda, “Tumor-selective delivery of macromolecular drugs via the epr effect: background and future prospects,” *Bioconjug Chem*, vol. 21, no. 5, pp. 797–802, 2010. [Online]. Available: <https://www.ncbi.nlm.nih.gov/pubmed/20397686>
- [14] H. Maeda, K. Tsukigawa, and J. Fang, “A retrospective 30 years after discovery of the enhanced permeability and retention effect of solid tumors:

- Next-generation chemotherapeutics and photodynamic therapy—problems, solutions, and prospects,” *Microcirculation*, vol. 23, no. 3, pp. 173–82, 2016. [Online]. Available: <https://www.ncbi.nlm.nih.gov/pubmed/26237291>
- [15] J. F. Hainfeld, D. N. Slatkin, and H. M. Smilowitz, “The use of gold nanoparticles to enhance radiotherapy in mice,” *Phys Med Biol*, vol. 49, no. 18, pp. N309–15, 2004. [Online]. Available: <https://www.ncbi.nlm.nih.gov/pubmed/15509078>
- [16] G. R. Sarria, M. A. Berenguer Frances, and I. Linares Galiana, “Enhancing radiotherapy effect in breast cancer with nanoparticles: A review,” *Rep Pract Oncol Radiother*, vol. 24, no. 1, pp. 65–67, 2019. [Online]. Available: <https://www.ncbi.nlm.nih.gov/pubmed/30479580>
- [17] C. Hollander-Mieritz, J. Johansen, C. Johansen, I. R. Vogelius, C. A. Kristensen, and H. Pappot, “Comparing the patients’ subjective experiences of acute side effects during radiotherapy for head and neck cancer with four different patient-reported outcomes questionnaires,” *Acta Oncol*, vol. 58, no. 5, pp. 603–609, 2019. [Online]. Available: <https://www.ncbi.nlm.nih.gov/pubmed/30698098>
- [18] A. L. McNamara, W. W. Kam, N. Scales, S. J. McMahon, J. W. Bennett, H. L. Byrne, J. Schuemann, H. Paganetti, R. Banati, and Z. Kuncic, “Dose enhancement effects to the nucleus and mitochondria from gold nanoparticles in the cytosol,” *Phys Med Biol*, vol. 61, no. 16, pp. 5993–6010, 2016. [Online]. Available: <https://www.ncbi.nlm.nih.gov/pubmed/27435339>
- [19] K. Haume, S. Rosa, S. Grellet, M. A. Smialek, K. T. Butterworth, A. V. Solov’yov, K. M. Prise, J. Golding, and N. J. Mason, “Gold nanoparticles for cancer radiotherapy: a review,” *Cancer Nanotechnol*, vol. 7, no. 1, p. 8, 2016. [Online]. Available: <https://www.ncbi.nlm.nih.gov/pubmed/27867425>
- [20] J. Schuemann, R. Berbeco, D. B. Chithrani, S. H. Cho, R. Kumar, S. J. McMahon, S. Sridhar, and S. Krishnan, “Roadmap to clinical

- use of gold nanoparticles for radiation sensitization,” *Int J Radiat Oncol Biol Phys*, vol. 94, no. 1, pp. 189–205, 2016. [Online]. Available: <https://www.ncbi.nlm.nih.gov/pubmed/26700713>
- [21] J. E. Sager, J. Yu, I. Ragueneau-Majlessi, and N. Isoherranen, “Physiologically based pharmacokinetic (pbpk) modeling and simulation approaches: A systematic review of published models, applications, and model verification,” *Drug Metab Dispos*, vol. 43, no. 11, pp. 1823–37, 2015. [Online]. Available: <https://www.ncbi.nlm.nih.gov/pubmed/26296709>
- [22] M. Li, P. Zou, K. Tyner, and S. Lee, “Physiologically based pharmacokinetic (pbpk) modeling of pharmaceutical nanoparticles,” *AAPS J*, vol. 19, no. 1, pp. 26–42, 2017. [Online]. Available: <https://www.ncbi.nlm.nih.gov/pubmed/27834047>
- [23] W. I. Hagens, A. G. Oomen, W. H. de Jong, F. R. Cassee, and A. J. Sips, “What do we (need to) know about the kinetic properties of nanoparticles in the body?” *Regul Toxicol Pharmacol*, vol. 49, no. 3, pp. 217–29, 2007. [Online]. Available: <https://www.ncbi.nlm.nih.gov/pubmed/17868963>
- [24] M. Li, K. T. Al-Jamal, K. Kostarelos, and J. Reineke, “Physiologically based pharmacokinetic modeling of nanoparticles,” *ACS Nano*, vol. 4, no. 11, pp. 6303–17, 2010. [Online]. Available: <https://www.ncbi.nlm.nih.gov/pubmed/20945925>
- [25] V. Yellepeddi, J. Rower, X. Liu, S. Kumar, J. Rashid, and C. M. T. Sherwin, “State-of-the-art review on physiologically based pharmacokinetic modeling in pediatric drug development,” *Clin Pharmacokinet*, vol. 58, no. 1, pp. 1–13, 2019. [Online]. Available: <https://www.ncbi.nlm.nih.gov/pubmed/29777528>
- [26] D. Yuan, H. He, Y. Wu, J. Fan, and Y. Cao, “Physiologically based pharmacokinetic modeling of nanoparticles,” *J Pharm Sci*, vol. 108, no. 1, pp. 58–72, 2019. [Online]. Available: <https://www.ncbi.nlm.nih.gov/pubmed/30385282>

- [27] A. Mesbahi, “A review on gold nanoparticles radiosensitization effect in radiation therapy of cancer,” *Rep Pract Oncol Radiother*, vol. 15, no. 6, pp. 176–80, 2010. [Online]. Available: <https://www.ncbi.nlm.nih.gov/pubmed/24376946>
- [28] Z. Kuncic and S. Lacombe, “Nanoparticle radio-enhancement: principles, progress and application to cancer treatment,” *Phys Med Biol*, vol. 63, no. 2, p. 02TR01, 2018. [Online]. Available: <https://www.ncbi.nlm.nih.gov/pubmed/29125831>
- [29] W. Li, M. Müllner, M. Greiter, C. Bissardon, W. Xie, H. Schlatll, U. Oeh, J. Li, and C. Hoeschen, *Monte Carlo simulations of dose enhancement around gold nanoparticles used as X-ray imaging contrast agents and radiosensitizers*, ser. SPIE Medical Imaging. SPIE, 2014, vol. 9033. [Online]. Available: <https://doi.org/10.1117/12.2043687>
- [30] Y. Lin, S. J. McMahon, M. Scarpelli, H. Paganetti, and J. Schuemann, “Comparing gold nano-particle enhanced radiotherapy with protons, megavoltage photons and kilovoltage photons: a monte carlo simulation,” *Phys Med Biol*, vol. 59, no. 24, pp. 7675–89, 2014. [Online]. Available: <https://www.ncbi.nlm.nih.gov/pubmed/25415297>
- [31] W. Sung, S. Jung, and S. J. Ye, “Evaluation of the microscopic dose enhancement for nanoparticle-enhanced auger therapy,” *Phys Med Biol*, vol. 61, no. 21, pp. 7522–7535, 2016. [Online]. Available: <https://www.ncbi.nlm.nih.gov/pubmed/27716643>
- [32] H. Rabus, E. Gargioni, W. B. Li, H. Nettelbeck, and C. Villagrasa, “Determining dose enhancement factors of high-z nanoparticles from simulations where lateral secondary particle disequilibrium exists,” *Phys Med Biol*, vol. 64, no. 15, p. 155016, 2019. [Online]. Available: <https://www.ncbi.nlm.nih.gov/pubmed/31300616>

- [33] C. Lopez-Chaves, J. Soto-Alvaredo, M. Montes-Bayon, J. Bettmer, J. Llopis, and C. Sanchez-Gonzalez, “Gold nanoparticles: Distribution, bioaccumulation and toxicity. in vitro and in vivo studies,” *Nanomedicine*, vol. 14, no. 1, pp. 1–12, 2018. [Online]. Available: <https://www.ncbi.nlm.nih.gov/pubmed/28882675>
- [34] G. Multhoff, C. Botzler, M. Wiesnet, E. Muller, T. Meier, W. Wilmanns, and R. D. Issels, “A stress-inducible 72-kda heat-shock protein (hsp72) is expressed on the surface of human tumor cells, but not on normal cells,” *Int J Cancer*, vol. 61, no. 2, pp. 272–9, 1995. [Online]. Available: <https://www.ncbi.nlm.nih.gov/pubmed/7705958>
- [35] S. Stangl, M. Gehrman, J. Riegger, K. Kuhs, I. Riederer, W. Sievert, K. Hube, R. Mocikat, R. Dressel, E. Kremmer, A. G. Pockley, L. Friedrich, L. Vigh, A. Skerra, and G. Multhoff, “Targeting membrane heat-shock protein 70 (hsp70) on tumors by cmhsp70.1 antibody,” *Proc Natl Acad Sci U S A*, vol. 108, no. 2, pp. 733–8, 2011. [Online]. Available: <https://www.ncbi.nlm.nih.gov/pubmed/21187371>
- [36] S. Stangl, M. Gehrman, R. Dressel, F. Alves, C. Dullin, G. Themelis, V. Ntziachristos, E. Staeblein, A. Walch, I. Winkelmann, and G. Multhoff, “In vivo imaging of ct26 mouse tumours by using cmhsp70.1 monoclonal antibody,” *J Cell Mol Med*, vol. 15, no. 4, pp. 874–87, 2011. [Online]. Available: <https://www.ncbi.nlm.nih.gov/pubmed/20406322>
- [37] S. J. McMahon, W. B. Hyland, M. F. Muir, J. A. Coulter, S. Jain, K. T. Butterworth, G. Schettino, G. R. Dickson, A. R. Hounsell, J. M. O’Sullivan, K. M. Prise, D. G. Hirst, and F. J. Currell, “Biological consequences of nanoscale energy deposition near irradiated heavy atom nanoparticles,” *Sci Rep*, vol. 1, p. 18, 2011. [Online]. Available: <https://www.ncbi.nlm.nih.gov/pubmed/22355537>
- [38] G. Kraft, M. Scholz, and U. Bechthold, “Tumor therapy and track structure,”

- Radiat Environ Biophys*, vol. 38, no. 4, pp. 229–37, 1999. [Online]. Available: <https://www.ncbi.nlm.nih.gov/pubmed/10654344>
- [39] S. J. McMahon, W. B. Hyland, M. F. Muir, J. A. Coulter, S. Jain, K. T. Butterworth, G. Schettino, G. R. Dickson, A. R. Hounsell, J. M. O’Sullivan, K. M. Prise, D. G. Hirst, and F. J. Currell, “Nanodosimetric effects of gold nanoparticles in megavoltage radiation therapy,” *Radiother Oncol*, vol. 100, no. 3, pp. 412–6, 2011. [Online]. Available: <https://www.ncbi.nlm.nih.gov/pubmed/21924786>
- [40] Y. Lin, S. J. McMahon, H. Paganetti, and J. Schuemann, “Biological modeling of gold nanoparticle enhanced radiotherapy for proton therapy,” *Phys Med Biol*, vol. 60, no. 10, pp. 4149–68, 2015. [Online]. Available: <https://www.ncbi.nlm.nih.gov/pubmed/25953956>
- [41] W. Sung, S. J. Ye, A. L. McNamara, S. J. McMahon, J. Hainfeld, J. Shin, H. M. Smilowitz, H. Paganetti, and J. Schuemann, “Dependence of gold nanoparticle radiosensitization on cell geometry,” *Nanoscale*, vol. 9, no. 18, pp. 5843–5853, 2017. [Online]. Available: <https://www.ncbi.nlm.nih.gov/pubmed/28429022>
- [42] W. Sung, Y. Jeong, H. Kim, H. Jeong, C. Grassberger, S. Jung, G. O. Ahn, I. H. Kim, J. Schuemann, K. Lee, and S. J. Ye, “Computational modeling and clonogenic assay for radioenhancement of gold nanoparticles using 3d live cell images,” *Radiat Res*, vol. 190, no. 5, pp. 558–564, 2018. [Online]. Available: <https://www.ncbi.nlm.nih.gov/pubmed/30142031>
- [43] E. Lechtman, S. Mashouf, N. Chattopadhyay, B. M. Keller, P. Lai, Z. Cai, R. M. Reilly, and J. P. Pignol, “A monte carlo-based model of gold nanoparticle radiosensitization accounting for increased radiobiological effectiveness,” *Phys Med Biol*, vol. 58, no. 10, pp. 3075–87, 2013. [Online]. Available: <https://www.ncbi.nlm.nih.gov/pubmed/23594417>
- [44] V. Ferrero, G. Visona, F. Dalmaso, A. Gobbato, P. Cerello, L. Strigari, S. Visentin, and A. Attili, “Targeted dose enhancement in radiotherapy for

- breast cancer using gold nanoparticles, part 1: A radiobiological model study,” *Med Phys*, vol. 44, no. 5, pp. 1983–1992, 2017. [Online]. Available: <https://www.ncbi.nlm.nih.gov/pubmed/28236655>
- [45] W. Friedland, M. Dingfelder, P. Kundrat, and P. Jacob, “Track structures, dna targets and radiation effects in the biophysical monte carlo simulation code partrac,” *Mutat Res*, vol. 711, no. 1-2, pp. 28–40, 2011. [Online]. Available: <https://www.ncbi.nlm.nih.gov/pubmed/21281649>
- [46] S. Agostinelli, J. Allison, K. Amako, J. Apostolakis, H. Araujo, P. Arce, M. Asai, D. Axen, S. Banerjee, G. Barrand, F. Behner, L. Bellagamba, J. Boudreau, L. Broglia, A. Brunengo, H. Burkhardt, S. Chauvie, J. Chuma, R. Chytracsek, G. Cooperman, G. Cosmo, P. Degtyarenko, A. Dell’Acqua, G. Depaola, D. Dietrich, R. Enami, A. Feliciello, C. Ferguson, H. Fesefeldt, G. Folger, F. Foppiano, A. Forti, S. Garelli, S. Giani, R. Giannitrapani, D. Gibin, J. J. Gómez Cadenas, I. González, G. Gracia Abril, G. Greeniaus, W. Greiner, V. Grichine, A. Grossheim, S. Guatelli, P. Gumplinger, R. Hamatsu, K. Hashimoto, H. Hasui, A. Heikkinen, A. Howard, V. Ivanchenko, A. Johnson, F. W. Jones, J. Kallenbach, N. Kanaya, M. Kawabata, Y. Kawabata, M. Kawaguti, S. Kelner, P. Kent, A. Kimura, T. Kodama, R. Kokoulin, M. Kossov, H. Kurashige, E. Lamanna, T. Lampén, V. Lara, V. Lefebure, F. Lei, M. Liendl, W. Lockman, F. Longo, S. Magni, M. Maire, E. Medernach, K. Minamimoto, P. Mora de Freitas, Y. Morita, K. Murakami, M. Nagamatu, R. Nartallo, P. Nieminen, T. Nishimura, K. Ohtsubo, M. Okamura, S. O’Neale, Y. Oohata, K. Paech, J. Perl, A. Pfeiffer, M. G. Pia, F. Ranjard, A. Rybin, S. Sadilov, E. Di Salvo, G. Santin, T. Sasaki, N. Savvas, Y. Sawada *et al.*, “Geant4—a simulation toolkit,” *Nuclear Instruments and Methods in Physics Research Section A: Accelerators, Spectrometers, Detectors and Associated Equipment*, vol. 506, no. 3, pp. 250–303, 2003. [Online]. Available: <http://www.sciencedirect.com/science/article/pii/S0168900203013688>

- [47] J. Allison, K. Amako, J. Apostolakis, P. Arce, M. Asai, T. Aso, E. Bagli, A. Bagulya, S. Banerjee, G. Barrand, B. R. Beck, A. G. Bogdanov, D. Brandt, J. M. C. Brown, H. Burkhardt, P. Canal, D. Cano-Ott, S. Chauvie, K. Cho, G. A. P. Cirrone, G. Cooperman, M. A. Cortés-Giraldo, G. Cosmo, G. Cuttone, G. Depaola, L. Desorgher, X. Dong, A. Dotti, V. D. Elvira, G. Folger, Z. Francis, A. Galoyan, L. Garnier, M. Gayer, K. L. Genser, V. M. Grichine, S. Guatelli, P. Guèye, P. Gumplinger, A. S. Howard, I. Hřivnáčová, S. Hwang, S. Incerti, A. Ivanchenko, V. N. Ivanchenko, F. W. Jones, S. Y. Jun, P. Kaitaniemi, N. Karakatsanis, M. Karamitros, M. Kelsey, A. Kimura, T. Koi, H. Kurashige, A. Lechner, S. B. Lee, F. Longo, M. Maire, D. Mancusi, A. Mantero, E. Mendoza, B. Morgan, K. Murakami, T. Nikitina, L. Pandola, P. Paprocki, J. Perl, I. Petrović, M. G. Pia, W. Pokorski, J. M. Quesada, M. Raine, M. A. Reis, A. Ribon, A. Ristić Fira, F. Romano, G. Russo, G. Santin, T. Sasaki, D. Sawkey, J. I. Shin, I. I. Strakovsky, A. Taborda, S. Tanaka, B. Tomé, T. Toshito, H. N. Tran, P. R. Truscott, L. Urban, V. Uzhinsky, J. M. Verbeke, M. Verderi, B. L. Wendt, H. Wenzel, D. H. Wright, D. M. Wright, T. Yamashita, J. Yarba, and H. Yoshida, “Recent developments in geant4,” *Nuclear Instruments and Methods in Physics Research Section A: Accelerators, Spectrometers, Detectors and Associated Equipment*, vol. 835, pp. 186–225, 2016. [Online]. Available: <http://www.sciencedirect.com/science/article/pii/S0168900216306957>
- [48] V. Ivanchenko, A. Bagulya, S. Bakr, M. Bandieramonte, D. Bernard, M.-C. Bordage, J. Brown, H. Burkhardt, P. Dondero, S. Elles, V. Grichine, S. Guatelli, F. Hariri, A. Howard, S. Incerti, S. Yung Jun, O. Kadri, I. Kyriakou, M. Maire, A. Mantero, M. Novak, D. Sawkey, D. Sawkey, I. Semeniouk, A. Sokolov, and L. Urban, “Progress of geant4 electromagnetic physics developments and applications,” *EPJ Web Conf.*, vol. 214, p. 02046, 2019. [Online]. Available: <https://doi.org/10.1051/epjconf/201921402046>
- [49] S. INCERTI, G. BALDACCHINO, M. BERNAL, R. CAPRA, C. CHAM-

- PION, Z. FRANCIS, P. GUÈYE, A. MANTERO, B. MASCIALINO, P. MORETTO, P. NIEMINEN, C. VILLAGRASA, and C. ZACHARATOU, “The geant4-dna project,” *International Journal of Modeling, Simulation, and Scientific Computing*, vol. 01, no. 02, pp. 157–178, 2010. [Online]. Available: <https://www.worldscientific.com/doi/abs/10.1142/S1793962310000122>
- [50] S. Jan, G. Santin, D. Strul, S. Staelens, K. Assie, D. Autret, S. Avner, R. Barbier, M. Bardies, P. M. Bloomfield, D. Brasse, V. Breton, P. Bruyndonckx, I. Buvat, A. F. Chatziioannou, Y. Choi, Y. H. Chung, C. Comtat, D. Donnarieix, L. Ferrer, S. J. Glick, C. J. Groiselle, D. Guez, P. F. Honore, S. Kerhoas-Cavata, A. S. Kirov, V. Kohli, M. Koole, M. Krieguer, D. J. van der Laan, F. Lamare, G. Largeron, C. Lartizien, D. Lazaro, M. C. Maas, L. Maigne, F. Mayet, F. Melot, C. Merheb, E. Pennacchio, J. Perez, U. Pietrzyk, F. R. Rannou, M. Rey, D. R. Schaart, C. R. Schmidtlein, L. Simon, T. Y. Song, J. M. Vieira, D. Visvikis, R. Van de Walle, E. Wieers, and C. Morel, “Gate: a simulation toolkit for pet and spect,” *Phys Med Biol*, vol. 49, no. 19, pp. 4543–61, 2004. [Online]. Available: <https://www.ncbi.nlm.nih.gov/pubmed/15552416>
- [51] J. Perl, J. Shin, J. Schumann, B. Faddegon, and H. Paganetti, “Topas: an innovative proton monte carlo platform for research and clinical applications,” *Med Phys*, vol. 39, no. 11, pp. 6818–37, 2012. [Online]. Available: <https://www.ncbi.nlm.nih.gov/pubmed/23127075>
- [52] J. Schümann, H. Paganetti, J. Shin, B. Faddegon, and J. Perl, “Efficient voxel navigation for proton therapy dose calculation in topas and geant4,” *Physics in Medicine and Biology*, vol. 57, no. 11, pp. 3281–3293, 2012. [Online]. Available: <http://dx.doi.org/10.1088/0031-9155/57/11/3281>
- [53] J. Ramos-Mendez, J. Perl, J. Schumann, J. Shin, H. Paganetti, and B. Faddegon, “A framework for implementation of organ effect models in topas with benchmarks extended to proton therapy,” *Phys*

- Med Biol*, vol. 60, no. 13, pp. 5037–52, 2015. [Online]. Available: <https://www.ncbi.nlm.nih.gov/pubmed/26061583>
- [54] H. Zhu, Y. Chen, W. Sung, A. L. McNamara, L. T. Tran, L. N. Burigo, A. B. Rosenfeld, J. Li, B. Faddegon, J. Schuemann, and H. Paganetti, “The microdosimetric extension in topas: development and comparison with published data,” *Phys Med Biol*, vol. 64, no. 14, p. 145004, 2019. [Online]. Available: <https://www.ncbi.nlm.nih.gov/pubmed/31117056>
- [55] J. Schuemann, A. L. McNamara, J. Ramos-Mendez, J. Perl, K. D. Held, H. Paganetti, S. Incerti, and B. Faddegon, “Topas-nbio: An extension to the topas simulation toolkit for cellular and sub-cellular radiobiology,” *Radiat Res*, vol. 191, no. 2, pp. 125–138, 2019. [Online]. Available: <https://www.ncbi.nlm.nih.gov/pubmed/30609382>
- [56] A. L. McNamara, J. Ramos-Mendez, J. Perl, K. Held, N. Dominguez, E. Moreno, N. T. Henthorn, K. J. Kirkby, S. Meylan, C. Villagrasa, S. Incerti, B. Faddegon, H. Paganetti, and J. Schuemann, “Geometrical structures for radiation biology research as implemented in the topas-nbio toolkit,” *Phys Med Biol*, vol. 63, no. 17, p. 175018, 2018. [Online]. Available: <https://www.ncbi.nlm.nih.gov/pubmed/30088810>
- [57] H. Zhu, A. L. McNamara, S. J. McMahon, J. Ramos-Mendez, N. T. Henthorn, B. Faddegon, K. D. Held, J. Perl, J. Li, H. Paganetti, and J. Schuemann, “Cellular response to proton irradiation: A simulation study with topas-nbio,” *Radiat Res*, vol. 194, no. 1, pp. 9–21, 2020. [Online]. Available: <https://www.ncbi.nlm.nih.gov/pubmed/32401689>
- [58] J. Müller and C. Kuttler, *Methods and Models in Mathematical Biology: Deterministic and Stochastic Approaches*, ser. Lecture Notes on Mathematical Modelling in the Life Sciences. Springer Berlin Heidelberg, 2015. [Online]. Available: <https://books.google.de/books?id=qRRcCgAAQBAJ>

- [59] S. E. Rosenbaum, *Basic Pharmacokinetics and Pharmacodynamics : An Integrated Textbook and Computer Simulations*. Hoboken, N.J.: Wiley, 2011. [Online]. Available: <http://search.ebscohost.com/login.aspx?direct=true&db=nlebk&AN=517765&site=ehost-live>
- [60] S. M. Pimblott and J. A. LaVerne, “Production of low-energy electrons by ionizing radiation,” *Radiation Physics and Chemistry*, vol. 76, no. 8-9, pp. 1244–1247, 2007. [Online]. Available: <https://www.sciencedirect.com/science/article/pii/S0969806X07000448>
- [61] E. B. Podgorsak, *Radiation Physics for Medical Physicists*, ser. Graduate Texts in Physics. Springer International Publishing, 2016. [Online]. Available: <http://dx.doi.org/10.1007/978-3-319-25382-4>
- [62] M. J. Gazda and L. R. Coia, “Principles of radiation therapy,” *Cancer management: a multidisciplinary approach*, 2001.
- [63] K. T. Butterworth, S. J. McMahon, F. J. Currell, and K. M. Prise, “Physical basis and biological mechanisms of gold nanoparticle radiosensitization,” *Nanoscale*, vol. 4, no. 16, pp. 4830–8, 2012. [Online]. Available: <https://www.ncbi.nlm.nih.gov/pubmed/22767423>
- [64] J. Choi, G. Kim, S. B. Cho, and H. J. Im, “Radiosensitizing high-z metal nanoparticles for enhanced radiotherapy of glioblastoma multiforme,” *J Nanobiotechnology*, vol. 18, no. 1, p. 122, 2020. [Online]. Available: <https://www.ncbi.nlm.nih.gov/pubmed/32883290>
- [65] T. D. Clemons, R. H. Kerr, and A. Joos, *3.10 - Multifunctional Magnetic Nanoparticles: Design, Synthesis, and Biomedical Applications*. Oxford: Academic Press, 2019, pp. 193–210. [Online]. Available: <https://www.sciencedirect.com/science/article/pii/B978012803581810462X>
- [66] A. V. Samrot, C. S. Sahithya, J. Selvarani A, S. K. Purayil, and P. Ponnaiah, “A review on synthesis, characterization and potential biological applications

- of superparamagnetic iron oxide nanoparticles,” *Current Research in Green and Sustainable Chemistry*, vol. 4, p. 100042, 2021. [Online]. Available: <https://www.sciencedirect.com/science/article/pii/S266608652030045X>
- [67] L. T. Baxter, H. Zhu, D. G. Mackensen, and R. K. Jain, “Physiologically based pharmacokinetic model for specific and nonspecific monoclonal antibodies and fragments in normal tissues and human tumor xenografts in nude mice,” *Cancer Res*, vol. 54, no. 6, pp. 1517–28, 1994. [Online]. Available: <https://www.ncbi.nlm.nih.gov/pubmed/8137258>
- [68] M. L. Bigham and F. Cockrem, “Body weights, tail lengths, body temperatures, food intakes, & some slaughter data for four strains of mice reared at three different environmental temperatures,” *New Zealand Journal of Agricultural Research*, vol. 12, no. 4, pp. 658–668, 2012. [Online]. Available: <https://doi.org/10.1080/00288233.1969.10421217>
- [69] M. Konarzewski and J. Diamond, “Evolution of basal metabolic rate and organ masses in laboratory mice,” *Evolution*, vol. 49, no. 6, pp. 1239–1248, 1995. [Online]. Available: <https://www.ncbi.nlm.nih.gov/pubmed/28568534>
- [70] A. Kumral, K. Tugyan, S. Gonenc, K. Genc, S. Genc, U. Sonmez, O. Yilmaz, N. Duman, N. Uysal, and H. Ozkan, “Protective effects of erythropoietin against ethanol-induced apoptotic neurodegeneration and oxidative stress in the developing c57bl/6 mouse brain,” *Brain Res Dev Brain Res*, vol. 160, no. 2, pp. 146–56, 2005. [Online]. Available: <https://www.ncbi.nlm.nih.gov/pubmed/16236368>
- [71] A. C. Riches, J. G. Sharp, D. B. Thomas, and S. V. Smith, “Blood volume determination in the mouse,” *J Physiol*, vol. 228, no. 2, pp. 279–84, 1973. [Online]. Available: <https://www.ncbi.nlm.nih.gov/pubmed/4687099>
- [72] Q. Wang, P. Sun, G. Li, K. Zhu, C. Wang, and X. Zhao, “Inhibitory effects of dendrobium candidum wall ex lindl. on azoxymethane- and dextran sulfate sodium-induced colon carcinogenesis in c57bl/6 mice,”

- Oncol Lett*, vol. 7, no. 2, pp. 493–498, 2014. [Online]. Available: <https://www.ncbi.nlm.nih.gov/pubmed/24396476>
- [73] F. Xiao, T. Furuta, M. Takashima, N. Shirai, and H. Hanai, “Involvement of cyclooxygenase-2 in hyperplastic gastritis induced by helicobacter pylori infection in c57bl/6 mice,” *Aliment Pharmacol Ther*, vol. 15, no. 6, pp. 875–86, 2001. [Online]. Available: <https://www.ncbi.nlm.nih.gov/pubmed/11380326>
- [74] T. Xie and H. Zaidi, “Monte carlo-based evaluation of s-values in mouse models for positron-emitting radionuclides,” *Phys Med Biol*, vol. 58, no. 1, pp. 169–82, 2013. [Online]. Available: <https://www.ncbi.nlm.nih.gov/pubmed/23221270>
- [75] P. Andreo, D. T. Burns, and F. Salvat, “On the uncertainties of photon mass energy-absorption coefficients and their ratios for radiation dosimetry,” *Phys Med Biol*, vol. 57, no. 8, pp. 2117–36, 2012. [Online]. Available: <https://www.ncbi.nlm.nih.gov/pubmed/22451262>
- [76] P. M. Shikhaliev and S. G. Fritz, “Photon counting spectral ct versus conventional ct: comparative evaluation for breast imaging application,” *Phys Med Biol*, vol. 56, no. 7, pp. 1905–30, 2011. [Online]. Available: <https://www.ncbi.nlm.nih.gov/pubmed/21364268>
- [77] A. C. Tedgren, A. Hedman, J. E. Grindborg, and G. A. Carlsson, “Response of lif:mg,ti thermoluminescent dosimeters at photon energies relevant to the dosimetry of brachytherapy (<1 mev),” *Med Phys*, vol. 38, no. 10, pp. 5539–50, 2011. [Online]. Available: <https://www.ncbi.nlm.nih.gov/pubmed/21992372>
- [78] J. Wong, E. Armour, P. Kazanzides, I. Iordachita, E. Tryggestad, H. Deng, M. Matinfar, C. Kennedy, Z. Liu, T. Chan, O. Gray, F. Verhaegen, T. McNutt, E. Ford, and T. L. DeWeese, “High-resolution, small animal radiation research platform with x-ray tomographic guidance capabilities,” *International journal of radiation oncology, biology, physics*, vol. 71, no. 5, pp. 1591–1599, 2008. [Online]. Available: <https://pubmed.ncbi.nlm.nih.gov/18640502https://www.ncbi.nlm.nih.gov/pmc/articles/PMC2605655/>

- [79] S. Meylan, S. Incerti, M. Karamitros, N. Tang, M. Bueno, I. Clairand, and C. Villagrasa, “Simulation of early dna damage after the irradiation of a fibroblast cell nucleus using geant4-dna,” *Sci Rep*, vol. 7, no. 1, p. 11923, 2017. [Online]. Available: <https://www.ncbi.nlm.nih.gov/pubmed/28931851>
- [80] B. Rudek, A. McNamara, J. Ramos-Mendez, H. Byrne, Z. Kuncic, and J. Schuemann, “Radio-enhancement by gold nanoparticles and their impact on water radiolysis for x-ray, proton and carbon-ion beams,” *Phys Med Biol*, vol. 64, no. 17, p. 175005, 2019. [Online]. Available: <https://www.ncbi.nlm.nih.gov/pubmed/31295730>
- [81] D. Sakata, N. Lampe, M. Karamitros, I. Kyriakou, O. Belov, M. A. Bernal, D. Bolst, M. C. Bordage, V. Breton, J. M. C. Brown, Z. Francis, V. Ivanchenko, S. Meylan, K. Murakami, S. Okada, I. Petrovic, A. Ristic-Fira, G. Santin, D. Sarramia, T. Sasaki, W. G. Shin, N. Tang, H. N. Tran, C. Villagrasa, D. Emfietzoglou, P. Nieminen, S. Guatelli, and S. Incerti, “Evaluation of early radiation dna damage in a fractal cell nucleus model using geant4-dna,” *Phys Med*, vol. 62, pp. 152–157, 2019. [Online]. Available: <https://www.ncbi.nlm.nih.gov/pubmed/31109825>
- [82] “Physics lists em constructors in geant4 10.4,” Jul. 2021. [Online]. Available: <https://geant4.web.cern.ch/node/1731>
- [83] B. A. Pulaski and S. Ostrand-Rosenberg, “Mouse 4t1 breast tumor model,” *Curr Protoc Immunol*, vol. Chapter 20, p. Unit 20 2, 2001. [Online]. Available: <https://www.ncbi.nlm.nih.gov/pubmed/18432775>
- [84] S. A. DuPre, D. Redelman, and J. Hunter, K. W., “The mouse mammary carcinoma 4t1: characterization of the cellular landscape of primary tumours and metastatic tumour foci,” *Int J Exp Pathol*, vol. 88, no. 5, pp. 351–60, 2007. [Online]. Available: <https://www.ncbi.nlm.nih.gov/pubmed/17877537>
- [85] W. D. Foulkes, I. E. Smith, and J. S. Reis-Filho, “Triple-negative breast

- cancer,” *N Engl J Med*, vol. 363, no. 20, pp. 1938–48, 2010. [Online]. Available: <https://www.ncbi.nlm.nih.gov/pubmed/21067385>
- [86] S. Stangl, J. Varga, B. Freysoldt, M. Trajkovic-Arsic, J. T. Siveke, F. R. Greten, V. Ntziachristos, and G. Multhoff, “Selective in vivo imaging of syngeneic, spontaneous, and xenograft tumors using a novel tumor cell-specific hsp70 peptide-based probe,” *Cancer Res*, vol. 74, no. 23, pp. 6903–12, 2014. [Online]. Available: <https://www.ncbi.nlm.nih.gov/pubmed/25300920>
- [87] K. Takai, A. Le, V. M. Weaver, and Z. Werb, “Targeting the cancer-associated fibroblasts as a treatment in triple-negative breast cancer,” *Oncotarget*, vol. 7, no. 50, pp. 82 889–82 901, 2016. [Online]. Available: <https://www.ncbi.nlm.nih.gov/pubmed/27756881>
- [88] M. L. Oelze, J. O’Brien, W. D., J. P. Blue, and J. F. Zachary, “Differentiation and characterization of rat mammary fibroadenomas and 4t1 mouse carcinomas using quantitative ultrasound imaging,” *IEEE Trans Med Imaging*, vol. 23, no. 6, pp. 764–71, 2004. [Online]. Available: <https://www.ncbi.nlm.nih.gov/pubmed/15191150>
- [89] V. S. LeBleu, J. T. O’Connell, K. N. Gonzalez Herrera, H. Wikman, K. Pantel, M. C. Haigis, F. M. de Carvalho, A. Damascena, L. T. Domingos Chinen, R. M. Rocha, J. M. Asara, and R. Kalluri, “Pgc-1alpha mediates mitochondrial biogenesis and oxidative phosphorylation in cancer cells to promote metastasis,” *Nat Cell Biol*, vol. 16, no. 10, pp. 992–1003, 1–15, 2014. [Online]. Available: <https://www.ncbi.nlm.nih.gov/pubmed/25241037>
- [90] K. Karanth, “Generating random points in a sphere,” Aug. 2018. [Online]. Available: <https://karthikkaranth.me/blog/generating-random-points-in-a-sphere/#>
- [91] S. Incerti, I. Kyriakou, M. A. Bernal, M. C. Bordage, Z. Francis, S. Guatelli, V. Ivanchenko, M. Karamitros, N. Lampe, S. B. Lee, S. Meylan, C. H. Min, W. G. Shin, P. Nieminen, D. Sakata, N. Tang, C. Villagrasa, H. N. Tran,

- and J. M. C. Brown, “Geant4-dna example applications for track structure simulations in liquid water: A report from the geant4-dna project,” *Med Phys*, 2018. [Online]. Available: <https://www.ncbi.nlm.nih.gov/pubmed/29901835>
- [92] Y. Pan, A. Leifert, D. Ruau, S. Neuss, J. Bornemann, G. Schmid, W. Brandau, U. Simon, and W. Jahnen-Dechent, “Gold nanoparticles of diameter 1.4 nm trigger necrosis by oxidative stress and mitochondrial damage,” *Small*, vol. 5, no. 18, pp. 2067–76, 2009. [Online]. Available: <https://www.ncbi.nlm.nih.gov/pubmed/19642089>
- [93] R. Liu, Y. Wang, Q. Yuan, D. An, J. Li, and X. Gao, “The au clusters induce tumor cell apoptosis via specifically targeting thioredoxin reductase 1 (trxr1) and suppressing its activity,” *Chem Commun (Camb)*, vol. 50, no. 73, pp. 10 687–90, 2014. [Online]. Available: <https://www.ncbi.nlm.nih.gov/pubmed/25078326>
- [94] C. Sicard-Roselli, E. Brun, M. Gilles, G. Baldacchino, C. Kelsey, H. McQuaid, C. Polin, N. Wardlow, and F. Currell, “A new mechanism for hydroxyl radical production in irradiated nanoparticle solutions,” *Small*, vol. 10, no. 16, pp. 3338–46, 2014. [Online]. Available: <https://www.ncbi.nlm.nih.gov/pubmed/24863679>
- [95] S. J. Seo, J. K. Jeon, S. M. Han, and J. K. Kim, “Reactive oxygen species-based measurement of the dependence of the coulomb nanoradiator effect on proton energy and atomic z value,” *Int J Radiat Biol*, vol. 93, no. 11, pp. 1239–1247, 2017. [Online]. Available: <https://www.ncbi.nlm.nih.gov/pubmed/28752783>
- [96] H. Zhu, A. L. McNamara, J. Ramos-Mendez, S. J. McMahon, N. T. Henthorn, B. Faddegon, K. D. Held, J. Perl, J. Li, H. Paganetti, and J. Schuemann, “A parameter sensitivity study for simulating dna damage after proton irradiation using topas-nbio,” *Phys Med Biol*, vol. 65, no. 8, p. 085015, 2020. [Online]. Available: <https://www.ncbi.nlm.nih.gov/pubmed/32101803>

- [97] E. Lieberman-Aiden, N. L. van Berkum, L. Williams, M. Imakaev, T. Ragoczy, A. Telling, I. Amit, B. R. Lajoie, P. J. Sabo, M. O. Dorschner, R. Sandstrom, B. Bernstein, M. A. Bender, M. Groudine, A. Gnirke, J. Stamatoyannopoulos, L. A. Mirny, E. S. Lander, and J. Dekker, “Comprehensive mapping of long-range interactions reveals folding principles of the human genome,” *Science*, vol. 326, no. 5950, pp. 289–93, 2009. [Online]. Available: <https://www.ncbi.nlm.nih.gov/pubmed/19815776>
- [98] M. A. Smialek, N. C. Jones, S. V. Hoffmann, and N. J. Mason, “Measuring the density of dna films using ultraviolet-visible interferometry,” *Phys Rev E Stat Nonlin Soft Matter Phys*, vol. 87, no. 6, p. 060701, 2013. [Online]. Available: <https://www.ncbi.nlm.nih.gov/pubmed/23848615>
- [99] N. Lampe, M. Karamitros, V. Breton, J. M. C. Brown, I. Kyriakou, D. Sakata, D. Sarramia, and S. Incerti, “Mechanistic dna damage simulations in geant4-dna part 1: A parameter study in a simplified geometry,” *Phys Med*, vol. 48, pp. 135–145, 2018. [Online]. Available: <https://www.ncbi.nlm.nih.gov/pubmed/29628360>
- [100] J. Ramos-Mendez, J. Perl, J. Schuemann, A. McNamara, H. Paganetti, and B. Faddegon, “Monte carlo simulation of chemistry following radiolysis with topas-nbio,” *Phys Med Biol*, vol. 63, no. 10, p. 105014, 2018. [Online]. Available: <https://www.ncbi.nlm.nih.gov/pubmed/29697057>
- [101] H. Nikjoo, P. O’Neill, W. E. Wilson, and D. T. Goodhead, “Computational approach for determining the spectrum of dna damage induced by ionizing radiation,” *Radiat Res*, vol. 156, no. 5 Pt 2, pp. 577–83, 2001. [Online]. Available: <https://www.ncbi.nlm.nih.gov/pubmed/11604075>
- [102] R. Watanabe, S. Rahmanian, and H. Nikjoo, “Spectrum of radiation-induced clustered non-dsb damage - a monte carlo track structure modeling and calculations,” *Radiat Res*, vol. 183, no. 5, pp. 525–40, 2015. [Online]. Available: <https://www.ncbi.nlm.nih.gov/pubmed/25909147>

- [103] M. Mokari, M. H. Alamatsaz, H. Moeini, and R. Taleei, "A simulation approach for determining the spectrum of dna damage induced by protons," *Phys Med Biol*, vol. 63, no. 17, p. 175003, 2018. [Online]. Available: <https://www.ncbi.nlm.nih.gov/pubmed/30074903>
- [104] M. Mahmoudi, S. Sant, B. Wang, S. Laurent, and T. Sen, "Superparamagnetic iron oxide nanoparticles (spions): development, surface modification and applications in chemotherapy," *Adv Drug Deliv Rev*, vol. 63, no. 1-2, pp. 24–46, 2011. [Online]. Available: <https://www.ncbi.nlm.nih.gov/pubmed/20685224>
- [105] V. I. Shubayev, n. Pisanic, T. R., and S. Jin, "Magnetic nanoparticles for theragnostics," *Adv Drug Deliv Rev*, vol. 61, no. 6, pp. 467–77, 2009. [Online]. Available: <https://www.ncbi.nlm.nih.gov/pubmed/19389434>
- [106] S. D. Kong, J. Lee, S. Ramachandran, B. P. Eliceiri, V. I. Shubayev, R. Lal, and S. Jin, "Magnetic targeting of nanoparticles across the intact blood-brain barrier," *J Control Release*, vol. 164, no. 1, pp. 49–57, 2012. [Online]. Available: <https://www.ncbi.nlm.nih.gov/pubmed/23063548>
- [107] Z. Abed, J. Beik, S. Laurent, N. Eslahi, T. Khani, E. S. Davani, H. Ghaznavi, and A. Shakeri-Zadeh, "Iron oxide-gold core-shell nano-theranostic for magnetically targeted photothermal therapy under magnetic resonance imaging guidance," *J Cancer Res Clin Oncol*, vol. 145, no. 5, pp. 1213–1219, 2019. [Online]. Available: <https://www.ncbi.nlm.nih.gov/pubmed/30847551>
- [108] S. Rudge, C. Peterson, C. Vessely, J. Koda, S. Stevens, and L. Catterall, "Adsorption and desorption of chemotherapeutic drugs from a magnetically targeted carrier (mtc)," *J Control Release*, vol. 74, no. 1-3, pp. 335–40, 2001. [Online]. Available: <https://www.ncbi.nlm.nih.gov/pubmed/11489515>
- [109] P. R. Lockman, R. J. Mumper, M. A. Khan, and D. D. Allen, "Nanoparticle technology for drug delivery across the blood-brain barrier," *Drug Dev Ind Pharm*, vol. 28, no. 1, pp. 1–13, 2002. [Online]. Available: <https://www.ncbi.nlm.nih.gov/pubmed/11858519>

- [110] M. Jeun, Y. J. Kim, K. H. Park, S. H. Paek, and S. Bae, “Physical contribution of neel and brown relaxation to interpreting intracellular hyperthermia characteristics using superparamagnetic nanofluids,” *J Nanosci Nanotechnol*, vol. 13, no. 8, pp. 5719–25, 2013. [Online]. Available: <https://www.ncbi.nlm.nih.gov/pubmed/23882824>
- [111] A. E. Deatsch and B. A. Evans, “Heating efficiency in magnetic nanoparticle hyperthermia,” *Journal of Magnetism and Magnetic Materials*, vol. 354, pp. 163–172, 2014. [Online]. Available: <https://www.sciencedirect.com/science/article/pii/S0304885313007981>
- [112] J. Beik, M. Asadi, S. Khoei, S. Laurent, Z. Abed, M. Mirrahimi, A. Farashahi, R. Hashemian, H. Ghaznavi, and A. Shakeri-Zadeh, “Simulation-guided photothermal therapy using mri-traceable iron oxide-gold nanoparticle,” *J Photochem Photobiol B*, vol. 199, p. 111599, 2019. [Online]. Available: <https://www.ncbi.nlm.nih.gov/pubmed/31470271>
- [113] D. Dhar, S. Ghosh, S. Das, and J. Chatterjee, “A review of recent advances in magnetic nanoparticle-based theranostics of glioblastoma,” *Nanomedicine (Lond)*, vol. 17, no. 2, pp. 107–132, 2022. [Online]. Available: <https://www.ncbi.nlm.nih.gov/pubmed/35000429>
- [114] Y. Huang, B. Zhang, S. Xie, B. Yang, Q. Xu, and J. Tan, “Superparamagnetic iron oxide nanoparticles modified with tween 80 pass through the intact blood-brain barrier in rats under magnetic field,” *ACS Appl Mater Interfaces*, vol. 8, no. 18, pp. 11 336–41, 2016. [Online]. Available: <https://www.ncbi.nlm.nih.gov/pubmed/27092793>
- [115] U. K. Sukumar, R. J. C. Bose, M. Malhotra, H. A. Babikir, R. Afjei, E. Robinson, Y. Zeng, E. Chang, F. Habte, R. Sinclair, S. S. Gambhir, T. F. Massoud, and R. Paulmurugan, “Intranasal delivery of targeted polyfunctional gold-iron oxide nanoparticles loaded with therapeutic micrnas for combined theranostic multimodality imaging and presensitization of glioblastoma to

- temozolomide,” *Biomaterials*, vol. 218, p. 119342, 2019. [Online]. Available: <https://www.ncbi.nlm.nih.gov/pubmed/31326657>
- [116] A. Henrique Silva, E. Lima Jr, M. Vasquez Mansilla, R. D. Zysler, M. L. Mojica Piscioti, C. Locatelli, R. Kumar Reddy Rajoli, A. Owen, T. B. Creczynski-Pasa, and M. Siccardi, “A physiologically based pharmacokinetic model to predict the superparamagnetic iron oxide nanoparticles (spions) accumulation in vivo,” *European Journal of Nanomedicine*, vol. 9, no. 2, pp. 79–90, 2017. [Online]. Available: <https://doi.org/10.1515/ejnm-2017-0001>
- [117] A. Raue, M. Schilling, J. Bachmann, A. Matteson, M. Schelker, D. Kaschek, S. Hug, C. Kreutz, B. D. Harms, F. J. Theis, U. Klingmuller, and J. Timmer, “Lessons learned from quantitative dynamical modeling in systems biology,” *PLoS One*, vol. 8, no. 9, p. e74335, 2013. [Online]. Available: <https://www.ncbi.nlm.nih.gov/pubmed/24098642>
- [118] T. Xia, J. Wang, C. Wu, F. Meng, Z. Shi, J. Lian, J. Feng, and J. Meng, “Novel complex-coprecipitation route to form high quality triethanolamine-coated fe₃o₄ nanocrystals: Their high saturation magnetizations and excellent water treatment properties,” *CrystEngComm*, vol. 14, no. 18, pp. 5741–5744, 2012. [Online]. Available: <http://dx.doi.org/10.1039/C2CE25813G>
- [119] N. Elahi and M. Rizwan, “Progress and prospects of magnetic iron oxide nanoparticles in biomedical applications: A review,” *Artif Organs*, vol. 45, no. 11, pp. 1272–1299, 2021. [Online]. Available: <https://www.ncbi.nlm.nih.gov/pubmed/34245037>
- [120] L. M. Sanchez and V. A. Alvarez, “Advances in magnetic noble metal/iron-based oxide hybrid nanoparticles as biomedical devices,” *Bioengineering (Basel)*, vol. 6, no. 3, 2019. [Online]. Available: <https://www.ncbi.nlm.nih.gov/pubmed/31466238>
- [121] B. Chudasama, A. K. Vala, N. Andhariya, R. V. Upadhyay, and R. V. Mehta, “Enhanced antibacterial activity of bifunctional fe₃o₄-ag core-shell

- nanostructures,” *Nano Research*, vol. 2, no. 12, pp. 955–965, 2009. [Online]. Available: <https://doi.org/10.1007/s12274-009-9098-4>
- [122] H. V. Tran, N. M. Ngo, R. Medhi, P. Srinoi, T. Liu, S. Rittikulsittichai, and T. R. Lee, “Multifunctional iron oxide magnetic nanoparticles for biomedical applications: A review,” *Materials (Basel)*, vol. 15, no. 2, 2022. [Online]. Available: <https://www.ncbi.nlm.nih.gov/pubmed/35057223>
- [123] A. McNamara, C. Geng, R. Turner, J. R. Mendez, J. Perl, K. Held, B. Faddegon, H. Paganetti, and J. Schuemann, “Validation of the radiobiology toolkit topas-nbio in simple dna geometries,” *Phys Med*, vol. 33, pp. 207–215, 2017. [Online]. Available: <https://www.ncbi.nlm.nih.gov/pubmed/28017738>
- [124] M. Karamitros, S. Incerti, and A. Mantero, “Modeling radiation chemistry in the geant4 toolkit,” *Progress in Nuclear Science and Technology*, pp. 503–508, 2011. [Online]. Available: http://inis.iaea.org/search/search.aspx?orig_q=RN:49052093
- [125] M. Karamitros, S. Luan, M. A. Bernal, J. Allison, G. Baldacchino, M. Davidkova, Z. Francis, W. Friedland, V. Ivantchenko, A. Ivantchenko, A. Mantero, P. Nieminen, G. Santin, H. N. Tran, V. Stepan, and S. Incerti, “Diffusion-controlled reactions modeling in geant4-dna,” *Journal of Computational Physics*, vol. 274, pp. 841–882, 2014. [Online]. Available: <https://www.sciencedirect.com/science/article/pii/S0021999114004185>
- [126] W. Sung and J. Schuemann, “Energy optimization in gold nanoparticle enhanced radiation therapy,” *Phys Med Biol*, vol. 63, no. 13, p. 135001, 2018. [Online]. Available: <https://www.ncbi.nlm.nih.gov/pubmed/29873303>
- [127] T. Wolfe, D. Chatterjee, J. Lee, J. D. Grant, S. Bhattarai, R. Tailor, G. Goodrich, P. Nicolucci, and S. Krishnan, “Targeted gold nanoparticles enhance sensitization of prostate tumors to megavoltage radiation therapy in vivo,” *Nanomedicine*, vol. 11, no. 5, pp. 1277–83, 2015. [Online]. Available: <https://www.ncbi.nlm.nih.gov/pubmed/25652893>

- [128] R. M. Thomson and I. Kawrakow, “On the monte carlo simulation of electron transport in the sub-1 keV energy range,” *Med Phys*, vol. 38, no. 8, pp. 4531–4, 2011. [Online]. Available: <https://www.ncbi.nlm.nih.gov/pubmed/21928623>
- [129] A. Ku, V. J. Facca, Z. Cai, and R. M. Reilly, “Auger electrons for cancer therapy - a review,” *EJNMMI Radiopharm Chem*, vol. 4, no. 1, p. 27, 2019. [Online]. Available: <https://www.ncbi.nlm.nih.gov/pubmed/31659527>
- [130] N. N. Cheng, Z. Starkewolf, R. A. Davidson, A. Sharmah, C. Lee, J. Lien, and T. Guo, “Chemical enhancement by nanomaterials under x-ray irradiation,” *J Am Chem Soc*, vol. 134, no. 4, pp. 1950–3, 2012. [Online]. Available: <https://www.ncbi.nlm.nih.gov/pubmed/22260210>
- [131] K. Nejati, M. Dadashpour, T. Gharibi, H. Mellatyar, and A. Akbarzadeh, “Biomedical applications of functionalized gold nanoparticles: A review,” *Journal of Cluster Science*, vol. 33, no. 1, pp. 1–16, 2022. [Online]. Available: <https://doi.org/10.1007/s10876-020-01955-9>
- [132] F. Xiao, Y. Zheng, P. Cloutier, Y. He, D. Hunting, and L. Sanche, “On the role of low-energy electrons in the radiosensitization of dna by gold nanoparticles,” *Nanotechnology*, vol. 22, no. 46, p. 465101, 2011. [Online]. Available: <https://www.ncbi.nlm.nih.gov/pubmed/22024607>
- [133] S. J. McMahon, J. Schuemann, H. Paganetti, and K. M. Prise, “Mechanistic modelling of dna repair and cellular survival following radiation-induced dna damage,” *Sci Rep*, vol. 6, p. 33290, 2016. [Online]. Available: <https://www.ncbi.nlm.nih.gov/pubmed/27624453>
- [134] S. J. McMahon and K. M. Prise, “A mechanistic dna repair and survival model (medras): Applications to intrinsic radiosensitivity, relative biological effectiveness and dose-rate,” *Front Oncol*, vol. 11, p. 689112, 2021. [Online]. Available: <https://www.ncbi.nlm.nih.gov/pubmed/34268120>
- [135] A. Marusyk and K. Polyak, “Tumor heterogeneity: causes and consequences,”

- Biochim Biophys Acta*, vol. 1805, no. 1, pp. 105–17, 2010. [Online]. Available: <https://www.ncbi.nlm.nih.gov/pubmed/19931353>
- [136] B. Zhivotovsky, B. Joseph, and S. Orrenius, “Tumor radiosensitivity and apoptosis,” *Exp Cell Res*, vol. 248, no. 1, pp. 10–7, 1999. [Online]. Available: <https://www.ncbi.nlm.nih.gov/pubmed/10094808>
- [137] I. Dagogo-Jack and A. T. Shaw, “Tumour heterogeneity and resistance to cancer therapies,” *Nat Rev Clin Oncol*, vol. 15, no. 2, pp. 81–94, 2018. [Online]. Available: <https://www.ncbi.nlm.nih.gov/pubmed/29115304>
- [138] J. C. L. Alfonso and L. Berk, “Modeling the effect of intratumoral heterogeneity of radiosensitivity on tumor response over the course of fractionated radiation therapy,” *Radiat Oncol*, vol. 14, no. 1, p. 88, 2019. [Online]. Available: <https://www.ncbi.nlm.nih.gov/pubmed/31146751>
- [139] J. Perez-Beteta, A. Martinez-Gonzalez, D. Molina, M. Amo-Salas, B. Luque, E. Arregui, M. Calvo, J. M. Borrás, C. Lopez, M. Claramonte, J. A. Barcia, L. Iglesias, J. Avecillas, D. Albillo, M. Navarro, J. M. Villanueva, J. C. Paniagua, J. Martino, C. Velasquez, B. Asenjo, M. Benavides, I. Herruzo, M. D. Delgado, A. Del Valle, A. Falkov, P. Schucht, E. Arana, L. Perez-Romasanta, and V. M. Perez-Garcia, “Glioblastoma: does the pre-treatment geometry matter? a postcontrast t1 mri-based study,” *Eur Radiol*, vol. 27, no. 3, pp. 1096–1104, 2017. [Online]. Available: <https://www.ncbi.nlm.nih.gov/pubmed/27329522>
- [140] D. Sakata, I. Kyriakou, S. Okada, H. N. Tran, N. Lampe, S. Guatelli, M. C. Bordage, V. Ivanchenko, K. Murakami, T. Sasaki, D. Emfietzoglou, and S. Incerti, “Geant4-dna track-structure simulations for gold nanoparticles: The importance of electron discrete models in nanometer volumes,” *Med Phys*, vol. 45, no. 5, pp. 2230–2242, 2018. [Online]. Available: <https://www.ncbi.nlm.nih.gov/pubmed/29480947>

- [141] D. Sakata, I. Kyriakou, H. N. Tran, M. C. Bordage, A. Rosenfeld, V. Ivanchenko, S. Incerti, D. Emfietzoglou, and S. Guatelli, “Electron track structure simulations in a gold nanoparticle using geant4-dna,” *Phys Med*, vol. 63, pp. 98–104, 2019. [Online]. Available: <https://www.ncbi.nlm.nih.gov/pubmed/31221415>